THE UNIVERSITY OF
SYDNEY

Data-Driven Numerical Modelling of the Solar Coronal Magnetic Field

A thesis submitted in fulfilment of the requirements for the degree of
Doctor of Philosophy

by

Stuart Anthony Gilchrist

Sydney Institute for Astronomy
School of Physics
Faculty of Science
The University of Sydney
Australia

March 18, 2014

Contents

Statement of originality

This thesis contains no material which has been presented for a degree at this or any other university. To the best of my knowledge, this thesis contains no copy or paraphrase of work completed by another person, except where duly acknowledged in the text.

I wrote the codes presented in Chapters 3 and 4, and derived the solutions presented in Chapter 5. I performed all the testing and development of the codes myself.

The preparation of the *Hinode* data in Chapter 2 was performed by KD Leka, and the numerical modelling code used in this chapter was written by Mike Wheatland. I performed the calculations and analysis of the results.

_____

Stuart Anthony Gilchrist

Acknowledgments

I would like to thank my PhD supervisor Mike Wheatland for his guidance and encouragement over the course of my studies. The work in this thesis would not have been possible without his excellent mentoring and insight. Thank you for your good advice over the years and for teaching me the importance of clarity of thought and expression. I would also like to thank my co-supervisor Don Melrose for his helpful advice, and Dave Galloway, whose excellent fluid dynamics course inspired my interest in magneto-hydrodynamics.

I thank my parents Judy and Duncan Gilchrist, and my sister Amy for their support during my many years of study.

I thank KD Leka for her helpful advice on spectro-polarimetric data, and for providing the data for Chapter 2 of this thesis despite a broken wrist.

I would like to thank Graham Barnes for kindly funding a trip to Boulder in 2012, and his hospitality during the visit. I also acknowledge that this trip was partially funded by The University of Sydney's Postgraduate Research Support Scheme.

I thank Marc De Rosa, Anny Malanushenko and Mark Cheung for hosting me during a trip to California in 2010. This trip was partially funded by a William and Catherine McIlrath Scholarship (grants-in-aid).

I thank the organisers of the nonlinear force-free workshop "Nonlinear Force-Free Modeling of the Solar Corona: Towards a New Generation of Methods" for inviting me to participate, and the International Space Science Institute for hosting and funding the workshop, and for partially funding my travel to Bern Switzerland in 2013.

I acknowledge the support of an Australian Postgraduate Research Award.

I thank the many fellow students who made daily life at the university more enjoyable. Especially Tim White, Chris Trinh and Pat Noble with whom I had many enjoyable and memorable discussions. Also, I thank my teaching colleagues Paul Stewart, Emma Lindley, Mohammad Rafat, and Kevin Aquino; my unofficial German tutor Mathias Redlich; my former office mates Adam Keane, and Muazzam Ali; my fellow research group members Pat Noble, Rai Yuen, and Mohammad Rafat; and former students turned colleagues Joe Callingham and Aina Musaeva.

I thank Joe Callingham and Don Melrose for proof reading this thesis.

In this thesis we present work based on data from the Synoptic Optical Long-term Investigations of the Sun (SOLIS) Vector-Spectromagnetograph, and the *Hinode* SpectroPolarimeter. SOLIS data used here are produced cooperatively by NSF/NSO and NASA/LWS. Hinode is a Japanese mission developed and launched by ISAS/JAXA, collaborating with NAOJ as a domestic partner, and NASA and STFC (UK) as international partners. Scientific operation of the Hinode mission is conducted by the Hinode science team organized at ISAS/JAXA. This team mainly consists of scientists from institutes in the partner countries. Support for the post-launch operation is provided by JAXA and NAOJ (Japan), STFC (UK), NASA, ESA, and NSC (Norway).

Publications

The following journal articles are based on work in this thesis.

1. Gilchrist, S.A., Wheatland, M.S., Leka, K.D.: 2012, *Solar Physics* **276**, 133.
2. Gilchrist, S.A., Wheatland, M.S.: 2013, *Solar Physics* **282**, 283.
3. Gilchrist, S.A., Wheatland, M.S.: 2014, *Solar Physics* **289**, 1153.

Chapter 2 is based on the work presented in Paper 1. Chapter 3 is based on the work presented in Paper 2. Chapters 4 and 5 are based on the work presented in Paper 3.

The following conference proceedings contain work from this thesis.

1. Wheatland, M.S., Gilchrist S.A.: 2013, *Journal of Physics Conference Series*, **440**, 012037.

Work from Chapters 2, 3, and 4 appears in Proceedings 1.

Summary

The aim of this thesis is the development of numerical models for determining the coronal magnetic field from observations of the magnetic field at the photosphere (coronal magnetic field extrapolation), with an emphasis on numerical methods, computation and code development.

In Chapter 1 we present motivation for this modelling. We outline the limitations of observational methods for the coronal magnetic field and introduce extrapolation modelling. We focus on the nonlinear force-free model, and discuss the limitations of this model.

In Chapter 2 we present free energy estimates for the solar active region AR 11029 derived from a force-free model applied to data from the *Hinode* Spectropolarimeter and the Synoptic Optical Long-term Investigations of the Sun Vector-Spectromagnetograph. This region was chosen because a previous study of flare occurrence in the region suggested that the free magnetic energy of the region may have been exhausted by its high level of flare activity. We use nonlinear force-free modelling to address this question. The work illustrates many of the difficulties with modelling discussed in Chapter 1.

Presently, the most popular model for extrapolations is the nonlinear force-free model. This model ignores the role of pressure and gravity forces, which is a valid assumption in the tenuous corona. However, vector magnetograms are taken at the height of the photosphere, where the gas density is much higher and pressure and gravity forces are significant. This results in a basic inconsistency between the force-free model and the magnetogram data, which causes problems with the modelling. In Chapter 3 we present a numerical code for solving a magneto-hydrostatic model of the corona which includes pressure forces in the corona. The code is applied to a simple test case to demonstrate its correctness. The code is based on the Grad-Rubin method, and represents a first step towards more general magneto-hydrostatic modelling of the solar corona.

Most codes for solving the nonlinear force-free model assume the curvature of the photosphere to be negligible. This assumption restricts the methods to small active regions where the photosphere can be considered locally flat. Most active regions do not satisfy this criterion and this reduces the applicability of the force-free models. A new generation of instruments such as the Helioseismic and Magnetic Imager on the *Solar Dynamics Observatory* provide full-disk vector magnetogram data suitable for constructing models based on data from the entire photosphere.

In Chapter 4 we present a numerical code for solving the nonlinear force-free model in spherical polar coordinates which overcomes the limitations of the Cartesian models. The code is an implementation of the Grad-Rubin method, and is based on a spectral representation of the magnetic field in terms of vector-spherical harmonics. The details of the method are presented as are the results of the application of the code to a simple test case, which demonstrates the correctness of the implementation.

In Chapter 5 we derive the vector-spherical harmonic solution to Ampere's law which is presented in Chapter 4 without derivation. This solution forms an important part of the spherical code presented in Chapter 4.

In Chapter 6 we provide a summary and outlook for future work.

Chapter 1

Introduction

Magnetic fields in the extended outer atmosphere of the Sun, the solar corona, are responsible for solar activity. Solar flares, coronal mass ejections and similar events are the result of the explosive release of magnetic energy stored in the coronal magnetic field (Priest and Forbes, 2002). These events are the most energetic in the solar system. They produce radiation and high energy particles which can damage satellites and electrical infrastructure on Earth, and are dangerous to manned space missions. Solar activity is coronal in origin and accurate information on the coronal magnetic field is required to understand it.

It has proven very difficult to study the coronal magnetic field observationally. Solar magnetic fields are determined remotely through their effect on the solar radiation reaching the Earth. A number of radiative processes in the corona are sensitive to the presence of magnetic fields (*e.g.* the Zeeman and Hanle effects, and gyromagnetic emission). However as a result of the hot, rarefied, and optically thin character of the coronal plasma, it has proven difficult to use these as reliable diagnostics for the coronal magnetic field. Presently, no observational method provides basic information such as the field strength and direction accurately and routinely. When this information is available, it is usually restricted to a single height in the atmosphere, or to the two-dimensional plane of the sky. The complete three-dimensional structure of the field is not obtained, and this is a major obstacle to the study of coronal physics.

In the denser, cooler gas of the solar photosphere, optical absorption lines sensitive to the Zeeman effect form (Stenflo, 1994; Landi Degl'Innocenti and Landolfi, 2004). Measurements of the polarisation state of the lines can be used to infer the vector magnetic field at the height of line formation. This process is called spectro-polarimetric inversion and is an accurate and well understood process compared with methods for determining the coronal magnetic field. Spectro-polarimetric inversion produces vector magnetograms, which are two dimensional maps of the vector magnetic field at the height at which the lines form. Vector magnetograms are routinely produced by several ground-based and space-based observatories.

Models can provide what observations presently cannot: the three-dimensional magnetic field in the corona, subject to the caveat that the accuracy of the magnetic field depends on the accuracy of the model. Models vary in complexity and scope from one-dimensional static models of flux tubes (Nagai, 1980), to three-dimensional time-dependent magneto-hydrodynamic models of the global magnetic field (Usmanov, 1996; Mikić *et al.*, 1999). Data driven models use photospheric magnetic field data and a static subset of the magneto-hydrodynamic equations to compute the magnetic field in the corona. The magnetic field that results from solving the model is an extrapolation of the photospheric magnetic field. This kind of modelling began in the 1960s, and over the past five decades, the complexity of the models and the quality of the photospheric data have been steadily improving. At present, the nonlinear force-free model is the most popular model, although it has several limitations.

This thesis addresses problems with the nonlinear force-free model used to represent the coronal magnetic field. Here, we address questions surrounding the reliability of the model, and develop extensions to the present model. This introduction chapter provides motivation and context for coronal magnetic field modelling.

1.1 Remote Determination of the Solar Magnetic Field

All observational methods for determining the solar magnetic field are indirect. In each case what is measured directly is some property of the radiation reaching Earth (*e.g.* polarisation, intensity), and the magnetic field is determined by the solution of an inverse problem which depends on the details of the radiative process and the type of observations being made. In general the inverse problem is under-constrained, *i.e.* the observations do not unambiguously determine the physical conditions at the sources. In addition, inversions often require modelling of the solar atmosphere, so the inferred quantities are inherently model dependent. In these ways indirect observations differ from direct measurements.

Conditions in the solar atmosphere vary significantly with height, and no single magnetically sensitive process is effective everywhere. Observations based on a single process provide an incomplete picture of the solar magnetic. In this section we briefly describe the methods for determining the magnetic field at the photosphere and in the corona.

1.1.1 Spectro-Polarimetric Observations of the Photospheric Magnetic Field

Hale (1908) was the first to determine the strength of the magnetic field at the Sun, and he did so by observing the Zeeman splitting of optical absorption lines in the solar spectrum. Over a century later, observation of the Zeeman effect is still the standard method for inferring magnetic fields in the lower solar atmosphere. Rather than measuring the broadening of the spectral lines as Hale did, modern methods are based on measurements of the polarisation state of the lines. Observations of this kind are called spectro-polarimetric observations (see reviews by Stenflo (1978) and Stenflo (2013)), and at present, are made by several ground-based and space-based observatories.

In the presence of a magnetic field particular spectral lines are split into several polarised Zeeman components (Landi Degl'Innocenti and Landolfi, 2004; Stenflo, 1994). Unpolarised light which traverses magnetised regions of the solar atmosphere emerges partially polarised, with the state of the magnetic field at the height of line formation imprinted on the Stokes profiles of the observed line. The Stokes profiles $I(\lambda)$, $U(\lambda)$, $Q(\lambda)$, and $V(\lambda)$ are the Stokes parameters I, U, Q, and V as a function of wavelength λ. The Stokes $V(\lambda)$ profile is sensitive to the line-of-sight component of the magnetic field, while the Stokes $U(\lambda)$ and $Q(\lambda)$ profiles are sensitive to the component of the magnetic field transverse to the line of sight (Landi Degl'Innocenti and Landolfi, 2004; Stenflo, 1994).

Routine study of the photospheric magnetic field began with the invention of the magnetograph (Kiepenheuer, 1953; Babcock, 1953; Leighton, 1959). The first generation of instruments (Beckers, 1968) determined the line-of-sight component of the magnetic field by measuring the wavelength integrated Stokes profiles, *i.e.*

$$S_V = \frac{\int V(\lambda) p(\lambda) d\lambda}{\int I(\lambda) p(\lambda) d\lambda}, \tag{1.1}$$

where $p(\lambda)$ is a filter profile which usually samples the wings of a magnetic line. In the "weak field" approximation (when the Zeeman splitting is small compared to thermal broadening), the line-of-sight magnetic field $B_{\rm los}$ is determined directly from S_V according to

$$S_V = C_{\rm los} B_{\rm los} \tag{1.2}$$

(Landi Degl'Innocenti and Landolfi, 2004), where $C_{\rm los}$ is a calibration constant which depends on the details of the instrument and the spectral line. Note that $B_{\rm los}$ is the projection of $\mathbf{B}$ along the line of sight and can be positive or negative depending on whether the field points towards or away from the observer.

A vector magnetograph (Stepanov and Severny, 1962) determines the strength and direction of the magnetic field by observing

$$S_U = \frac{\int U(\lambda) p(\lambda) d\lambda}{\int I(\lambda) p(\lambda) d\lambda}, \tag{1.3}$$

and

$$S_Q = \frac{\int Q(\lambda)p(\lambda)d\lambda}{\int I(\lambda)p(\lambda)d\lambda} \tag{1.4}$$

(Landi Degl'Innocenti and Landolfi, 2004). In the weak field limit, S_Q and S_U are related to the component of the magnetic field transverse to the line of sight $B_\perp$ by

$$\sqrt{S_U^2 + S_Q^2} = C_\perp B_\perp^2 \tag{1.5}$$

(Landi Degl'Innocenti and Landolfi, 2004), where $C_\perp$ is the transverse calibration constant. The inclination of the magnetic field to the line of sight can be found from the ratio of $B_{\rm los}$ and $B_\perp$. The direction in the plane of the sky is determine by the azimuthal angle $\phi_{\rm azm}$, which is the angle subtended in the plane of the sky by the transverse component of the magnetic field relative to the "north" of the observer's reference frame. It is related to S_Q and S_U by

$$\tan(2\phi_{\rm azm}) = \frac{S_U}{S_Q} \tag{1.6}$$

(Landi Degl'Innocenti and Landolfi, 2004). Equation (1.6) is invariant under the transformation $\phi_{\rm azm} \rightarrow \phi_{\rm azm} + \pi$, and as a result $\phi_{\rm azm}$ can only be determined up to a factor of 180°. This 180° ambiguity is not a result of the weak field approximation but is a general feature of spectro-polarimetric observations. Here we have presented the most basic method for determining the solar magnetic field from integrated Stokes profiles (see Landi Degl'Innocenti and Landolfi (2004) and reference therein for more advanced methods).

An advantage of the magnetograph is that the inversion does not require explicit modelling of the solar atmosphere, so the inversions are not computationally intensive and can be performed quickly on large data sets. The disadvantage is that the weak-field approximation is invalid in active regions (particular in the umbra of sunspots), so the results can significantly underestimate the magnetic field in strong field regions (Jefferies, Lites, and Skumanich, 1989; Jefferies and Mickey, 1991). In addition, the neglect of magneto-optical effects means $\phi_{\rm azm}$ is determined inaccurately (Landi Degl'Innocenti, 1979).

A spectro-polarimeter measures the wavelength dependence of the Stokes profiles over the wavelength range enclosing the magnetic line. Determination of the magnetic field from the Stokes profiles is called Stokes inversion or spectro-polarimetric inversion. In general, it is not based on the weak-field assumption and requires explicit modelling of the solar atmosphere. The inversion is performed by fitting model Stokes profiles to the data, where the model profiles are determined by solving the radiative transport equation for polarised light in a model atmosphere.

Several inversion methods exist and are based on different choices of model atmosphere and fitting methods (see references in Landi Degl'Innocenti and Landolfi 2004). It is popular to assume a Milne-Eddington atmosphere (Harvey, Livingston, and Slaughter, 1972; Auer, House, and Heasley, 1977; Skumanich and Lites, 1987), in which the magnetic field and thermodynamic parameters do not vary with optical depth or across a pixel. For the Milne-Eddington model, the radiative transfer equations can be solved analytically. The solution is called the Unno-Rachkovsky solution (Unno, 1956; Rachkovsky, 1962). Milne-Eddington inversion is performed by fitting the analytic Unno-Rachkovsky solutions to the observed Stokes profiles, with the magnetic field and thermodynamic parameters treated as parameters in the fitting. If the variation of the magnetic field with optical depth is small, the Milne-Eddington method is expected to recover the vector magnetic field. More complicated treatments of the atmosphere are required to deal with variation in optical depth (Landi Degl'Innocenti and Landolfi, 2004).

The direction of the magnetic field in the plane of the sky is determined up to a 180° ambiguity. The ambiguity can be resolved by introducing an additional constraint on the magnetic field, *e.g.* that the magnetic field should minimise the electric currents flowing through the photosphere (see Metcalf *et al.* (2006) and references therein). The constraints are not determined just from observations but require additional assumptions, which introduces uncertainty in the data. Despite this, it has been shown that these methods can determine the correct direction when applied to test cases, with some methods being more accurate than others (Metcalf *et al.*, 2006).

The spatial, temporal, and spectral resolution of spectro-polarimeters has improved greatly over the past few decades, and the inversion methods have reached a high level of automation. Spectro-polarimetric

observations are performed routinely by a number of dedicated instruments located on Earth and in space, and vector magnetogram data are produced on a daily or hourly basis. In summary, vector magnetogram data are abundant and of high quality.

1.1.2 Observational Methods for Determining the Coronal Magnetic Field

Compared to the magnetic field at the photosphere, the coronal magnetic field is difficult to observe. In common with the photospheric magnetic field, remote study of the coronal magnetic field relies on the presence of radiative mechanisms which couple the coronal magnetic field to solar radiation. The environment of the coronal plasma differs from the photosphere: it is a high temperature plasma with relatively weak magnetic fields. This means the effect of the magnetic field on the radiation is difficult to discern due to thermal effects. In addition, the corona is optically thin at most wavelengths meaning that magnetic fields everywhere along a line of sight contribute to an observed signal.

In this section we give a brief description of the methods used for observational study of the coronal magnetic field. This list is not exhaustive, and we are not aware of a comprehensive review. However, Dulk and McLean (1978) and Stenflo (1978) review a number of methods, Gelfreikh (1994) reviews radio based methods. We also note that we have neglected methods based on observations of radio emission from flare loops (Gary, Fleishman, and Nita, 2013), and observations based on post flare oscillations of loops in EUV images (Aschwanden and Schrijver, 2011).

Optical, X-ray and Ultra-Violet Images

Historically, the corona itself has been difficult to observe because it is extremely faint compared to the solar disk. Before the invention of the coronograph, and space-based X-ray and Extreme-UltraViolet (EUV) telescopes, the corona was only observed during total solar eclipses, which are infrequent and provide only a short observational window. The difficulties inherent to coronal observations are even more pronounced for the coronal magnetic field, which cannot be directly imaged by a telescope, but instead must be inferred indirectly from its effect on the solar plasma, and the Sun's radiation. Optical coronagraphs, and EUV and X-ray images show structure in the coronal plasma determined by the magnetic field, and quantitatively map the structure and topology of the coronal magnetic field. However the images do not provide information on the strength and direction of the magnetic field.

Spectro-Polarimetric Observations of Forbidden Coronal Emission lines

The polarisation of coronal emission lines (such as the Fe XIII line) provides a way to determine the coronal magnetic field from optical and IR observations (Judge, 1998; Judge, Habbal, and Landi, 2013). The Stokes $V(\lambda)$ component of these lines is due to the Zeeman effect and is sensitive to the line-of-sight magnetic field (Judge, 1998). The Stokes $V(\lambda)$ signal is weak and difficult to measure but has been achieved (Lin, Penn, and Tomczyk, 2000; Lin, Kuhn, and Coulter, 2004). The Stokes U and Q components are the result of resonance scattering which is modified by the presence of a magnetic field. The effect of the magnetic field on the resonance scattering occurs in the strong field or saturated regime and therefore the Stokes U and Q signals can only provide the direction of the magnetic field in the plane of the sky.

Coronal emissions are faint compared to the solar disk and can only be observed above the limb when the disk is occulted (either by the Moon or a coronograph). The corona is optically thin to these emissions and the observed signal represents the effect of magnetic fields integrated over the line of sight. As such it is difficult to assign magnetic field values to particular points in the corona.

Spectro-polarimetric Observations of Prominences

In addition to coronal emission lines, spectro-polarimetric diagnostics can be applied to prominences. The prominence gas is denser and cooler than the surrounding corona, and the conditions resemble those in the photosphere (Aschwanden, 2004). Prominences are confined to a relatively small region of space allowing the source of the signal to be determined with more precision. The magnetic field in prominences has been determined by Zeeman and Hanle effect measurements (*e.g.* Rust 1967; Leroy 1977). However, it should be noted that the prominence magnetic field is unlikely to be typical of the coronal magnetic field due to the significant difference between the coronal and prominence plasmas.

Gyroresonance Radio Emission

Gyroresonance emission in the corona is due to the helical motion of electrons in the coronal magnetic field (Melrose and McPhedran, 1991) and is a natural diagnostic for the magnetic field. At a given radio frequency, f, gyromagnetic emission is strongly absorbed in the corona by thin gyroresonance layers at which

$$f_{\mathrm{B}} = \frac{f}{s}, \tag{1.7}$$

where f_{B} is the electron gyro-frequency, which is proportional to the magnitude B of the magnetic field, and where s is the harmonic number of the emission. This is an oversimplified picture as the optical depth also depends on the viewing angle, electron temperature and density, and the mode of the wave (Melrose and McPhedran, 1991). When the harmonic number of the emission is known, maps of the radio brightness represent surfaces of constant B (isogauss surfaces) in the corona (White and Kundu, 1997; Tun *et al.*, 2011).

Gyroresonance layers are optically thick and physically thin, which means the gyroresonance observations do not suffer from line-of-sight effects, and this is a major advantage of the method. The disadvantage of this approach is that the absolute height of a given gyroresonance layer is not well determined. The method only provides a qualitative determination of the height distribution of the magnetic field.

Summary

It is possible to determine the coronal magnetic field from observations using the methods explained in this section. The overall decrease in magnetic field strength with height above the photosphere has been constructed from multiple observations using different methods at different heights (Dulk and McLean, 1978). However, in general, the methods determine the distributions of magnetic fields with low confidence, limited spatial extent, and the location in the corona where the magnetic field is being determined is often ambiguous due to line-of-sight-effects. In addition, some methods require special conditions outside the observer's control such as the presence of a prominence. Significant improvements in theory and instrumentation are required before observational methods are sufficiently advanced to allow for systematic study of the coronal magnetic field with a level of accuracy and automation similar to that obtained by observational methods for the photospheric magnetic field.

1.2 Determination of the Coronal Magnetic Field from Extrapolation of Photospheric Data

The observational picture of the magnetic field in the Sun's atmosphere is incomplete: the magnetic field is only determine routinely and accurately at a single height in the atmosphere (the photosphere), and is unknown at all heights above. Extrapolation of the two-dimensional magnetic field data at the photosphere into the corona can be performed by assuming a model for the coronal magnetic field. The model provides a

set of equations for the magnetic field in the volume, and the photospheric data provide boundary conditions for the model. In this way the model provides a way to calculate the coronal magnetic field from the data, and the modelling is referred to as data-driven modelling (see reviews by Régnier 2013, Wiegelmann and Sakurai 2012, and Wiegelmann 2008). This approach is attractive because of the abundance and high quality of photospheric magnetic field data compared with that for the corona. The drawback is that the computed magnetic field only represents the true coronal magnetic field in so far as the chosen model is accurate.

1.2.1 Justification and Scope of Static Models of the Coronal Magnetic Field

The magnetic Reynolds number in the corona is sufficiently large that the coronal magnetic field can be considered to be frozen in to the coronal plasma (Sturrock, 1994). The strong coupling means that the coronal magnetic field and the hydrodynamics of the coronal plasma cannot be considered in isolation. For the purpose of modelling the corona, ideal magneto-hydrodynamics (MHD) provides a mathematical framework and a set of equations for modelling the dynamic evolution of the coronal plasma/magnetic field system (Sturrock, 1994).

Except during solar flares and eruptions, the coronal magnetic field of active regions evolves in slow response to the driving of the photospheric magnetic field. The time delay between changes at the photosphere and in the corona depends on the Alfvén speed in the corona, and for active regions the time delay is small compared to the evolutionary time scale of the region (seconds compared with days to weeks). As a result, the magnetic field at any instant of time can be considered to be in a quasi-static state.

The quasi-static nature of the coronal magnetic field has implications for the modelling. The evolutionary time scale of the coronal magnetic field is also typically longer than the cadence of the spectro-polarimetric data, which requires an integration time of order minutes to hours. To a first approximation the data represents the instantaneous state of the field at the photosphere, and this justifies its use for time-independent (static) modelling of the coronal magnetic field.

The assumption of a static coronal magnetic field greatly simplifies the modelling. Time-dependent MHD calculations are difficult and computationally intensive. The static models should not be used to represent the coronal magnetic field during flares or eruptions, or to model small scale turbulent magnetic fields, but they should capture the large scale structure of the field, such as the active region loops observed in X-ray and EUV images.

1.2.2 Determination of the Coronal Magnetic Field as a Boundary Value Problem

Mathematically, the problem of computing the coronal magnetic field from observations at the photosphere takes the form of a boundary value problem. Different models require different boundary conditions. In general, as the complexity of a model increases so does the number of boundary conditions, and the computational difficulty. The domain is the coronal volume, Ω, and the lower boundary of the domain is the photosphere, $\partial\Omega_{\mathrm{photo}}$. The photosphere only represents the lower boundary of Ω, and typically additional boundaries are present depending on the choice of domain (*e.g.* transverse boundaries if only a subvolume of the corona is considered).

Extrapolation models may attempt to model only the local fields in a subvolume of the corona, or they may aim to model the global magnetic field all the way out to the solar wind. The scope of the modelling often determines the computational domain. For example, the infinite Cartesian half space

$$\Omega_{\mathrm{hs}} = \{(x, y, z) | z \geq 0\} \tag{1.8}$$

is used to model the coronal volume of small active regions where the curvature of the Sun is negligible (*e.g.* Schmidt 1964). The boundary of this domain is the $z = 0$ plane, which represents the photosphere.

1.3 The Potential Field Model

An early attempt to compute the coronal magnetic field from photospheric data was performed by Schmidt (1964), and was based on a vacuum (or potential field) model which neglected electric currents in the corona. The equations for the magnetic field in this model are

$$\nabla \times \mathbf{B} = 0, \tag{1.9}$$

and

$$\nabla \cdot \mathbf{B} = 0. \tag{1.10}$$

The boundary value problem in this case is well studied (Jackson, 1998). A unique solution is guaranteed if the normal component of $\mathbf{B}$ is specified on all boundaries. The linear form of Equations (1.9) and (1.10) imply closed form analytic solutions exist for this model (Schmidt, 1964; Altschuler and Newkirk, 1969; Sakurai, 1982).

The formal boundary conditions for the potential model are the prescription of the normal component of the magnetic field at the photosphere (Jackson, 1998). Observations determine the line-of-sight component of the magnetic field more accurately than the transverse component, and early instruments provided only the line-of-sight component. An equivalent formulation of the boundary value problem based on a prescription of $B_{\rm los}$ at the photosphere is more useful in practice (Semel, 1988; Cuperman, Ofman, and Semel, 1990).

Potential field models have been used to model active regions (Schmidt, 1964), and to model the global coronal magnetic field (Altschuler and Newkirk, 1969; Schatten, Wilcox, and Ness, 1969; Wang and Sheeley, 1992). The potential source-surface model is often used to determine the structure of the coronal magnetic at the Earth in order to predict the regions of fast and slow solar wind (Wang and Sheeley, 1992).

The potential field model of the corona is simple to implement but it is not realistic, especially in active regions. Significant photospheric currents are inferred from vector-magnetogram data in active regions, and EUV images show significantly twisted (non-potential) structures in the corona (Schrijver *et al.*, 2005; Wiegelmann *et al.*, 2005). Moreover, the energy of the current systems in the corona is believed to provide the energy for solar flares (Priest and Forbes, 2002).

1.4 Extrapolating the Coronal Magnetic Field as a Force-Free Magnetic Field

Extrapolations based on the potential model are inadequate because they ignore the role of electric currents in the corona. A more sophisticated model which better approximates the likely state of the magnetic field in the corona is the force-free model. In this section we present the force-free equations, and the force-free boundary value problem for reconstructing the coronal magnetic field.

Force-free magnetic fields are a natural equilibrium state for a magnetised plasma in which non-magnetic forces are negligible. In the absence of non-magnetic forces, the magnetic (Lorentz) force must be self-balancing, *i.e.*

$$\mathbf{J} \times \mathbf{B} = 0, \tag{1.11}$$

where $\mathbf{J}$ is the electric current density. Equation (1.11) is the defining equation for a force-free magnetic field. A consequence of Equation (1.11) is that electric currents are constrained to flow along magnetic field lines. The magnetic field and current also satisfy the magnetostatic Maxwell equations (Jackson, 1998)

$$\nabla \times \mathbf{B} = \mu_0 \mathbf{J}, \tag{1.12}$$

and

$$\nabla \cdot \mathbf{B} = 0. \tag{1.13}$$

The coupling between the magnetic field and the electric current implied by Equation (1.11) means that the system of equations is nonlinear.

It is generally thought that the coronal magnetic field is in an approximately force-free state. Theoretical arguments and observational evidence support this hypothesis. A magnetic field is force-free when $\beta \ll 1$, where

$$\beta = \frac{p}{B^2/2\mu_0}. \tag{1.14}$$

A basic estimate of β in the corona can be made by assuming the ideal gas law for pressure $p = nkT$, where n is the number density, T is the temperature, and k is Boltzmann's constant. Assuming a number density $n = 10^9\,\mathrm{cm}^{-3}$, a temperature $T = 10^6\,\mathrm{K}$, and a magnetic field $B = 100\,\mathrm{G}$, gives $\beta \approx 10^{-4}$. A detailed study of the β in the corona due to Gary (2001), incorporating data from many sources, estimated β in the range $10^{-4} - 10^{-2}$ at a height of $\approx 1\,\mathrm{Mm}$ above an active region, and more widely varying values of β above and below this height.

Spectro-polarimetric observations of the vector magnetic field can provide estimates of the residual Lorentz forces in a subvolume of the solar atmosphere. Observations in the chromosphere/photosphere above an active region indicate that the magnetic field becomes force-free at a height of $\approx 400\,\mathrm{km}$ above the photosphere (Metcalf *et al.*, 1995), for the particular region studied.

Equation (1.11) implies that for a force-free magnetic field, the magnetic field and electric currents are aligned:

$$\mu_0 \mathbf{J} = \alpha(\mathbf{r})\mathbf{B}, \tag{1.15}$$

where α is a scalar function of the position $\mathbf{r}$, which is often called the force-free parameter. Equations (1.11)-(1.12) expressed in terms of α and $\mathbf{B}$ are

$$\nabla\alpha \cdot \mathbf{B} = 0, \tag{1.16}$$

$$\nabla \times \mathbf{B} = \alpha\mathbf{B}, \tag{1.17}$$

and

$$\nabla \cdot \mathbf{B} = 0. \tag{1.18}$$

As a consequence of Equation (1.16), α is constant along magnetic field lines.

1.4.1 Linear Force-Free Model

The force-free equations are nonlinear, except in the special case that α is a constant. The solutions to the linear problem are called linear force-free magnetic fields, and the model is called the linear force-free model. Because the equations are linear, closed form analytic solutions exist (Nakagawa and Raadu, 1972; Chiu and Hilton, 1977; Barbosa, 1978; Alissandrakis, 1981).

The linear force-free model suffers from several problems. Firstly, the solution is not uniquely determined by the magnetic field at the boundary (Chiu and Hilton, 1977). Additional restrictions are required to determine a unique solution. Different choices lead to different solutions, and it is not clear *a priori* which choice is correct. One resolution of this problem is to choose the constraint which leads to a solution which best matches the observed photospheric field (Wheatland, 1999). A second problem with applying the linear force-free model for coronal modelling is that linear force-free fields typically contain infinite magnetic energy in an unbounded space (Alissandrakis, 1981). A third problem with using the linear force-free model is that observations imply α varies significantly in the corona. Maps of α determined by spectro-polarimetric methods show significant variation in α over the photosphere (Pevtsov, Canfield, and Metcalf, 1994). This implies significant variation of α in the corona, because α is constant along field lines in the force-free model. These problems make the linear force-free model of limited use for modelling the coronal magnetic field.

1.4.2 Nonlinear Force-Free Model

The general case where α is a function of position is referred to as the nonlinear force-free model. In general, the nonlinear equations must be solved numerically, except in specific cases. The nonlinear model avoids some of the problems of the linear force-free model: the energy in the field can be finite in an infinite domain.

1.4.3 Formulation of the Nonlinear Force-Free Boundary Value Problem

The formal boundary value problem for force-free modelling can be stated in different ways depending on the choice of boundary conditions on the photosphere (different possible choices are discussed by Grad and Rubin (1958)). Some definitions use all three components of $\mathbf{B}$ over the entire boundary, while others prescribe the normal component of the magnetic field $\mathbf{B}\cdot\hat{\boldsymbol{n}}$ and the distribution of α over a single polarity of $\mathbf{B}\cdot\hat{\boldsymbol{n}}$, *i.e.* α is prescribed at points where $\mathbf{B}\cdot\hat{\boldsymbol{n}} < 0$ or at points where $\mathbf{B}\cdot\hat{\boldsymbol{n}} > 0$. The latter has been shown to provide a well-posed[1] formulation of the problem (in particular domains) for sufficiently small values of α, while the former is an over specification of the problem (Bineau, 1972; Boulmezaoud and Amari, 2000; Kaiser, Neudert, and von Wahl, 2000). In both cases the boundary value problem is nonlinear and in general requires a numerical treatment.

1.5 Numerical Solution Methods for the Nonlinear Force-Free Model

Several numerical methods have been developed for solving the nonlinear force-free equations. The methods are based on different formulations of the force-free boundary value problem (see reviews by Sakurai (1989), or more recently Wiegelmann (2008)). In this section we give a brief outline of the most popular solution methods.

1.5.1 Vertical Integration Method

The specific form of the force-free equations means it is possible to reformulate the force-free boundary value problem as an initial value problem (Wu *et al.*, 1990). In Cartesian coordinates, the vertical derivatives of α and the components of the magnetic field are:

$$\frac{\partial B_z}{\partial z} = -\frac{\partial B_x}{\partial x} - \frac{\partial B_y}{\partial y}, \tag{1.19}$$

$$\frac{\partial B_x}{\partial z} = \alpha B_y + \frac{\partial B_z}{\partial x}, \tag{1.20}$$

$$\frac{\partial B_y}{\partial z} = -\alpha B_x + \frac{\partial B_z}{\partial y}, \tag{1.21}$$

and

$$\frac{\partial \alpha}{\partial z} = -\frac{1}{B_z}\left(B_x\frac{\partial \alpha}{\partial x} + B_y\frac{\partial \alpha}{\partial y}\right). \tag{1.22}$$

The right hand sides of Equations (1.19)-(1.22) depend only on variables at the current height z, and therefore the system of partial differential equations can be treated as a system of coupled ordinary differential equations and directly integrated. The vector magnetic field is known at $z = 0$ from spectro-polarimetric data, and this is used to initiate the integration. In this way the boundary value problem is recast as an initial value problem in terms of the height variable z.

[1] A boundary value problem is said to be well-posed if it has a unique solution which depends continuously on the boundary conditions.

Unfortunately the vertical integration method is ill-posed and small errors in the initial conditions are magnified exponentially with height. Practical implementations require regularisation schemes to remove this instability (Demoulin, Cuperman, and Semel, 1992).

1.5.2 Optimisation Method

Solving the force-free equations can be treated as an optimisation problem where the goal is to minimise the functional (Wheatland, Sturrock, and Roumeliotis, 2000):

$$L = \int B^{-2}|(\nabla \times \mathbf{B}) \times \mathbf{B}|^2 + |\nabla \cdot \mathbf{B}|^2 dV, \tag{1.23}$$

where $B = |\mathbf{B}|$, and the integral is over the volume of the domain. The functional is positive definite with minimum value $L = 0$ (which is obtained for a magnetic field which satisfies the force-free equations).

Given an arbitrary initial field, the optimisation procedure arrives at a solution to the force-free equations by evolving $\mathbf{B}(\mathbf{x}, t)$, according to a pseudo-time parameter t, in such a way that L decreases monotonically with t. The requirement that L be a decreasing function of t determines an evolution equation for $\mathbf{B}(\mathbf{x}, t)$ which takes the form of a nonlinear diffusion equation

$$\frac{\partial \mathbf{B}}{\partial t} = \mu \mathbf{F}, \tag{1.24}$$

where μ is a positive function, and $\mathbf{F} = \mathbf{F}(\mathbf{B})$ is a function of $\mathbf{B}$ and its spatial derivatives (Wheatland, Sturrock, and Roumeliotis, 2000). The method is based on an overspecification of the boundary value problem, because the evolution requires $\mathbf{B}$ prescribed on all boundaries of the domain.

The original optimisation method (outlined here) has been extended to include additional terms in the functional L to model non-magnetic forces (Wiegelmann and Neukirch, 2006; Wiegelmann *et al.*, 2007), to constrain the departure of the field from the spectro-polarimetric boundary data (Wiegelmann and Inhester, 2010), and to include a weighting function which makes it possible to ignore particular subvolumes in the computation (Wiegelmann, 2004). It has also been implemented in spherical geometry (Wiegelmann, 2007; Wiegelmann *et al.*, 2007).

1.5.3 Magneto-Frictional Method

A force-free magnetic field is the equilibrium state of a magneto-hydrodynamic relaxation. The magneto-frictional method arrives at a force-free magnetic field by the physical evolution of an arbitrary initial magnetic field subject to an artificial friction force.

The method starts with an initial field in a volume. The magnetic field on the lower boundary is replaced by observed values. The mismatch at the lower boundary implies non-zero Lorentz forces which drive flows in the fluid. Subsequently the flows are damped by the artificial frictional force. The net result is that the magnetic field moves to a state with a smaller residual Lorentz force, and given sufficient time the magnetic field reaches a steady state which is force-free.

The evolution of the magnetic field $\mathbf{B}$, and fluid velocity $\mathbf{v}$ are governed by

$$\mathbf{v} = \frac{1}{\nu}(\nabla \times \mathbf{B}) \times \mathbf{B}, \tag{1.25}$$

and

$$\frac{\partial \mathbf{B}}{\partial t} = \nabla \times (\mathbf{v} \times \mathbf{B}), \tag{1.26}$$

where ν determines the strength of the artificial friction. The method is typically started with an initial potential magnetic field in the volume, and as mentioned, the evolution equations are solved with the observed $\mathbf{B}$ prescribed as a boundary condition. This represents an overspecification of the boundary value problem.

Magneto-frictional relaxation was introduced outside solar physics (Chodura and Schlueter, 1981), before being applied to modelling the corona (Yang, Sturrock, and Antiochos, 1986; Valori, Kliem and Keppens, 2005).

1.5.4 Boundary Integral Method

The force-free equations are a set of partial differential equations. Green's theorem can be used to replace the differential equations with the equivalent integral equation (Yan and Sakurai, 2000)

$$\mathbf{B} = \int_{\partial\Omega} \left(\mathbf{Y} \frac{\partial \mathbf{B}}{\partial n} - \frac{\partial \mathbf{Y}}{\partial n} \mathbf{B} \right) dS, \tag{1.27}$$

where the integral is over the boundary of the domain, $\partial/\partial n$ is the normal derivative to the boundary, and $\mathbf{Y}$ is a 3×3 diagonal matrix of reference functions of the form

$$Y_i(\mathbf{r}) = \frac{\cos(\lambda_i r)}{4\pi r}, \tag{1.28}$$

where λ_i is called the pseudo force-free parameter. There is a separate reference function and pseudo force-free parameter for each component of the magnetic field, which is represented by the subscript.

Equation (1.27) relates $\mathbf{B}$ at each point in the volume to an integral over quantities on the boundary of the domain. The magnetic field $\mathbf{B}$ is assumed to be known at the boundary (in practice it is provided by spectro-polarimetric observations). However the pseudo force-free parameters λ_i and the normal derivative of $\mathbf{B}$ are *a priori* unknown and must be determined by an iterative scheme (Yan and Sakurai, 2000).

The boundary integral method requires $\mathbf{B}$ on the boundary, which over specifies the problem.

1.5.5 Grad-Rubin Method

The Grad-Rubin method is an iterative method for solving the nonlinear force-free equations (Grad and Rubin, 1958). The method replaces the nonlinear Equations (1.16) and (1.17) with a set of linear equations which are solved repeatedly in a sequence of iterations. We denote a quantity after k Grad-Rubin iterations using a superscript in square brackets, for example $\mathbf{B}^{[k]}$. One iteration of the Grad-Rubin method may be written

$$\nabla \alpha^{[k+1]} \cdot \mathbf{B}^{[k]} = 0, \tag{1.29}$$

$$\nabla \times \mathbf{B}^{[k+1]} = \alpha^{[k+1]} \mathbf{B}^{[k]}. \tag{1.30}$$

The Grad-Rubin method is based on a well-posed formulation of the nonlinear force-free boundary value problem, *i.e.* the boundary conditions at the photosphere are the normal component of $\mathbf{B}$, and α over one polarity of the normal component of $\mathbf{B}$.

Equation (1.29) updates the force-free parameter α in the volume subject to boundary conditions on α. Equation (1.30) updates the magnetic field in the volume using the new α values together with the magnetic field from the previous iteration and the boundary conditions on the normal component of the field. Equations (1.29) and (1.30) are repeatedly solved until the magnetic field $\mathbf{B}^{[k]}$ and the force-free parameter $\alpha^{[k]}$ converge at all points in the volume. The fixed point of the iteration is a solution to the nonlinear force-free equations. The iteration is initiated using a potential field $\mathbf{B}^{[0]} = \mathbf{B}_0$ constructed from the boundary conditions on $\mathbf{B} \cdot \hat{\mathbf{n}}$.

The Grad-Rubin method was first applied in a solar context by Sakurai (1981). It has been implemented in Cartesian coordinates (Sakurai, 1981; Amari, Boulmezaoud, and Mikic, 1999; Wheatland, 2007) and more recently in spherical coordinates (Amari *et al.*, 2013; Gilchrist and Wheatland, 2014).

1.6 Practical Difficulties with the Nonlinear Force-Free Method

The nonlinear force-free model represents the existing state of the art for coronal magnetic field modelling. Several different extrapolation codes exist which are based on several different numerical solution methods. These have been tested on analytic solutions in order to ascertain the numerical accuracy and the computational efficiency of the algorithms and the particular implementations (see for example Schrijver *et al.* 2006 and references therein).

When applied to solar data, the force-free extrapolation methods encounter difficulties (Schrijver *et al.*, 2008; De Rosa *et al.*, 2009). The numerical methods for solving the nonlinear force-free equations are generally iterative, and when applied to solar data the methods often fail to converge.

1.6.1 Uncertainty in Spectro-Polarimetrically Derived Magnetic Field Data

Nonlinear force-free modelling uses spectro-polarimetrically derived vector magnetogram data as boundary conditions, and errors in the data are propagated to the modelling. There are several sources of uncertainty in the spectro-polarimetric data: noise, ambiguity resolution errors, the limitations of the Milne-Eddington inversion, and uncertainty due to the finite spectral, temporal and spatial resolution of the instrument. For a given set of data, all these problems are present to some degree. Although observational errors in the spectro-polarimetric data are a source of uncertainty in the modelling, the problems intrinsic to the model are probably more concerning.

1.6.2 Inconsistency between Magnetogram Data and the Force-Free Model

The force-free model ignores the role of pressure and gravity forces. In the corona this assumption is justifiable, but at the photosphere where the gas is denser and cooler it is not. Vector magnetograms represent the magnetic field at the photosphere and are therefore inconsistent with the force-free model.

The inconsistency between the data and the model causes convergence problems for numerical methods which over specify the boundary value problem. Methods based on the Grad-Rubin formulation of the boundary value problem (which are well-posed) also encounter convergence problems. In addition, for these methods the vector magnetogram data provide two choices of boundary conditions on α based on

$$\alpha_0(x,y) = \frac{1}{B_z}\left(\frac{\partial B_y}{\partial x} - \frac{\partial B_z}{\partial y}\right)\bigg|_{z=0}. \tag{1.31}$$

The two choices produce two solutions which are in general inconsistent with each other.

In Chapter 3 we outline an implementation of the Grad-Rubin method for constructing magneto-hydrostatic models of the coronal magnetic field, *i.e.* a model incorporating pressure forces. In principle, this model can overcome the inconsistency problem.

1.6.3 Assumption of Cartesian Geometry

It is common to assume Cartesian geometry for modelling the coronal magnetic field. In this geometry the photosphere is the $z = 0$ plane and the coronal volume is the space $z > 0$. This assumption ignores the curvature of the Sun and is accurate provided the region being modelled is the size of a small active region.

Historically, coronal field modelling was confined to active-region scales due to the limited field of view of early vector magnetographs. Recently, a new generation of instruments has provided full-disk vector magnetograms, which in principle permit full-Sun modelling.

In Chapter 4 we outline an implementation of the Grad-Rubin method for solving the force-free equations in spherical geometry, enabling full-Sun modelling.

1.6.4 Additional Boundary Conditions

Spectro-polarimetry only provides boundary conditions for modelling at the photosphere, but the numerical solution domains assumed for the modelling typically contain additional boundaries on which the magnetic field is not constrained by observation. An example is the infinite half space $\Omega_{\rm hs}$ considered in Cartesian models. In practice, this infinite domain is replaced with a finite box, which introduces top and transverse boundaries.

The additional boundaries require additional boundary conditions. Different methods treat this problem in slightly different ways, but in general *ad hoc* boundary conditions are assumed, such as periodicity. These boundary conditions do not reflect conditions at the Sun, and make the modelling less realistic. In Chapter 4 we present a method which makes no explicit assumption about the magnetic field at the boundaries.

Chapter 2

The Free Energy of NOAA Solar Active Region AR 11029

Gilchrist, S.A., Wheatland, M.S., Leka, K.D.: 2012, *Solar Physics* **276**, 133.

Abstract

The NOAA active region AR 11029 was a small but highly active sunspot region which produced 73 *GOES* soft X-ray flares during its transit of the disk in late October 2009. The flares appear to show a departure from the well known power-law frequency-size distribution. Specifically, too few *GOES* C-class and no M-class flares were observed by comparison with a power-law distribution (Wheatland in *Astrophys. J.* **710**, 1324, 2010). This was conjectured to be due to the region having insufficient magnetic energy to power the missing large events. We construct nonlinear force-free extrapolations of the coronal magnetic field of active region AR 11029 using data taken on 24 October by the SOLIS Vector-SpectroMagnetograph (SOLIS/VSM), and data taken on 27 October by the *Hinode* Solar Optical Telescope SpectroPolarimeter (*Hinode*/SP). Force-free modelling with photospheric magnetogram data encounters problems because the magnetogram data are inconsistent with a force-free model. We employ a recently developed "self-consistency" procedure which addresses this problem and accommodates uncertainties in the boundary data (Wheatland and Régnier in *Astrophys. J.* **700**, L88, 2009). We calculate the total energy and free energy of the self-consistent solution which provides a model for the coronal magnetic field of the active region. The free energy of the region is found to be $\approx 4 \times 10^{29}\,\mathrm{erg}$ on 24 October, and $\approx 7 \times 10^{31}\,\mathrm{erg}$ on 27 October. An order of magnitude scaling between *RHESSI* non-thermal energy and *GOES* peak X-ray flux is established from a sample of flares from the literature and is used to estimate flare energies from observed *GOES* peak X-ray flux. Based on the scaling, we conclude that the estimated free energy of AR 11029 on 27 October when the flaring rate peaked is sufficient to power M-class or X-class flares, and hence the modelling does not appear to support the hypothesis that the absence of large flares is due to the region having limited energy.

2.1 Introduction

Solar flares are the result of the explosive release of magnetic energy from intense coronal magnetic fields associated with sunspots (Priest and Forbes, 2002). Understanding the storage and release of magnetic energy in the corona is fundamental to understanding solar flares, and other coronal transient events (*e.g.*

coronal mass ejections and transient X-ray brightenings).

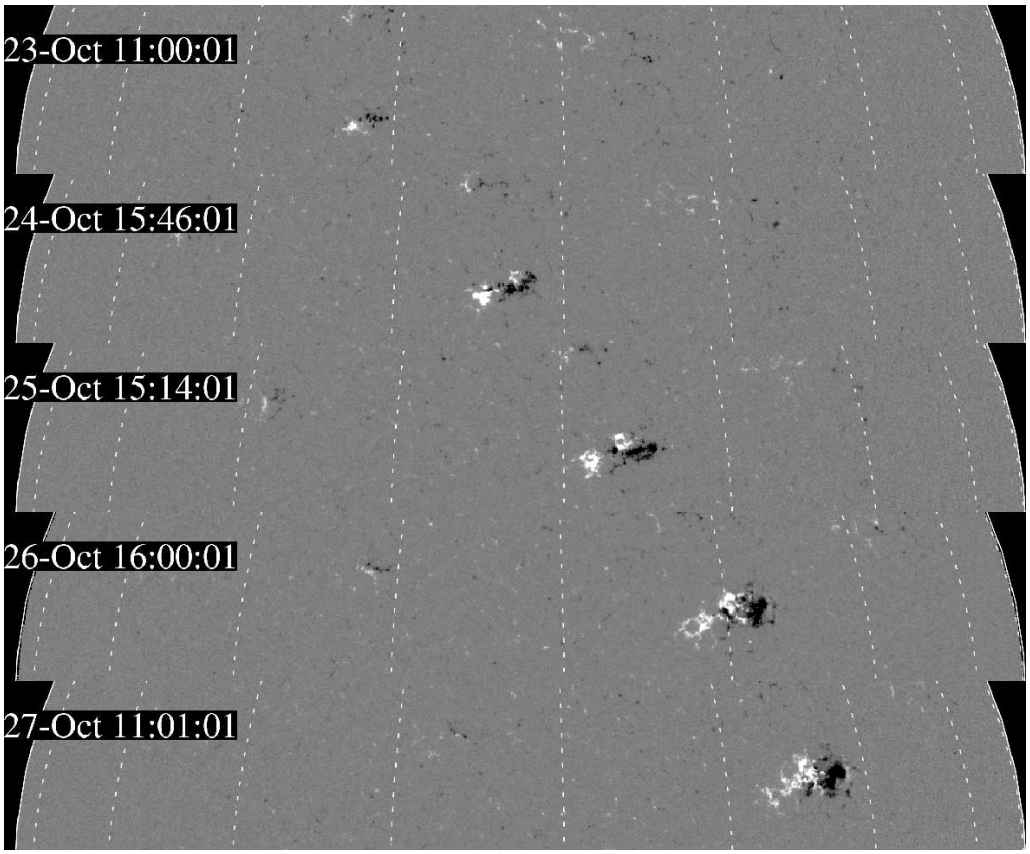

Figure 2.1: Evolution of active region AR 11029 from 23 to 27 October 2009. The figure shows a collage of magnetograms from the Michelson Doppler Imager (MDI) aboard the *Solar and Heliospheric Observatory*. The data show the line-of-sight magnetic field $\approx 120\,\mathrm{km}$ above the base of the photosphere, and the field values saturate at $\pm 500\,\mathrm{G}$. The times when the data are taken are indicated in the panels.

The NOAA solar active region AR 11029 emerged on 21-22 October 2009, began flaring on 24 October 2009, and rotated off the disk on 1 November 2009. Figure 2.1 shows the evolution of the photospheric magnetic field of AR 11029 between 23 and 27 October as observed by the Michelson Doppler Imager (MDI) aboard the *Solar and Heliospheric Observatory*. Over the period shown the region grew in size and complexity. A detailed summary of the region's evolution during its transit of the disk is given by Wheatland (2010).

Active region AR 11029 was highly active, producing a large number of small flares during a period of pronounced solar minimum (Livingston and Penn, 2009). In total 73 soft X-ray events are listed in the event catalogue[1] compiled from observations by the *Geostationary Operational Environmental Satellites* (*GOES*) during the region's transit of the disk. The majority are small *GOES* B-class events (peak 1-8 Å soft X-ray flux in the range $10^{-7}\mathrm{Wm}^{-2}$ to $10^{-6}\mathrm{Wm}^{-2}$). The largest is a *GOES* C2.2 event (peak soft X-ray flux of $2.2 \times 10^{-6}\mathrm{Wm}^{-2}$). No moderate sized M-class flares (peak flux $10^{-5}\,\mathrm{Wm}^{-2}$ to $10^{-4}\,\mathrm{Wm}^{-2}$) or large X-class flares (peak flux $\geq 10^{-4}\,\mathrm{Wm}^{-2}$) were produced.

The frequency and size of solar flares (by "size" we mean a measure of the magnitude *e.g. GOES* peak flux) are related by a well known power-law distribution (*e.g.* Akabane 1956; Hudson 1991). This distribution is universal in the sense that the same power law index is observed at all times, for events occurring over the entire Sun and for events that occur in different active regions (Wheatland, 2000). The power law in size reflects an underlying power law in the distribution of flare energies (Hudson, 1991).

[1]The *GOES* event catalogue is found online at http://www.ngdc.noaa.gov.

Analysis of the statistics of the flares produced by active region AR 11029 using the *GOES* event data provides strong evidence for a departure from the expected power-law frequency-peak flux distribution for this region (Wheatland, 2010). The region produced fewer large events than expected given the number of small events, based on the power law distribution, and hence did not appear to follow the universal distribution.

The upper panel of Figure 2.2 shows the frequency-peak flux distribution for the flares produced by AR 11029 as a cumulative histogram (diamonds), and the curves show two model distributions. The straight line corresponds to a power-law model distribution $P(S) \sim S^{-\gamma}$ where S is the peak flux and γ is the power-law index. The curved line corresponds to a power law model with an exponential rollover at large event sizes $P(S) \sim S^{-\lambda}\exp(-S/\sigma)$ where λ is the power-law index for small S and σ is the rollover size. The vertical dotted line shows the peak flux above which the two models are assumed to apply ($10^{-7}\,\mathrm{Wm}^{-2}$). There is a noticeable departure from the power law at the large end of the scale. Given the data, a Bayesian model comparison taking into account all events showed that the rollover model was favoured over the simple power-law model with an odds ratio[2] of ≈ 220 (Wheatland, 2010).

The absence of large flares was attributed by Wheatland (2010) to the region having insufficient energy to produce large events. In principle an upper bound on flare size must exist which reflects the finite energy stored in the active region's magnetic field (Hudson, 1991). However, it has proven difficult to observationally identify this effect in flare statistics (Hudson, 2007).

By determining the energy stored in the coronal magnetic field of active region AR 11029 it is in principle possible to test the hypothesis that the absence of large flares results from a lack of energy stored in the active region's magnetic field. The energy available for release in flares is called the free energy E_{f}, and is stored in the component of the coronal magnetic field generated by large scale electric currents in the corona (Priest and Forbes, 2002). Equivalently, the free energy is the energy in excess of the current free (potential) component *i.e.*

$$E_{\mathrm{f}} = E - E_0 = \frac{1}{2\mu_0}\int |\mathbf{B}|^2 dV - \frac{1}{2\mu_0}\int |\mathbf{B}_0|^2 dV, \tag{2.1}$$

where E is the total energy of the active region magnetic field $\mathbf{B}$, E_0 is the energy of the current free (potential) field $\mathbf{B}_0$, and the integrals are over the coronal volume of the active region. The potential field is uniquely defined in a finite volume by the normal component of the magnetic field on the closed surface surrounding this volume.

To determine E_{f} from Equation (2.1) requires the spatial distribution of $|\mathbf{B}|$ in the corona. This information is not provided by present observational methods but can be estimated from extrapolation of the photospheric magnetic field based on a force-free model (*e.g.* Régnier and Priest 2007; Thalmann, Wiegelmann, and Raouafi 2008). The linear force-free model cannot provide a reliable estimate of the free-energy due to the energy of the linear field being generally unbounded.

Force-free modelling encounters a number of problems in application to magnetogram data (De Rosa *et al.*, 2009). This appears to be primarily a result of the inconsistency between the force-free models and the boundary data. Whilst the corona may be close to force-free (Gary, 2001), the photosphere is not (Metcalf *et al.*, 1995; Gary, 2001). Wheatland and Régnier (2009) developed a procedure based on an implementation of the Grad-Rubin method for calculating nonlinear force-free fields (Wheatland, 2007) which addresses the inconsistency between the data and the model. This approach identifies a force-free magnetic field solution with boundary conditions close to, but not exactly matching, the magnetogram boundary conditions. The resulting "self-consistent" field may represent the coronal magnetic field. The self-consistency procedure can accommodate uncertainties in the boundary data (details of this method are given in Section 2.2). This method has previously been applied to vector magnetogram data without incorporating the uncertainties in

[2]The odds ratio is the relative probability that the data favours the rollover model over the power law model: a value of one indicates both models are equally likely, and a value of ≈ 220 indicates that the rollover model is ≈ 220 times more likely given the data (Jaynes and Bretthorst, 2003).

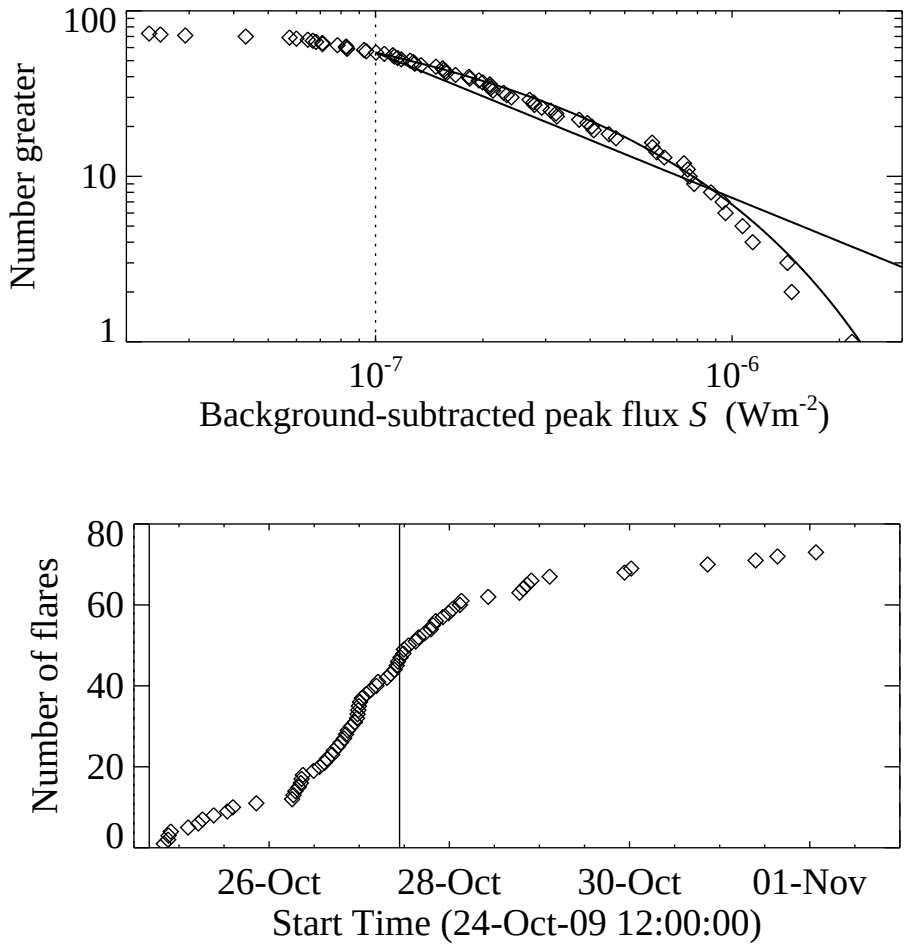

Figure 2.2: The upper panel shows the frequency-size distribution of soft X-ray flares for active region AR 11029 (Wheatland, 2010), plotted as a cumulative number distribution for the background subtracted peak soft X-ray flux of *GOES* events. The straight line shows a simple power law distribution, and the curved line shows a power law with an exponential rollover at large peak fluxes. The dotted vertical line shows the size threshold above which the models are assumed to apply ($10^{-7}\,\mathrm{Wm}^{-2}$). A Bayesian model comparison favours the rollover model to the straight power law with an odds ratio of ≈ 220 (Wheatland, 2010). The lower panel shows the cumulative number of *GOES* flares observed in active region AR 11029 versus time, between 24 October when the region began flaring, and 1 November when it rotated off the disk. The times when SOLIS/VSM and *Hinode*/SP magnetogram data are available are indicated in the lower panel by the solid vertical lines.

the data (Wheatland and Régnier, 2009), and has recently been applied with uncertainties (Wheatland and Leka, 2011).

In this chapter we use the Wheatland and Régnier (2009) self-consistency procedure to reconstruct the coronal magnetic field of AR 11029 from vector magnetogram data. The magnetograms are derived from spectropolarimetric data provided by the US National Solar Observatory's (NSO) Synoptic Optical Long term Investigations of the Sun Vector-SpectroMagnetograph (SOLIS/VSM), and the Solar Optical Telescope SpectroPolarimeter onboard the *Hinode* spacecraft (*Hinode*/SP). Based on the reconstructed coronal magnetic field we calculate the total energy stored in the active region and the free energy E_{f}, defined by Equation (2.1), and compare these results to a lower bound on the energy corresponding to the size of the largest observed *GOES* event produced by AR 11029.

This chapter is structured as follows. Section 2.2 provides background on nonlinear force-free models and the self-consistency method, and Section 2.3 explains the use of the SOLIS/VSM and *Hinode*/SP data. Section 2.4 explains the application of the force-free model to the SOLIS/VSM and *Hinode*/SP data and presents the results of the modelling. Section 2.5 discusses the results, and Section 2.6 presents the conclusions.

2.2 Background

2.2.1 Force-Free Modelling of the Coronal Magnetic Field

A force-free magnetic field is a solution[3] to the equations

$$\mathbf{B} \cdot \nabla \alpha = 0 \tag{2.2}$$

and

$$\nabla \times \mathbf{B} = \alpha \mathbf{B} \tag{2.3}$$

(Sturrock, 1994). Here $\mathbf{B}$ is the magnetic field vector and α is the force-free parameter, which is related to the electric current density $\mathbf{J} = \mu_0^{-1} \nabla \times \mathbf{B}$ by the relationship $\mathbf{J} = \alpha \mathbf{B}/\mu_0$.

Equations (2.2) and (2.3) are nonlinear in the general case (when α is a function of position, *i.e.* $\alpha = \alpha(\mathbf{r})$ where $\mathbf{r}$ is the position vector). The nonlinearity, and the mixed elliptic-hyperbolic character of the equations makes them difficult to solve, motivating a numerical approach. A version of the current-field iteration or Grad-Rubin approach, originally proposed by Grad and Rubin (1958), is used here (Wheatland, 2007).

The boundary conditions for solving the force-free equations are described by Grad and Rubin (1958). In the solar context, the boundary conditions are B_n, the component of the magnetic field normal to the photosphere and α_0, the value of α on the photosphere over one polarity of the field *i.e.* over the region where $B_n > 0$, or the region where $B_n < 0$. We refer to the two choices, defined by the two different polarities, as the P and N choices respectively.

On the scale of an active region the curvature of the photosphere is often ignored (Gary and Hagyard, 1990), and Equations (2.2) and (2.3) are solved in the Cartesian half space $z \geq 0$, where $z = 0$ is the photosphere. In this case $B_n = B_z$, and the force-free parameter α on the photosphere is defined by

$$\alpha_0 = \frac{1}{B_z} \left(\frac{\partial B_y}{\partial x} - \frac{\partial B_x}{\partial y} \right) \Bigg|_{z=0} . \tag{2.4}$$

The right hand side of Equation (2.4) may be estimated from photospheric vector magnetogram data, which we assume provides the vector components of $\mathbf{B}$ at $z = 0$.

The boundary value problem outlined in this section is for an infinite half space. To compute a numerical solution it is necessary to solve the equations on a finite grid of points. This introduces the problem that boundary conditions on $\mathbf{B}$ and α are unknown on the top and sides of the finite domain and force-free

[3] In this chapter when we refer to a "model" we mean the nonlinear force-free model defined by these equations. By "solution" we mean a solution to these equations, for specific boundary conditions.

extrapolation codes must deal with this problem. The code used here assumes the magnetic field is periodic in the x and y directions, and that the force-free parameter α is zero on the top and side boundaries (Wheatland, 2007). Equation (2.2) requires that α is constant along field lines, and hence field lines which leave the top or side of the box have α set to zero along their length. This approach deals with the missing boundary data on α and ensures that $\nabla \cdot \mathbf{J} = 0$ is satisfied in the volume. The handling of missing boundary data is a source of uncertainty for the force-free modelling performed here, and in particular we expect the free energy to be decreased by the removal of currents implied by setting α to zero. In addition, images of the solution introduced by the periodicity will affect the solution. The effect of this should be small when the computational domain is large so the region of interest is isolated from the boundaries.

2.2.2 A Self-Consistent Model of the Coronal Magnetic Field

Force-free modelling encounters problems when applied to photospheric magnetogram data (De Rosa *et al.*, 2009). Firstly, the iterative methods used to solve Equations (2.2) and (2.3) fail to strictly converge if large electric currents are present in the boundary data (De Rosa *et al.*, 2009). Secondly, methods using the formally correct boundary conditions given in Section 2.2.1 produce P and N solutions which differ both in terms of energy and field line connectivity. The second problem makes it difficult to estimate the energy of the region from the model because two solutions with different energy are obtained from the same magnetogram. These problems are in part due to noise in the data and uncertainties associated with the inversion of polarisation measurements to give boundary magnetic field values, errors in the resolution of the 180-degree ambiguity in the direction of the field transverse to the line-of-sight (see Section 2.3.1), and errors introduced by the process of estimating photospheric values of α. However the fundamental problem is likely the inconsistency between the force-free model and the magnetogram data (Metcalf *et al.*, 1995).

The self-consistency procedure developed by Wheatland and Régnier (2009) addresses the inconsistency between the boundary data and the force-free model. The method iteratively modifies the values of α on the boundary, which we denote α_0, until the P and N solutions agree. The self-consistency procedure can also take into account the uncertainties on α_0 which we denote σ. We refer to repeat applications of the method involving modifications of α_0 as self-consistency "cycles".

Here we give a brief outline of the self-consistency procedure (see Wheatland and Régnier (2009) or Wheatland and Leka (2011) for a detailed explanation). A single self-consistency cycle can be broken into three steps. The first step involves constructing the P and N solutions from the the boundary data $B_z(x, y)$ and $\alpha_0(x, y)$. The Grad-Rubin method, an iterative method for solving Equations (2.2) and (2.3) (Grad and Rubin, 1958) is used, with an implementation in code described by Wheatland (2007). In general the P and N solutions obtained differ indicating the boundary data are inconsistent with a force-free model.

The second step of a self-consistency cycle involves constructing a second set of α values on the boundary, which we denote α_1, based on the connectivity of the P and N solutions. For a force-free field the parameter α is constant along field lines (an implication of Equation (2.2)). Closed magnetic field lines connect points in the boundary with $B_z > 0$ to points with $B_z < 0$, which defines a mapping between regions of P polarity and N polarity. The mapping defined by the field lines of the P solution maps values of α_0 in the P polarity to the N polarity (since α is constant along field lines). This defines a second set of α values over the N polarity. Similarly the N solution maps values of α_0 from the N polarity to the P polarity, which defines a second set of α values over the P polarity. Combined the values of α_0 mapped by the P and N solutions cover the entire lower boundary and we denote this second set of values α_1. In general $\alpha_0(x, y) \neq \alpha_1(x, y)$ unless the boundary data are consistent with a force-free model. Uncertainties on α_1, which we denote σ_1, are constructed from σ in the same way that α_1 is constructed from α_0.

The third step involves constructing a new set of α values on the lower boundary based on α_0 and α_1. The self-consistency procedure treats α_0 and α_1 as two separate observations of α on the lower boundary and Bayesian probability is used to decide on the most probable value at each boundary point given the uncertainties σ and σ_1 (Jaynes and Bretthorst, 2003). Assuming the uncertainties σ (and by construction also σ_1) are Gaussian uncertainties, the new distribution of α on the lower boundary is

$$\alpha_{\rm new} = \frac{\alpha_0/\sigma^2 + \alpha_1/\sigma_1^2}{1/\sigma^2 + 1/\sigma_1^2}. \tag{2.5}$$

If all uncertainties are equal then $\alpha_{\rm new}$ is the average of the two values at each point *i.e.* $\alpha_{\rm new} = (\alpha_0 + \alpha_1)/2$. An important property of Equation (2.5) is that $\alpha_{\rm new}$ is unchanged under a global rescaling of the uncertainties σ and σ_1, *i.e.* Equation (2.5) is unchanged by the replacement $\sigma \rightarrow C\sigma$, where C is a constant. Hence the absolute value of σ at a point is not important: only the value with respect to other points is important.

The process of constructing P and N solutions and then applying Equation (2.5) (all three steps) is called a "self-consistency cycle". This procedure is iterated until $\alpha_0 = \alpha_1$ at all points in the boundary: a single force-free solution (a "self-consistent" solution) is obtained. In Wheatland and Régnier (2009) the self-consistency procedure was demonstrated in application to data from AR 10953, with uncertainties assumed equal at all boundary points, and in Wheatland and Leka (2011) the calculation was repeated with uncertainties derived from the spectropolarimetric inversion. This chapter follows the approach of Wheatland and Leka (2011).

2.3 Data and Modelling

Vector magnetogram data for active region AR 11029 are available from the ground based SOLIS Vector-SpectroMagnetograph (SOLIS/VSM), and from the Solar Optical Telescope SpectroPolarimeter on board the *Hinode* satellite (*Hinode*/SP). One SOLIS/VSM magnetogram per day is available for 24, 25, 26 and 28 October, and one *Hinode*/SP magnetogram per day is available from 24-29 October. All magnetograms are derived from observations of the Fe I ($630\mathrm{nm}$) multiplet which provides the vector magnetic field close to the level of the photosphere ($\approx 250\,\mathrm{km}$ above the base of the photosphere).

From the available data we use only the SOLIS/VSM magnetogram for 24 October and the *Hinode*/SP magnetogram for 27 October to derive the relevant boundary conditions for force-free modelling, as outlined in Section 2.2. We exclude the data for 28 and 29 October because the active region was too close to the limb, where projections effects become prohibitive. We exclude the *Hinode*/SP data for 24-26 October because for these days most of the active region lies outside the *Hinode*/SP field of view. We exclude the SOLIS/VSM data for 25 and 26 October because the magnetograms appear to contain significant systematic errors and are not suitable for force-free modelling. In particular the component of the magnetic field transverse to the line of sight shows a strongly preferred direction which we attribute to the result of systematic error.

The lower panel of Figure 2.2 shows the times of the acceptable magnetogram observations (solid vertical lines) compared with the flare history of the region. The magnetogram data requires ≈ 10 minutes of integration time in the case of SOLIS/VSM and ≈ 60 minutes of integration time in the case of *Hinode*/SP. The region first began flaring on 24 October producing several small *GOES* A-class and B-class flares, and the SOLIS/VSM magnetogram data are taken on this day. The flaring rate for the region peaked on 26 and 27 October and the *Hinode*/SP magnetogram data are obtained during this interval.

2.3.1 SOLIS/VSM Data

The National Solar Observatory SOLIS/VSM provides Milne-Eddington inverted vector magnetograms, and "Quicklook" data consisting of initial estimates of the vector magnetic field produced prior to Milne-Eddington inversion (Henney, Keller, and Harvey, 2006). Both full disk magnetograms and cropped data centred on individual active regions are available online[4]. The online data provide the magnetic field vector

[4] See http://solis.nso.edu.

close to the photosphere in terms of a line-of-sight component and a component transverse to the line of sight (Henney, Keller, and Harvey, 2006). The transverse component is further decomposed into a magnitude and direction defined by the azimuthal angle. The inversion is performed by the NSO and details are given in Henney, Keller, and Harvey (2006).

The magnetogram for 24 October is obtained at $16\colon 05\,(\mathrm{UT})$ and is 236×236 pixels in size with a spatial resolution of $1.1''$ per pixel. The magnetogram covers an area of $267'' \times 267''$ corresponding to $195 \times 196\,\mathrm{Mm}$ on the photosphere. The NSO also provides Quicklook data for the same day. Over regions of the photosphere where the magnetic field is weak there are gaps in the Milne-Eddington data where inversion in not performed due to a poor signal to noise ratio. We embed Quicklook data directly into the Milne-Eddington data to fill these gaps, following the advice provided by the NSO[5].

As explained in Section 2.2 force-free modelling is performed in a locally flat Cartesian coordinate system defined on the photosphere, and we refer to this coordinate system as helioplanar coordinates. The magnetogram is provided on a uniform grid on a plane perpendicular to the line of sight. We map the magnetogram to a helioplanar system using the transformations given in Venkatakrishnan, Hagyard, and Hathaway (1988). The helioplanar coordinate system is defined on a plane tangent to the solar surface at a point at the centre of the active region. The axes of this system are oriented such that the x and y axes align with solar west and north respectively, and the z axis is normal to the photosphere. Owing to projection effects after mapping, the grid on which the magnetic field is defined is no longer regularly spaced. We regrid the magnetogram onto a larger (in number of grid points) uniform grid with the same spatial resolution ($1.1''$ per pixel) as the original data. Since the active region is close to disk centre on 24 October the projection effects are small.

The spectropolarimetrically derived azimuthal angle contains an inherent 180° ambiguity (Landi Degl'Innocenti and Landolfi, 2004) which must be resolved to determine the magnetic field components (B_x, B_y and B_z) needed to derive boundary conditions for force-free modelling. Several procedures exist for resolving the 180° ambiguity (see Metcalf *et al.* 2006 and references therein), and here we use the "minimum energy" method developed by Metcalf (1994). This method determines the azimuthal angle by requiring the ambiguity-resolved field to minimise $|\nabla \cdot \overline{\mathbf{B}}| + |\bar{J}_z|$ over the magnetogram, where $\overline{\mathbf{B}}$ and $\overline{J}_z$ are non-dimensionalised versions of $\mathbf{B}$ and J_z (see Section 2.3.4 for details of the non-dimensionalisation.) The optimal magnetic field configuration is found using the general optimisation procedure of simulated annealing (Press *et al.*, 2007). We note that the NSO/SOLIS provides ambiguity-resolved data using a different resolution method (Georgoulis, 2005), but we have chosen to perform this step again using the minimum energy procedure.

The boundary conditions for force-free modelling are the component of the magnetic field normal to the photosphere, which corresponds to the B_z values in the regridded magnetogram, and the force-free parameter α on the photosphere derived from the values of B_x and B_y in the magnetogram using Equation (2.4). The partial derivatives in Equation (2.4) are approximated using centred differencing (Press *et al.*, 2007). The boundary values on α are set to zero at points where $|B_z| < 0.01 \times \max(|B_z|)$ because the ratio J_z/B_z is inaccurate in regions where B_z is small.

The final boundary conditions after projection and regridding are shown in Figures 2.3 and 2.4. Figure 2.3 shows the boundary conditions for B_z (upper panel), and the boundary conditions for J_z (lower panel). Figure 2.4 shows the force-free parameter α_0, and the signal-to-noise ratio $|\alpha_0|/\sigma$ for α_0 where σ represents the approximate uncertainty in the α_0 value estimated using the B_z boundary value, as explained in Section 2.3.4. In both Figures 2.3 and 2.4, the data saturate at a particular threshold value which is below the maximum in the data, by which we mean all points above the threshold appear with the same colour. This is done to provide a good contrast between large and small data values, and to diminish the appearance of outliers. For the panels showing J_z and α_0 only points where the signal-to-noise ratio $|\alpha_0|/\sigma$ is three standard deviations above the mean signal-to-noise ratio are represented, points where $|\alpha_0|/\sigma = 0$ are excluded when computing the mean and standard deviation. This criterion is chosen because it is independent of the magnitude of σ which is arbitrary for the SOLIS/VSM data (see Section 2.3.4). Only the central portion of the data is shown in the two panels because the boundary data values (B_z, J_z and α_0) outside the

[5] See the introduction to SOLIS/VSM data at http://solis.nso.edu/vsm/vsm_image_info3.html.

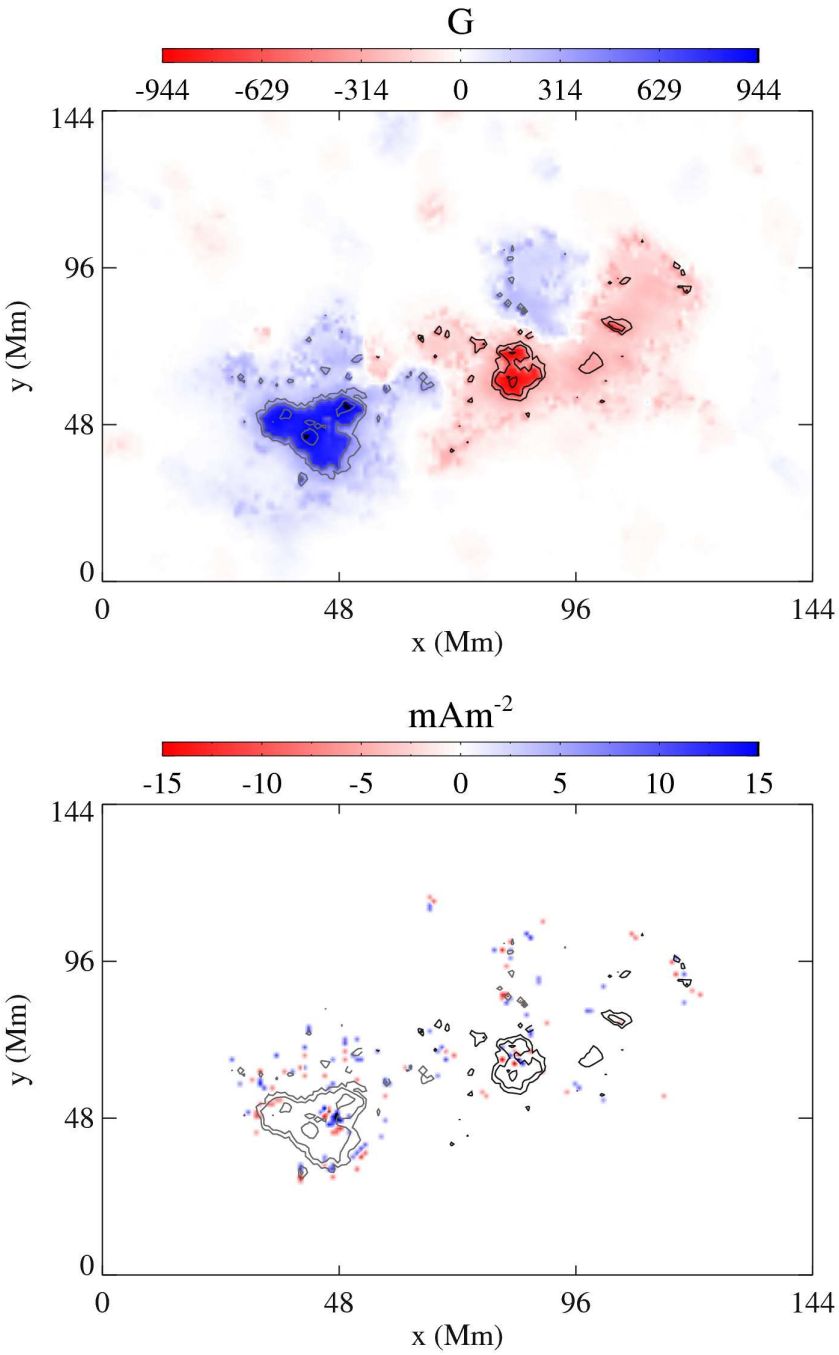

Figure 2.3: The central part of part of the SOLIS/VSM vector magnetogram data for 24 October. The upper panel shows B_z and the lower panel shows J_z. The data are coloured blue when positive, white when zero, and red when negative. Contours of B_z are superimposed on the data, with contours separated by intervals of 300 G. The contours are black where $B_z < 0$ and light grey where $B_z > 0$. The values of B_z (upper panel) have been saturated at ± 944 G with a maximum value of 961 G. The values of J_z (lower panel) have been saturated at $\pm 15\,\mathrm{mAm}^{-2}$ with a maximum value of $23\,\mathrm{mAm}^{-2}$. In the lower panel only points where $|\alpha_0|/\sigma$ is three standard deviations above the mean are shown.

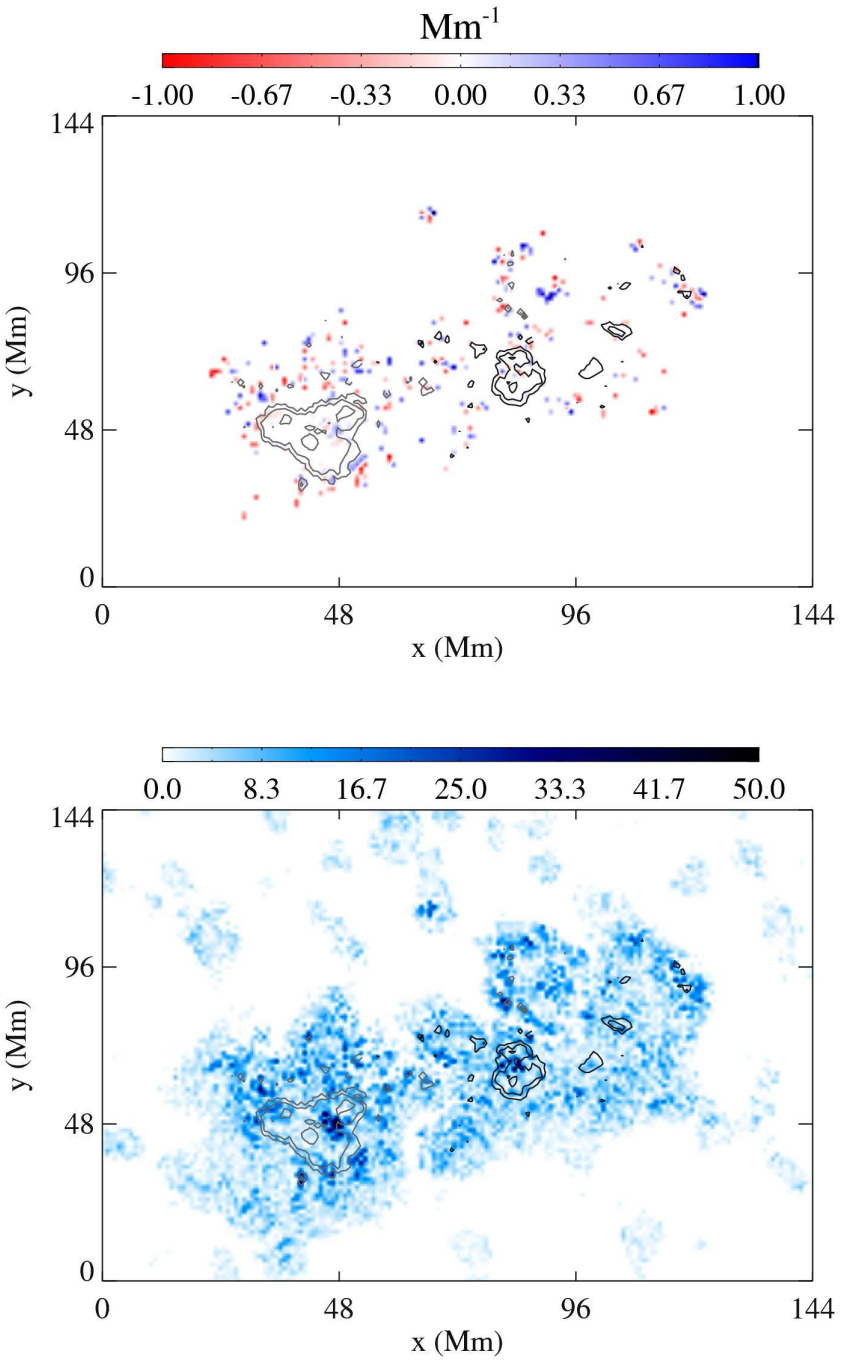

Figure 2.4: Boundary conditions on the force-free parameter obtained from the SOLIS/VSM vector magnetogram data for 24 October. The upper panel shows α_0 and the lower panel shows the signal to noise ratio $|\alpha_0|/\sigma$. The data are coloured blue when positive, white when zero, and red when negative. Contours of B_z are superimposed on the data, with the contours separated by 300 G. The contours are black where $B_z < 0$ and light grey where $B_z > 0$. The values of α_0 (upper panel) have been saturated at $\pm 1\,\mathrm{Mm}^{-1}$ with a maximum value of $3.7\,\mathrm{Mm}^{-1}$. The values of $|\alpha_0|/\sigma$ (lower panel) have been saturated at 50 with a maximum value of 67. In the upper panel only points where $|\alpha_0|/\sigma$ is three standard deviations above the mean are shown.

central region are comparatively small and are not visible with the chosen scale.

2.3.2 *Hinode*/SP Magnetogram Data

The *Hinode*/SP vector magnetogram data for 27 October is derived from spectropolarimetric data from the Solar Optical Telescope/SpectroPolarimeter aboard the *Hinode* satellite (Kosugi *et al.*, 2007; Tsuneta *et al.*, 2008). The "fast-scan" map obtained at $10\colon 45\,(\mathrm{UT})$ is spatially sampled at $0.32''$, and covers a relatively small $360'' \times 164''$ field of view. The data are inverted using the High Altitude Observatory (HAO) Milne-Eddington inversion code (Skumanich and Lites (1987); Lites and Skumanich (1990); Lites *et al.* (1993)), which has been modified for *Hinode*/SP data (revised code courtesy B. Lites, HAO/NCAR). Ambiguity resolution is performed using an implementation[6] of the minimum energy procedure (Leka, Barnes, and Crouch, 2009).

For the *Hinode*/SP data for 27 October uncertainties in the three components of the magnetic field $(\sigma_x, \sigma_y, \sigma_z)$ are derived during the Milne-Eddington inversion. These are based on the uncertainty in the χ^2 fit of the synthetic Stokes profiles to the observed Stokes profiles. The uncertainties are then propagated through the projection, regridding and ambiguity resolution to derive uncertainties for α_0. These uncertainties are a measure of how well the artificial Milne-Eddington profiles fit the observed profiles. They do not take into account the approximation of the Milne-Eddington atmosphere or systematic errors in the observations of the Stokes profiles. Therefore they may be considered lower bounds to the real uncertainties. Some parameter-dependence is introduced into the method of simulated annealing by the choice of a "cooling schedule" (Press *et al.*, 2007). We note that some data points are particularly sensitive to the choice of schedule, but overall the large scale structure of the ambiguity-resolved magnetogram appears independent of the choice. Large uncertainties are assigned to points which depend strongly on the choice of cooling schedule to reflect this parameter dependence.

The resulting vector magnetic components and uncertainties from the *Hinode*/SP data are re-mapped to a helioplanar $1''$ grid. The *Hinode*/SP field of view is small and only covers the main portion of the active region. As explained in Section 2.2 when performing force-free modelling it is important to isolate the region of interest from the boundaries to limit the influence of the boundaries on the solution. As with other studies involving *Hinode*/SP data (*e.g.* Wheatland and Leka 2011; De Rosa *et al.* 2009) the field of view is expanded by adding line-of-sight data from the Michelson Doppler Imager on the *Solar and Heliospheric Observatory* (Scherrer *et al.*, 1995) around the *Hinode*/SP data. A map of B_z is constructed using a potential field matching the observed line-of-sight magnetic field values in the boundary, and this is also remapped onto a $1''$ grid. After coalignment between the two data sources, an apodising function is applied at the boundaries of the two data sets to ensure a smooth transition between data values. This procedure follows Wheatland and Leka (2011), and improves upon a method used in De Rosa *et al.* (2009). The final size of the boundary data is 440×300 pixels, covering a region on the photosphere of size $320 \times 220\,\mathrm{Mm}$.

The data are shown in Figures 2.5 and 2.6. The vertical magnetic field B_z (upper panel) and vertical current density J_z (lower panel) are shown in Figure 2.5. The presentation of the data follows the format used in Figures 2.3 and 2.4. Approximate uncertainties σ in the α_0 values are provided by the spectropolarimetric inversion, for the *Hinode*/SP data points. Figure 2.6 shows the force-free parameter α_0 (upper panel) and the signal-to-noise ratio $|\alpha_0|/\sigma$ (lower panel). For the panels showing J_z and α_0 only points where the signal to noise ratio $|\alpha_0|/\sigma$ is three standard deviations above the mean signal-to-noise ratio are represented, points where $|\alpha_0|/\sigma = 0$ are excluded when computing the mean and standard deviation. Only the central portion of the data is shown in the two panels because the boundary data values (B_z, J_z and α_0) outside the central region are comparatively small and are not visible with the chosen scale.

[6] Available at http://www.cora.nwra.com/AMBIG/.

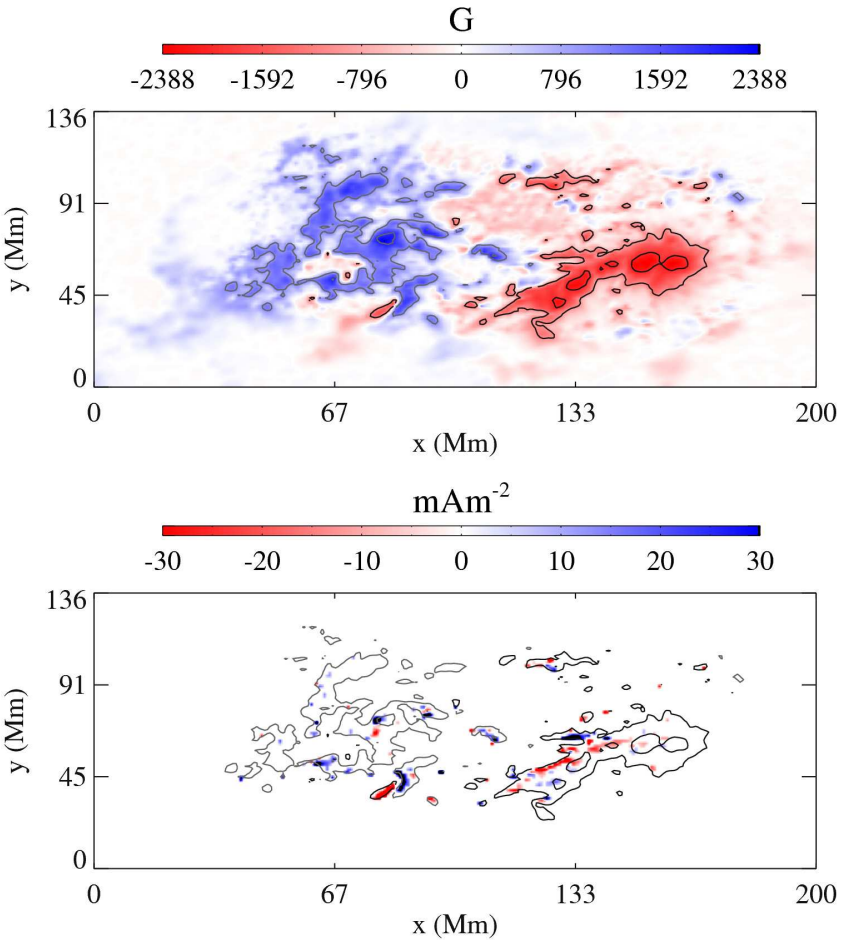

Figure 2.5: The central part of the *Hinode*/SP vector magnetogram data for 27 October. The upper panel shows B_z and the lower panel shows J_z. The data are coloured blue when positive, white when zero, and red when negative. Contours of B_z are superimposed on the data, with contours separated by intervals of 1000 G. The contours are black where $B_z < 0$ and light grey where $B_z > 0$. The values of B_z (upper panel) have been saturated at ± 2448 G with a maximum value of 2388 G. The values of J_z (lower panel) have been saturated at $\pm 30\,\mathrm{mAm}^{-2}$ with a maximum value of $144\,\mathrm{mAm}^{-2}$. In the lower panel only points where $|\alpha_0|/\sigma$ is three standard deviations above the mean are shown.

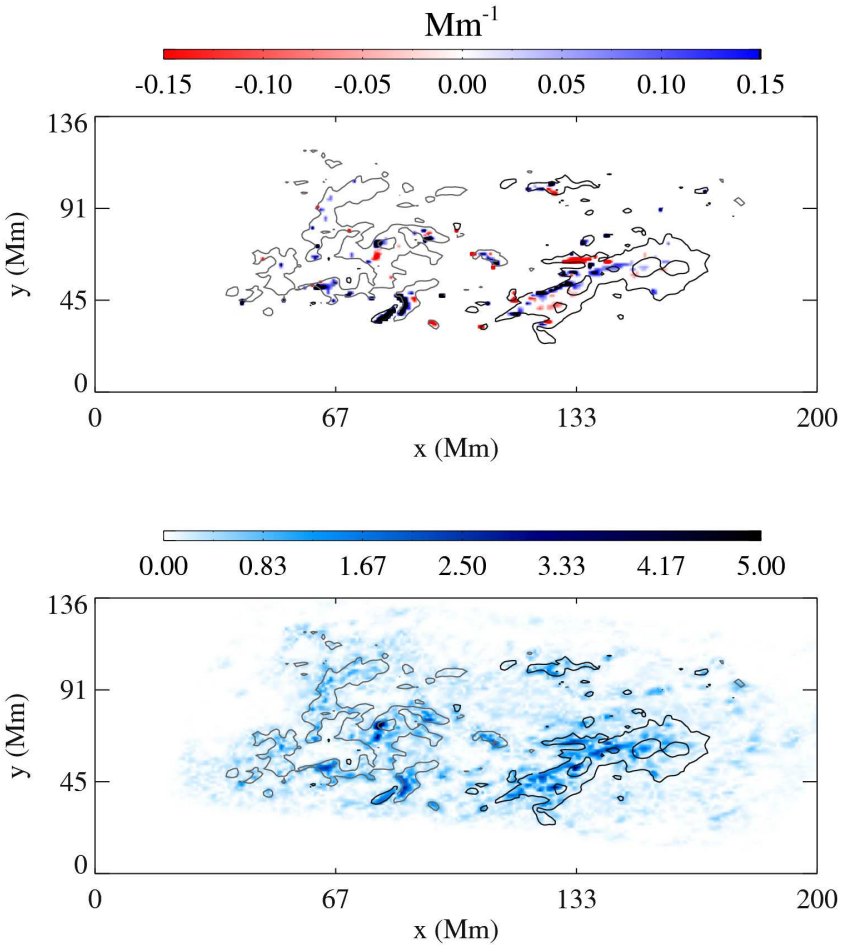

Figure 2.6: Boundary conditions on the force-free parameter obtained from the *Hinode*/SP vector magnetogram data for 27 October. The upper panel shows α_0 and the lower panel shows the signal to noise ratio $|\alpha_0|/\sigma$. The data are coloured blue when positive, white when zero, and red when negative. Contours of B_z are superimposed on the data, with the contours separated by $1000\,\mathrm{G}$. The contours are black where $B_z < 0$ and light grey where $B_z > 0$. The values of α_0 (upper panel) have been saturated at $\pm 0.15\,\mathrm{Mm}^{-1}$ with a maximum value of $1.9\,\mathrm{Mm}^{-1}$. The values of $|\alpha_0|/\sigma$ (lower panel) have been saturated at five with a maximum value of 5.4. In the upper panel only points where $|\alpha_0|/\sigma$ is three standard deviations above the mean are shown.

2.3.3 Flux Balance

The integral of B_z over the magnetogram defines the net magnetic flux across the observed region of the photosphere. If the net flux is zero, then the magnetogram is said to be flux balanced. Flux balance is not essential for the force-free modelling procedure used here, but if the flux is unbalanced a greater number of field lines leave the top and sides of the computational domain in order to satisfy $\nabla \cdot \mathbf{B} = 0$ globally. As discussed in Section 2.2 boundary conditions are not known on the top and side boundaries of the domain and the force-free code sets $\alpha = 0$ along field lines which leave the domain via these boundaries (Wheatland, 2007). The currents and therefore the free energy tend to be reduced by this procedure. The effect of the boundaries on the energy estimates is likely to be less pronounced if the magnetogram is flux balanced.

A practical measure of flux balance is the relative flux balance, defined as

$$\Phi_B = \frac{\int B_z dA}{\int |B_z| dA} \tag{2.6}$$

where the integrals are over the magnetogram area. The integrals in Equation (2.6) are evaluated numerically using the two-dimensional trapezoidal rule. The results are listed in the right-hand column in Table 2.1.

We consider a Φ_B of less than 1% acceptable. The *Hinode*/SP magnetogram for 27 October meets this requirement, but the SOLIS/VSM magnetogram for 24 October does not. To flux balance the SOLIS/VSM data a buffer region of constant B_z is added around the border of the magnetogram. The magnitude of the field in the buffer region satisfies $|B_z| < 0.01 \times \max(|B_z|)$, and hence the buffer region is considered weak field by our previous definition (see Section 2.3.1). In the buffer the magnitude of B_z is $9.3\,\mathrm{G}$ (the weak field threshold is $9.6\,\mathrm{G}$), and the value of α_0 is set to zero everywhere in the buffer. The total size of the magnetogram with the buffer added is 270×270 grid points, and the resolution of the data remains the same ($1.1''$ per pixel). The final size of the region including the flux buffer is $222 \times 222\,\mathrm{Mm}$.

2.3.4 Phenomenological Uncertainties for SOLIS/VSM Data

Uncertainties are provided with the *Hinode*/SP data based on spectropolarimetric inversion of the data (as explained in Section 2.3.2), but are not available for the SOLIS/VSM data for 24 October. Instead we make a simple estimate for the uncertainties based on the magnitude of B_z at each boundary point. Specifically we introduce a phenomenological uncertainty defined by

$$L_x \sigma(x,y) = \begin{cases} 0.01 & \text{for the flux buffer region;} \\ B_\mathrm{m}/|B_z(x,y)| & \text{where } |B_z/B_\mathrm{m}| > 0.01 \\ 100 & \text{where } |B_z/B_\mathrm{m}| < 0.01 \end{cases} \tag{2.7}$$

Equation (2.7) is written in non-dimensional units. The magnetic field is scaled by $B_\mathrm{m} = \max(|B_z|)$, the maximum value of $|B_z|$, and σ is scaled by L_x, the transverse length of the magnetogram. Points in the flux buffer are assigned a small constant uncertainty, which ensures $\alpha_0 = 0$ for this region during the self-consistency procedure. A relatively large uncertainty ($L_x\sigma = 100$, in non-dimensional units) is assigned to points in weak field regions where α_0 has been set to zero (see Section 2.3.1).

The phenomenological scaling $\sigma(x,y) \sim 1/|B_z(x,y)|$ for the SOLIS/VSM data region is based on inspection of the inversion-based uncertainties for the *Hinode*/SP data for 27 October.

Figure 2.7 shows $P(\sigma, |B_z|)^{1/4}$, where $P(\sigma, |B_z|)$ is the distribution of the inversion-based uncertainties for the *Hinode*/SP data for 27 October over field strength and uncertainty in α_0 *i.e.* the fraction of points with field value $|B_z|$ and uncertainty σ. We have applied a nonlinear scaling to the distribution so that strong field regions with small values of $P(\sigma, |B_z|)$ are visible. The solid line shows $\sigma = 100\,\mathrm{Mm}^{-1}/|B_z|$ with

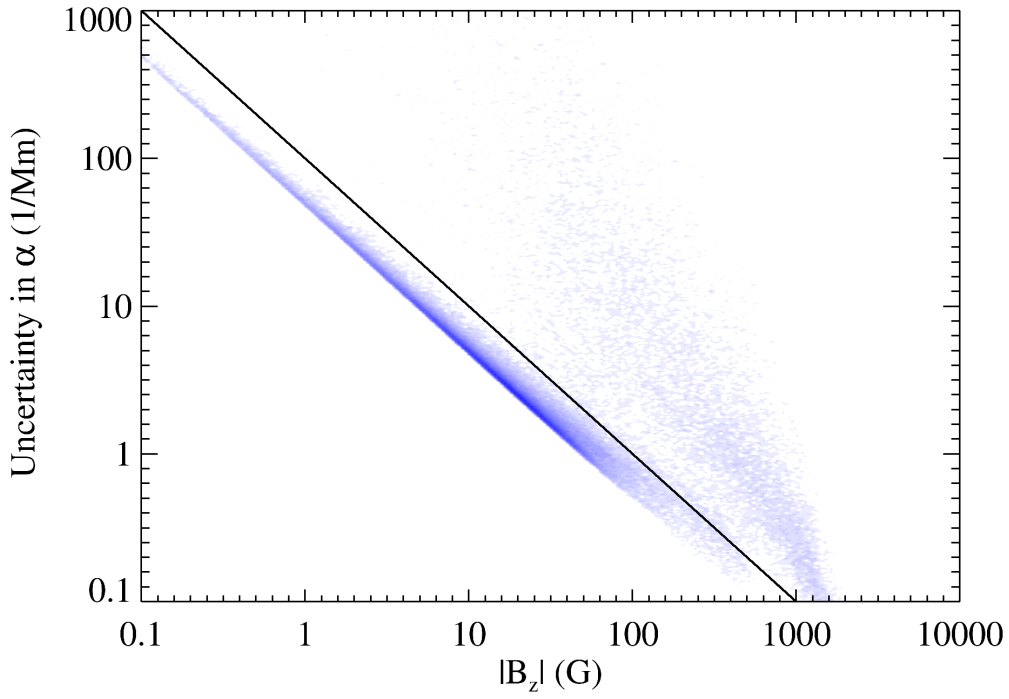

Figure 2.7: The relationship between the uncertainties on the boundary values of the force-free parameter derived from the spectropolarimetric inversion and $|B_z|$ for the *Hinode*/SP data for 27 October. The solid line is to illustrate $\sigma \sim 1/|B_z|$ dependence and the position of the line has been chosen arbitrarily. There is a noticeable departure from the $\sigma \sim 1/|B_z|$ scaling for large values of $|B_z|$.

B_z in gauss, to illustrate $\sigma \sim 1/|B_z|$ dependence for comparison. The choice of the factor $100\,\mathrm{Mm}^{-1}$ is arbitrary. The figure shows that the simple phenomenological scaling implied by Equation (2.7) is accurate for a majority of data points, although there is notable departure for large values of $|B_z|$.

It should be noted that, according to Equation (2.5), the exact magnitude of the uncertainties is not important for the self-consistency averaging procedure (see discussion following Equation (2.5)). Only the relative size of uncertainties at different points is important. Although, due to the departure from the $\sigma \sim 1/|B_z|$ scaling for large values of $|B_z|$ we expect that the uncertainties in strong field regions are underestimated relative to weak field regions.

2.3.5 Force-Free Modelling Using SOLIS/VSM and *Hinode*/SP Data

Force-free solutions are calculated using the code of Wheatland (2007) and the self-consistency procedure of Wheatland and Régnier (2009). The boundary conditions derived from the SOLIS/VSM and *Hinode*/SP vector magnetogram data described in Sections 2.3.1 and 2.3.2 are used. The initial magnetic field for the Grad-Rubin iteration is a potential field calculated using a Fourier solution to Poisson's equation. The computational domain used is a uniform three dimensional Cartesian grid with transverse dimensions (*i.e.* the x and y dimensions) matching the dimensions of the magnetogram which forms the lower boundary at $z = 0$. The vertical dimension (*i.e.* z) is 128 points high for the SOLIS/VSM data and 200 points high for the *Hinode*/SP data. The resulting dimensions of the grids are $270 \times 270 \times 128$ points for 24 October, and $440 \times 300 \times 200$ points for 27 October. The grid spacing is uniform in each direction. We summarise the size, maximum magnetic field, and flux balance of the data in Table 2.1.

Table 2.1: Summary of magnetogram data/computational data domain sizes, field strength parameters, and relative flux balance Φ_B (see Equation (2.6)) for the computational models of AR 11029.

Data source	Date	$N_x \times N_y \times N_z$	$L_x \times L_y \times L_z$ (10^8 m)	$B_\mathrm{m} = \max(\lvert B_z \rvert)$ (G)	Φ_B (%)
SOLIS/VSM	Oct. 24	$236 \times 236 \times 128$	$2.0 \times 2.0 \times 1.1$	962	11
SOLIS/VSM (buffered)	Oct. 24	$270 \times 270 \times 128$	$2.2 \times 2.2 \times 1.1$	962	0.02
Hinode/SP	Oct. 27	$440 \times 300 \times 200$	$3.2 \times 2.2 \times 1.5$	2448	0.4

2.4 Results

This section presents the results of the force-free modelling of active region AR 11029. Section 2.4.1 discusses the results when the force-free code is applied to the SOLIS/VSM data for 24 October to construct P and N solutions without using the self-consistency procedure. Section 2.4.2 discusses the application of the self-consistency procedure to the same data. Section 2.4.3 discusses the application of the self-consistency procedure to the *Hinode*/SP data for 27 October.

2.4.1 Construction of P and N Solutions Directly from Magnetogram Data for 24 October

We construct P and N solutions for AR 11029 directly from the magnetogram data for 24 October. In this section we do not apply the self-consistency procedure. To construct the P and N solutions 50 Grad-Rubin iterations are used beginning with a potential field constructed from B_z.

In application to the magnetogram data the Grad-Rubin procedure does not strictly converge for the P and N solutions. The energy of the magnetic field at each iteration provides a way to examine the convergence. Figure 2.8 shows the magnetic energy, E, in units of the energy of the potential field, E_0, over successive

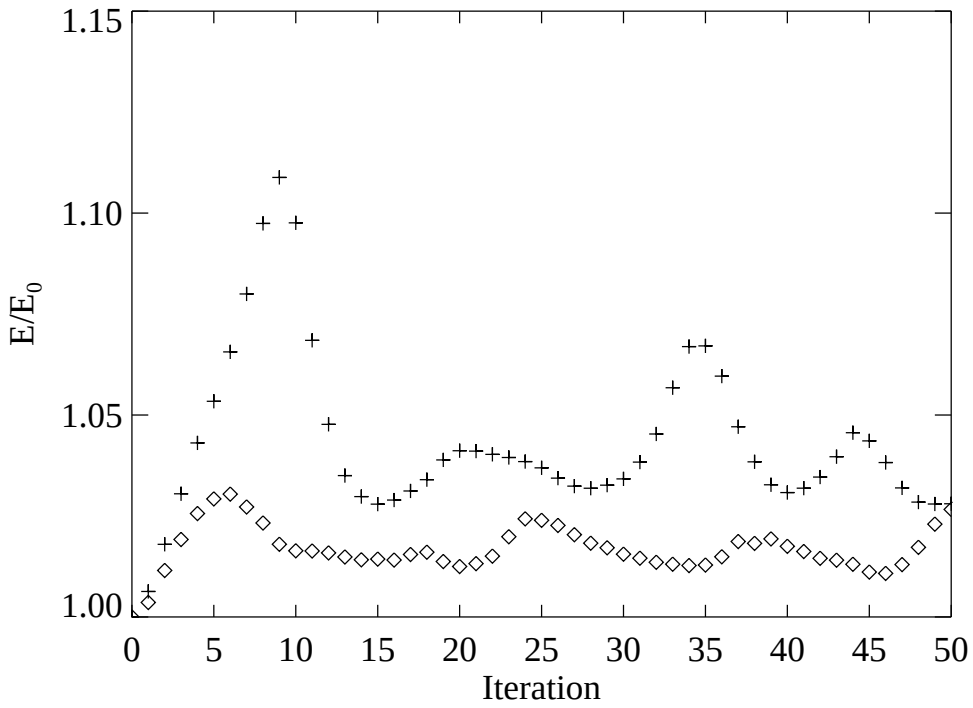

Figure 2.8: Results for the construction of P and N solutions directly from the SOLIS/VSM magnetogram data for 24 October. The total magnetic energy is shown (as a fraction of the energy of the potential field) for the P solution (plus signs) and the N solution (diamonds) over 50 Grad-Rubin iterations starting from a potential field. The oscillations in the energy occur because of large localised currents in the boundary data.

Grad-Rubin iterations for both the P and N solutions. The energy of the two solutions behaves similarly. Initially the total energy increases beyond the energy of the potential field and then begins oscillating after about 15 iterations for the P solution and after about ten iterations for the N solution. This oscillatory behaviour is typical in situations where the Grad-Rubin method does not strictly converge, and may be attributed to large currents at certain points in the boundary. This is confirmed by inspecting visualisations of field lines at successive Grad-Rubin iterations. For the P and N solutions for the 24 October data we observe that the longest field lines which stretch high into the computational volume (and carry significant currents) change over successive iterations. The field in the lower part of the volume is static, and the field in the middle of the volume displays small oscillations.

We estimate the energy of the P and N solutions by averaging the energy over several Grad-Rubin iterations. After 15 Grad-Rubin iterations the P solutions stops changing systematically and begins oscillating so we estimate the energy of the P solution by taking the average energy of the field over successive Grad-Rubin iterations starting from iteration 15 (*i.e.* we take $E_P = \mathrm{mean}(E_{15}, E_{16}, ..., E_{50})$, where E_i is the energy of the P solution after i Grad-Rubin iterations). We do the same for the N solution, except we start the average from iteration ten (*i.e.* $E_N = \mathrm{mean}(E_{10}, ..., E_{50})$). We also compute the free energy $E_\mathrm{f} = E - E_0$, for $E = E_P$ and $E = E_N$. The results are listed in Table 2.2.

The upper panel of Figure 2.9 shows a visualisation of the magnetic field after 20 Grad-Rubin iterations (the lower panel is discussed in Section 2.4.2). The magnetic field lines for the P solution (blue curves) and the N solution (red curves) are displayed in the upper panel. The fields are viewed looking down on the photosphere, which is coloured blue where $B_z > 0$ and red where $B_z < 0$. The panel shows some qualitative difference between the P and N solutions.

The visualisation of the field lines also reveals the extent to which the missing information on the boundaries

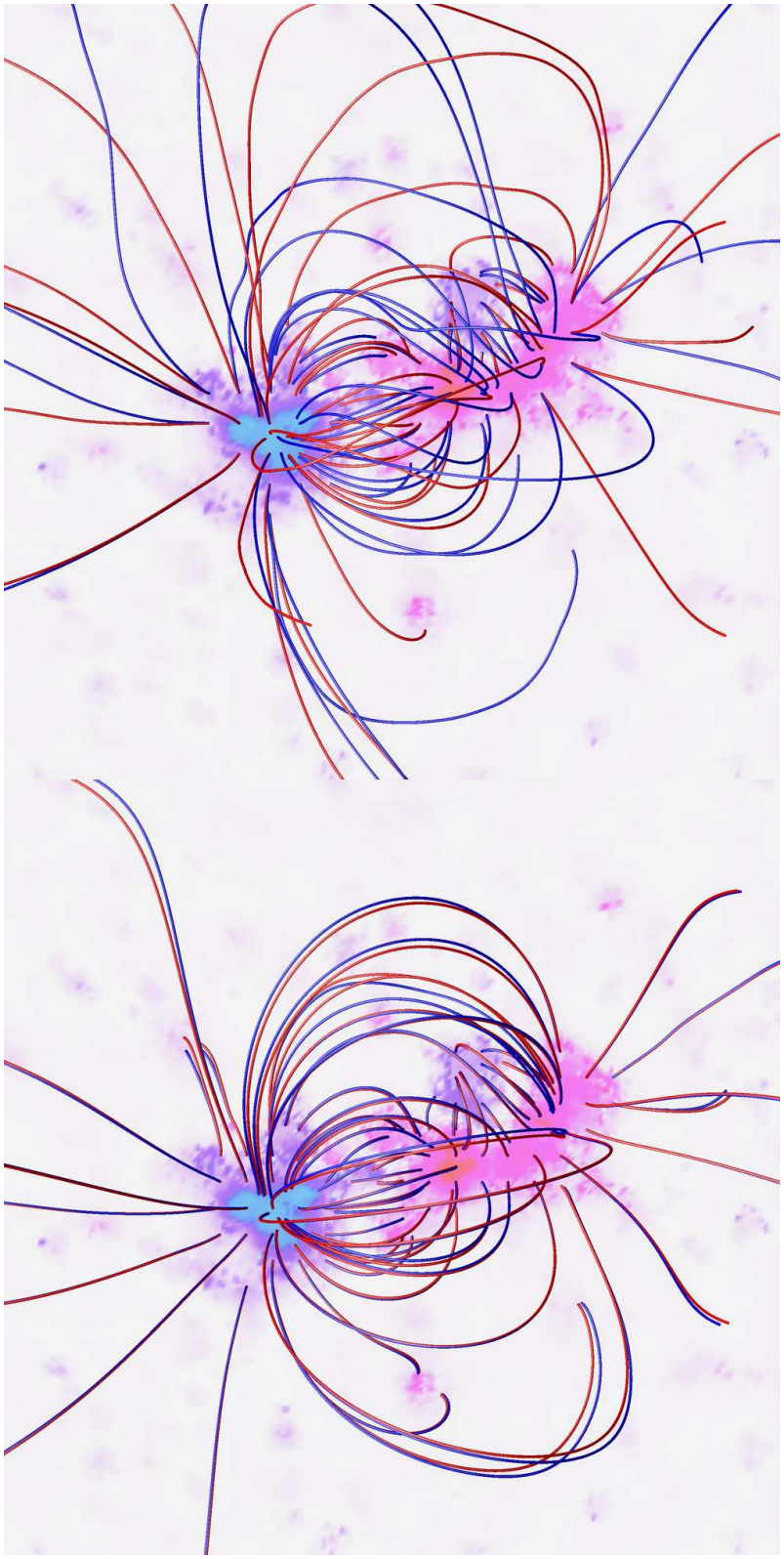

Figure 2.9: Nonlinear force-free models of the coronal magnetic field constructed from the SOLIS/VSM vector magnetogram data for 24 October. The P solution (blue field lines) and N solution (red field lines) are shown viewed looking down on the photosphere. The upper panel shows the two solutions constructed from the original vector magnetogram boundary data (with a flux buffer added) using 20 Grad-Rubin iterations. The lower panel shows the solutions after ten self-consistency cycles with 20 Grad-Rubin iterations per cycle. The photosphere is coloured blue where $B_z > 0$ and red where $B_z < 0$. This figure illustrates the achievement of self-consistency: the P and N solutions in the upper panel are dissimilar but in the lower panel are very similar.

Table 2.2: Energy estimates for the P and N solutions constructed directly from the SOLIS/VSM magnetogram data for AR 11029 on 24 October.

Solution	E (10^{31} erg)	E_0 (10^{31} erg)	$E_{\rm f} = E - E_0$ (10^{30} erg)
P	9.98	9.62	3.6
N	9.77	9.62	1.5

influences the solution. It can be seen from the upper panel of Figure 2.9 that both solutions have field lines which cross the side boundaries. Many field lines connected to the trailing positive spot leave the box. However, a significant part of the active region field involves closed field lines. It is unlikely the boundary has a large influence on the final energy.

The results in this section illustrate difficulties associated with obtaining estimates for the total and free energy using the nonlinear force-free model. The Grad-Rubin iteration does not strictly converge, due to strong currents, which introduces a degree of arbitrariness in the energy estimate since the energy depends on the choice of when to stop the iteration process. Compared with the total energy the oscillations in the total energy are small, but these oscillations in the total energy translate into large oscillations in the free energy, because $E \gg E_{\rm f}$. The force-free energy estimates may be regarded as approximate (order of magnitude) estimates of the free energy. Based on the results in Table 2.2 we estimate that the free energy is $\approx 3 \times 10^{30}$ erg.

2.4.2 Construction of Self-Consistent Solutions for 24 October

The self-consistency procedure is applied to the SOLIS/VSM vector magnetogram boundary data for 24 October. Initially, we use ten self-consistency cycles with 20 Grad-Rubin iterations per cycle (P and N solutions are constructed using 20 Grad-Rubin iterations, and this is repeated for ten self-consistency cycles, with the α_0-values updated using Equation (2.5) at the end of each cycle).

The energy of the P and N solution at each self-consistency cycle may be used to monitor the convergence of the procedure. At the end of each cycle (after 20 Grad-Rubin iterations for both P and N solutions), the total magnetic energy, E, for the solutions is calculated. Figure 2.10 shows the evolution of E/E_0 with cycle for the P and N solutions. Initially the two energies are different (as discussed in Section 2.4.1 and shown in Table 2.2) but after three cycles the energy approaches a single value. After ten cycles $E/E_0 = 1.0047$ for the P solution and $E/E_0 = 1.0044$ for the N solution which is lower than the energy of either the initial P or N solutions. The small difference between the energies of the P and N solutions translates into a difference of $\approx 7\%$ in the free energy. In dimensional units the free energy is about 4×10^{29} erg. The total energy of the final self-consistent solution E, the energy of the potential field E_0, and the free energy of the final self-consistent solution $E_{\rm f} = E - E_0$ are listed in Table 2.3 (the first two rows of this table are relevant; the second two rows are discussed below).

The lower panel of Figure 2.9 shows a visualisation of the magnetic field of the self-consistent solutions. The magnetic field lines of the P and N solutions after ten self-consistency cycles are shown by the blue and red curves respectively. In contrast to the top panel of Figure 2.9, the two sets of field lines are very similar. Small differences are seen for field lines extending high into the computational volume. The agreement between the two sets of field lines confirms that a single self-consistent solution is obtained.

The oscillations of the energies of the initial P and N solutions (see Section 2.4.1) means that the magnetic field used to re-map α_0 at the end of the early self-consistency cycle depends somewhat on the number of Grad-Rubin iterations used to construct the P and N solutions. If a different number of Grad-Rubin iterations is chosen the P and N solutions have different field lines, because of the oscillations seen in Figure 2.8. Hence the mapping of field lines is different and the application of Equation (2.5) gives a different result. Correspondingly the final energy of the self-consistency procedure depends somewhat on the number of Grad-Rubin iterations used. To test this dependence we repeat the calculation with 35 Grad-

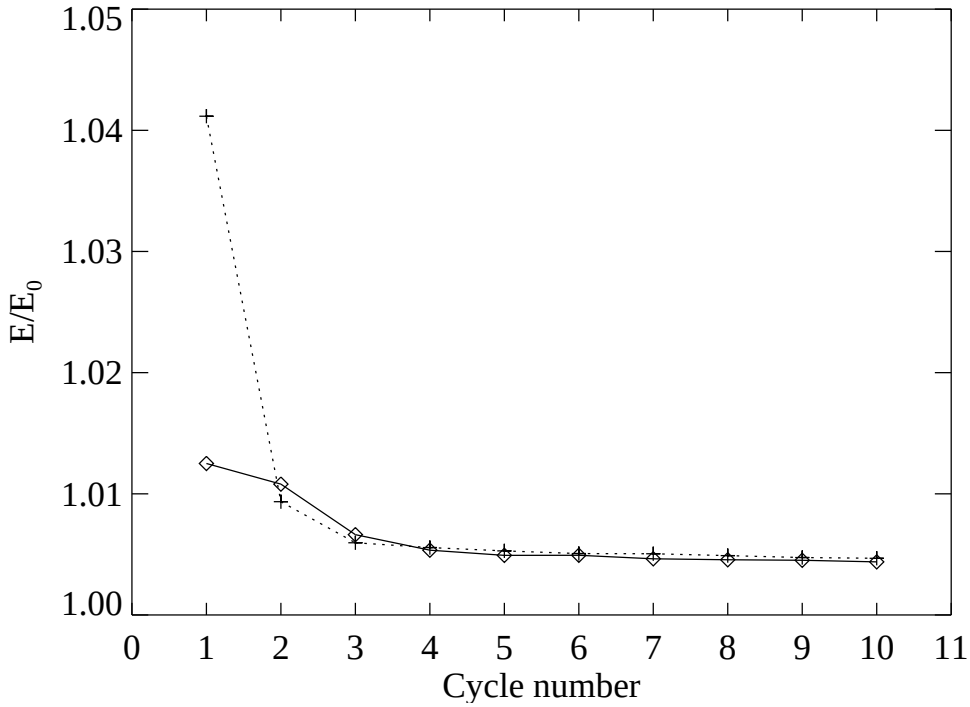

Figure 2.10: Results for the application of the self-consistency procedure to the SOLIS/VSM vector magnetogram data for 24 October. The energies of the P and N solutions (as a fraction of the energy of the potential field) are shown over the ten self-consistency cycles. For each cycle 20 Grad-Rubin iterations are used to construct the P and N solutions. The energy of the P solution is indicated by plus signs and a dashed line, and that of the N solution by diamonds and a solid line.

Table 2.3: Energy estimates for the self-consistent solutions constructed from the SOLIS/VSM magnetogram data for AR 11029 on 24 October.

Grad-Rubin iterations/cycle	Solution	E (10^{31} erg)	E_0 (10^{31} erg)	$E_{\rm f} = E - E_0$ (10^{29} erg)
20	P	9.669	9.62	4.52
	N	9.667	9.62	4.23
35	P	9.666	9.62	4.20
	N	9.667	9.62	4.23

Rubin iterations for the P and N solutions, instead of 20. We choose this value because it corresponds to an iteration at which the difference in energy between the P and N solutions constructed directly from the vector magnetogram data is large (see Figure 2.8). Once again ten self-consistency cycles are applied. The final energy and free energy in this case are also given in Table 2.3 in the third and fourth rows. The variation in the energies for the two self-consistent solutions with different numbers of Grad-Rubin iterations per self-consistency cycle is sufficiently small to justify an order of magnitude (or better) estimate for the free energy of the region based on the results.

The self-consistency procedure modifies α_0 according to the procedure explained in Section 2.2.2. Figure 2.11 shows the vertical current density J_z after ten self-consistency cycles for the P solution (upper panel) and for the N solution (lower panel). The self-consistent values of J_z for the P and N solutions are very similar, confirming that a self-consistent force-free solution is found. This figure should be compared with the lower panel of Figure 2.3, which shows J_z for the original magnetogram data. Both Figures 2.3 and 2.11 cover the same region of the photosphere.

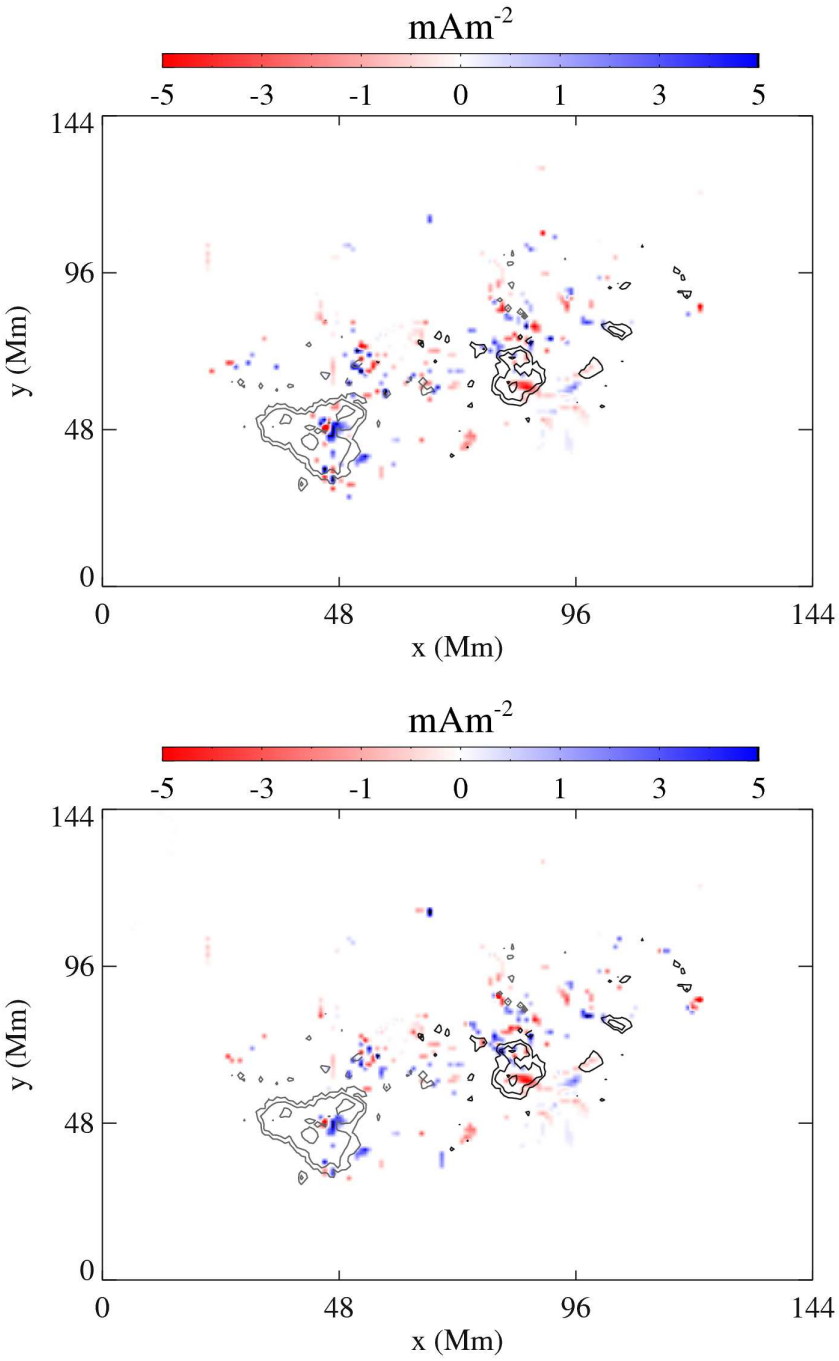

Figure 2.11: Results for the application of the self-consistency procedure to the SOLIS/VSM vector magnetogram data for 24 October. The vertical electric current density J_z over part of the boundary is shown for the P solution (upper panel), and for the N solution (lower panel) after ten self-consistency cycles. The values of J_z are saturated at $\pm 5\,\mathrm{mAm}^{-2}$, and only points where $|\alpha_0/\sigma|$ is three standard deviations above the mean are shown. The contours are the same as Figure 2.3. The distributions of J_z for the P and N solutions after the self-consistency procedure are very similar, indicating a single self-consistent solution is found.

The currents in the lower boundary are significantly reduced as a result of the self-consistency procedure (the maximum currents are $\approx 5\,\mathrm{mAm}^{-2}$ compared with $\approx 15\,\mathrm{mAm}^{-2}$ in the original data). This is in part due to the averaging implied by Equation (2.5). However, it also represents the preservation of smaller but more certain values and the loss of larger but less certain values (based on the phenomenological uncertainty rule $\sigma \sim |B_z|^{-1}$). Specifically the values of α_0 are typically smaller in strong field regions, which have a smaller uncertainty, so these smaller values are better preserved in the application of Equation (2.5) (compared to large values of α_0 in weak field regions). There are substantial areas with $\alpha_0 = 0$ in the final self-consistent boundary data. These patches correspond to open field regions where α is set to zero by the handling of the side and top boundary conditions, as explained in Section 2.2.

2.4.3 Construction of Self-Consistent Solutions for 27 October

The self-consistency procedure is applied to the *Hinode*/SP magnetogram data for 27 October. The initial P and N solutions again oscillate in energy. However, for the *Hinode*/SP data the oscillations are so severe that a meaningful estimate of the energy and free energy cannot be made. The large oscillations are due to large boundary values of α_0. Many of these large values have a large associated uncertainty, and hence may be spurious, but the results of the calculation are influenced by these values. It is necessary to apply the self-consistency procedure which accounts for uncertainties in α_0 and tends to remove values with large uncertainties in a systematic fashion.

The self-consistency procedure is applied to the *Hinode*/SP data for 27 October using two separate runs with a different number of Grad-Rubin iterations per cycle for each run, similar to the procedure in Section 2.4.2 with the SOLIS/VSM data. For the first run we use 20 Grad-Rubin iterations per self-consistency cycle, and for the second run we use 30 Grad-Rubin iterations per self-consistency cycle. We apply ten self-consistency cycles in each case. For both runs the final energies of the P and N solution converge to a single value after ten self-consistency cycles. Figure 2.12 shows the energy of the P solution (plus signs) and N solution (diamonds) in units of the potential field energy at the end of each self-consistency cycle over the ten cycles with 20 Grad-Rubin iterations per cycle. The results using 30 Grad-Rubin iterations are similar to those using 20 iterations per cycle. In both cases the energies of the P and N solution initially differ greatly, but after ten self-consistency cycles the energy difference is reduced to $\approx 1\%$.

The total energy, free energy of the P and N solutions, and the energy of the potential field for the self-consistency calculation are summarised in Table 2.4.

The total and free energy estimates differ for the two runs with different numbers of Grad-Rubin iterations, but the difference is sufficiently small to allow an order of magnitude estimate for the energy. The total energy is large (of order $10^{33}\,\mathrm{erg}$, which is ten times larger than was found for the region on 24 October). The variation in the free energy is correspondingly large, but we can still place an upper bound of $\approx 10^{32}\,\mathrm{erg}$ on the free energy of the active region based on the results in Table 2.4.

Table 2.4: Energy estimates for the self-consistent solutions constructed from the *Hinode*/SP magnetogram data for AR 11029 on 27 October.

Grad-Rubin iterations/cycle	Solution	E (10^{33} erg)	E_0 (10^{33} erg)	$E_\mathrm{f} = E - E_0$ (10^{31} erg)
20	P	1.769	1.707	6.16
	N	1.772	1.707	6.50
30	P	1.787	1.707	7.94
	N	1.791	1.707	8.35

Figure 2.13 shows a visualisation of the magnetic field of the self-consistent P solution (blue curves) and N solution (red curves) for the run using 20 Grad-Rubin iterations per cycle. The two sets of field lines are similar, although some small differences are visible.

The self-consistency procedure modifies α_0 according to the procedure explained in Section 2.2.2. Figure

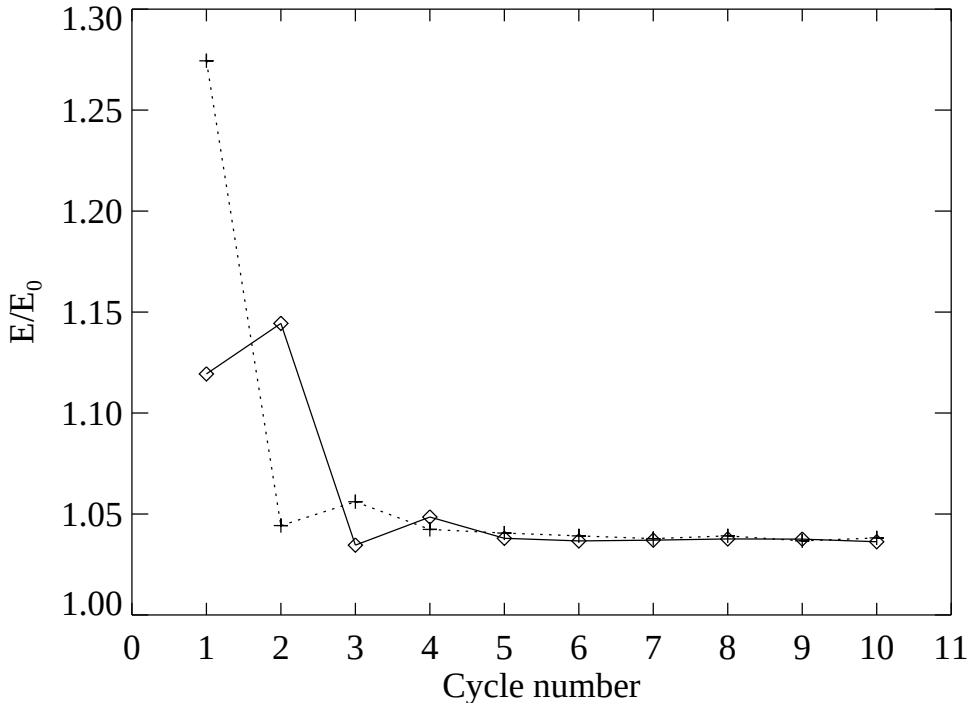

Figure 2.12: Results for the application of the self-consistency procedure to the *Hinode*/SP vector magnetogram data for 27 October. The energies of the P and N solutions (as a fraction of the energy of the potential field) are shown over the ten self-consistency cycles. For each cycle 20 Grad-Rubin iterations are used to construct the P and N solutions. The energy of the P solution is indicated by plus signs and a dashed line, and that of the N solution by diamonds and a solid line.

2.14 shows the vertical current density J_z after ten self-consistency cycles for the P solution (upper panel) and for the N solution (lower panel). The results are shown for the run using 20 Grad-Rubin iterations per cycle, but the results using 30 Grad-Rubin iterations per cycle are similar. The self-consistent values of J_z for the P and N solutions are very similar, confirming that a self-consistent solution is found. The self-consistent values of J_z are significantly reduced by comparison with the values of J_z in the original magnetogram (lower panel of Figure 2.5). This is due to the averaging implicit in the procedure, and the removal by the procedure of large values with large associated uncertainties (see discussion in Section 2.2.2). The final self-consistent boundary data contains regions with $\alpha_0 = 0$ corresponding to open field regions where α has been set to zero by the handling of the side and top boundary conditions (see Section 2.2).

2.5 Summary and Discussion of Results

Estimates of the total energy and free energy of the coronal magnetic field of active region AR 11029 are calculated using two vector magnetograms. The first magnetogram is based on data for 24 October from the SOLIS Vector-SpectroMagnetograph (SOLIS/VSM), and the second is based on data for 27 October obtained from the *Hinode* Solar Optical Telescope SpectroPolarimeter (*Hinode*/SP). The estimates use nonlinear force-free solutions constructed from the vector magnetogram boundary data. The magnetogram data provide two solutions to the nonlinear force-free model (the P and N solutions, denoting the choice of polarity in the boundary conditions used). The model does not have a unique solution because the boundary data are inconsistent with the model. In each case "self-consistent" solutions (Wheatland and Régnier, 2009) are constructed taking into account uncertainties in the boundary data. For the 24 October data the

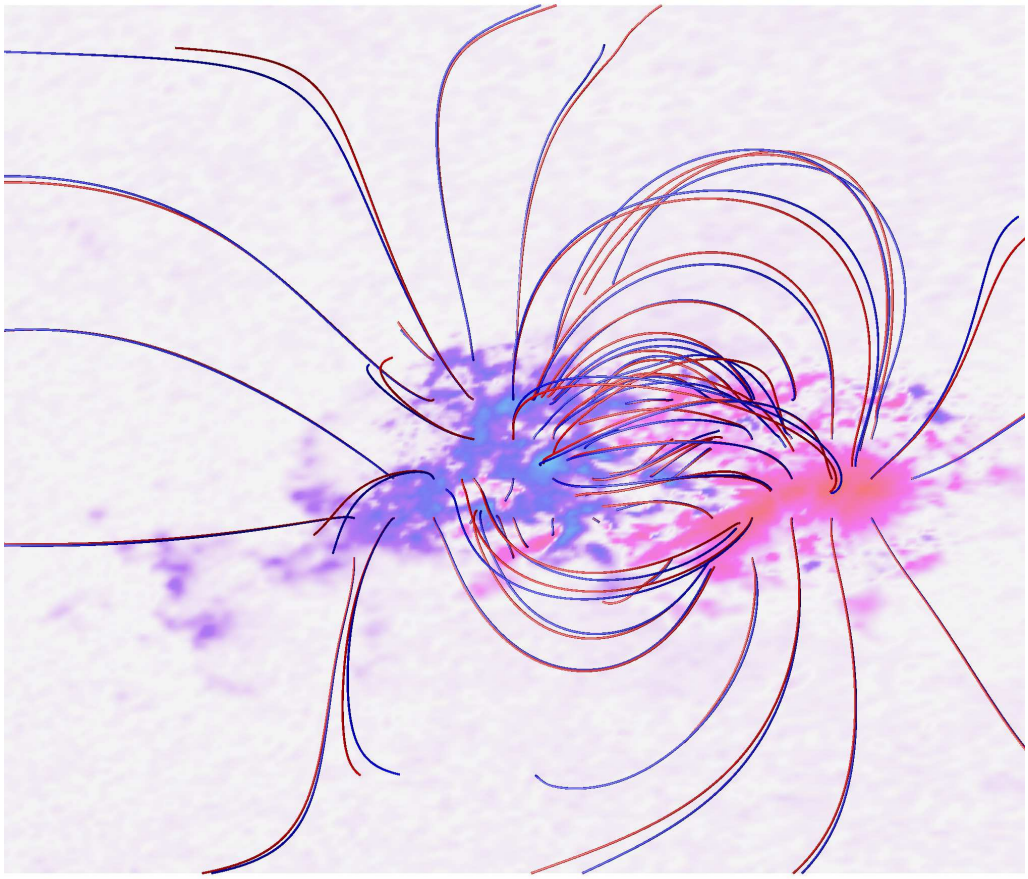

Figure 2.13: Nonlinear force-free models of the coronal magnetic field constructed from the *Hinode*/SP vector magnetogram data for 27 October. The self-consistent P solution (blue field lines) and N solution (red field lines) are shown for the calculation using ten self-consistency cycles with 20 Grad-Rubin iterations per cycle. The region is view looking down on the photosphere which is coloured blue where $B_z > 0$ and red where $B_z < 0$.

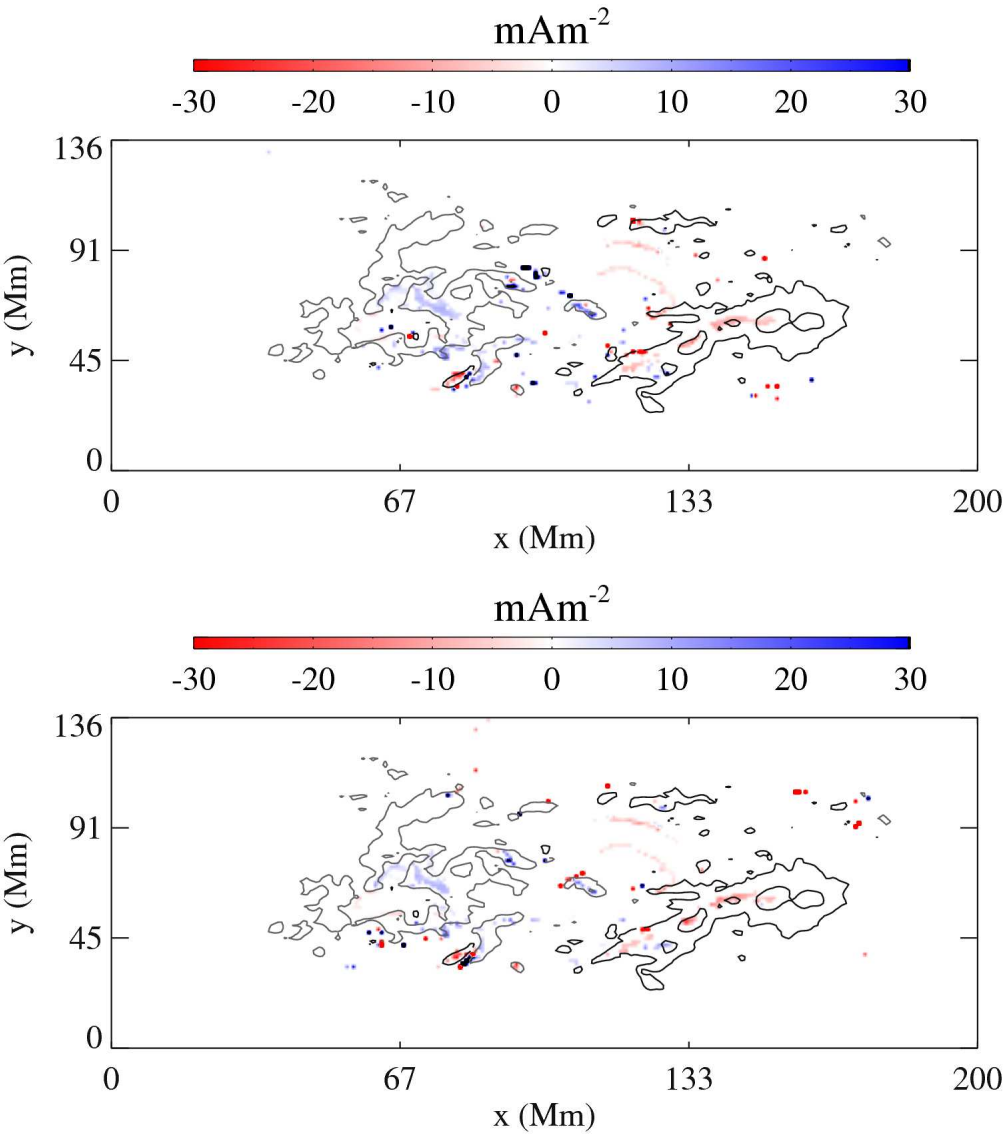

Figure 2.14: Results for the application of the self-consistency procedure to the *Hinode*/SP vector magnetogram data for 27 October. The vertical electric current density J_z over part of the boundary is shown for the P solution (upper panel), and for the N solution (lower panel) after ten self-consistency cycles. The values of J_z are saturated at $\pm 30\,\mathrm{mAm}^{-2}$, and only points where $|\alpha_0/\sigma|$ is three standard deviations above the mean are shown. The contours are the same as Figure 2.5. The distributions of J_z for the P and N solutions after the self-consistency procedure are similar, indicating a single self-consistent solution is found.

uncertainties are estimated phenomenologically, and for the 27 October data the uncertainties are obtained from the inversion process used to construct the magnetogram.

The initial P and N solutions calculated from the vector magnetogram data for 24 October have different energies and different field line structures. These solutions are themselves not uniquely defined because the Grad-Rubin iteration procedure used to construct the solutions does not strictly converge. The energy of the solutions oscillates with successive Grad-Rubin iterations owing to large currents in the boundary data. The amplitude of the oscillations in the total energy is relatively small, but the free energy is a small fraction of the total energy so this represents large amplitude oscillations in the free energy. The oscillations limit the accuracy of the estimation of the free energy, but an order of magnitude estimate is possible. The free energy of AR 11029 on 24 October is estimated from the initial P and N solutions to be $\approx 3 \times 10^{30}\,\mathrm{erg}$.

The self-consistency procedure is applied to the 24 October data. The energy of the P and N solutions agrees closely after ten self-consistency cycles, and visual inspection of the field lines of the P and N solutions confirms that a self-consistent solution is obtained. The final energy of the self-consistent solution depends only weakly on the number of Grad-Rubin iterations per self-consistency cycle allowing a reliable estimate of the free energy. The free energy based on the self-consistent force-free solutions for 24 October is $\approx 4 \times 10^{29}\,\mathrm{erg}$. This value is roughly an order of magnitude smaller than the value obtained from the initial P and N solutions.

For the 27 October *Hinode*/SP data, the initial P and N solutions do not permit a meaningful estimate of the free energy, because of large amplitude oscillations in the energy during the Grad-Rubin procedure. The misbehaviour is attributed to large currents in the boundary data, and many of these values also have large associated uncertainties. The large values prevent convergence of the Grad-Rubin iteration, and hence the result is completely determined by the spurious boundary data. We believe the self-consistency procedure which accounts for these large uncertainties provides a more reliable result. The self-consistency procedure is applied to the *Hinode*/SP data leading to the estimate that the free energy of the region is $\approx 7 \times 10^{31}\,\mathrm{erg}$ on 27 October.

The results presented here illustrate the practical difficulties with force-free modelling (De Rosa *et al.*, 2009). The models constructed directly from the vector magnetogram data do not provide a unique energy estimate so we use the self-consistency procedure. The accuracy of the energy estimates obtained using the self-consistency procedure has not been tested in any independent way, and it is possible to identify aspects of the modelling which may lead to underestimation of the energy. A number of factors tend to reduce the currents in the computational volume and in turn tend to reduce the free energy. Missing boundary data on the top and sides of the computational volume is handled by setting $\alpha = 0$ along field lines which leave the top and sides of the volume. This step removes currents from the volume. The self-consistency procedure also tends to reduce the α_0 values on the lower boundary. This is due to three reasons. First, large values of α_0 which have a large uncertainty are averaged out by the weighted average in the self-consistency procedure. Second, regions with $\alpha_0 \neq 0$ connected by field lines to regions in the flux buffer with $\alpha_0 = 0$ tend to get averaged to $\alpha_0 = 0$ over successive self-consistency cycles because points in the flux buffer are assigned small uncertainties. Third, the boundary data have many small regions of α_0 with opposite sign and averaging between these regions will lead to a net decrease in α_0 over successive self-consistency cycles.

There is also considerable uncertainty associated with the boundary magnetogram data. The field values are based on inversion of spectropolarimetric measurements with finite spatial, depth, and temporal resolution, and the inversions in this case assume a Milne-Eddington atmosphere and the analytic form of the Stokes spectra described by Unno and Rachkovsky (*e.g.* Landi Degl'Innocenti and Landolfi 2004). The active region considered here, NOAA AR 11029, evolved rapidly and was highly dynamic, producing Stokes spectra which were strongly Doppler shifted and multi-lobed over much of the region. The latter indicates that the observed spectra are not consistent with a Milne-Eddington atmosphere, hence the returned field values may not be appropriate estimates of the underlying field. The inversion based uncertainties (explained in Section 2.3.2) for the *Hinode*/SP data reflect this somewhat but are likely underestimates. The inversions for the SOLIS/VSM data can be assumed to harbour the same concerns. There is also uncertainty associated with the resolution of the 180-degree ambiguity (Metcalf *et al.*, 2006; Leka *et al.*, 2009).

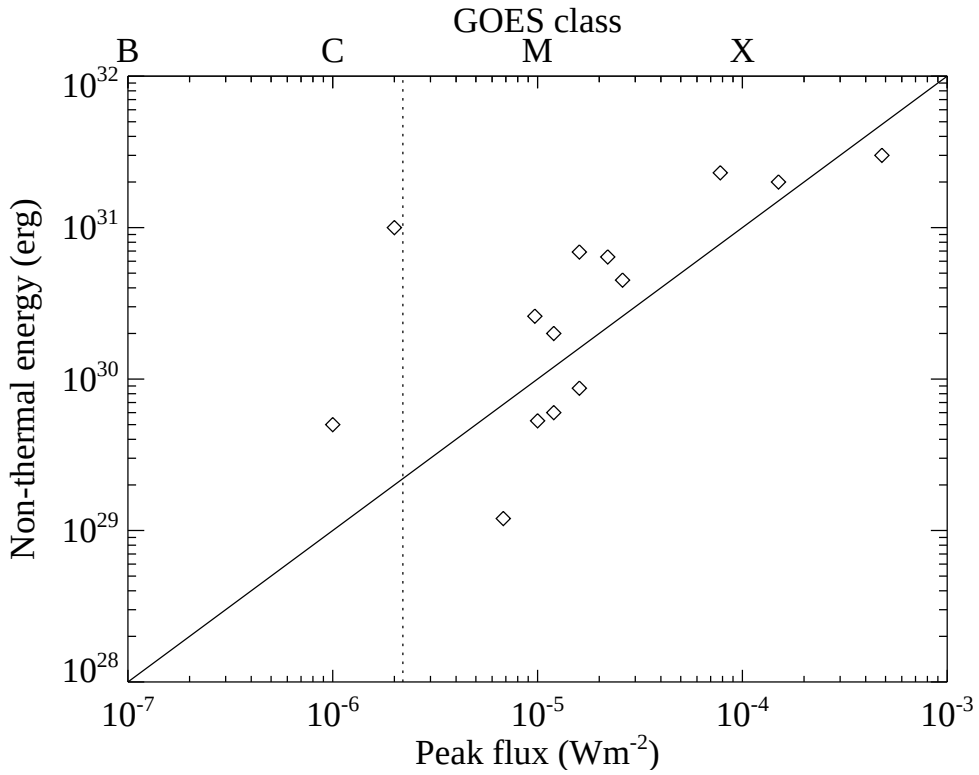

Figure 2.15: The relationship between *RHESSI* energy estimates for the non-thermal energy of a sample of flares from the literature (see Section 2.5) and the *GOES* peak flux of the flares. The plot also indicates the *GOES* classes. The vertical dashed line shows the peak flux of a *GOES* C2.2 class flare (peak flux of $2.2 \times 10^{-6}\,\mathrm{Wm}^{-2}$), the largest soft X-ray flare produced by AR 11029.

Given these caveats, it is nevertheless interesting to compare the energy of the largest flares produced by AR 11029 with the free energy estimates derived for the region, although only a fraction of the free energy is expected to be released in any single flare. To make this comparison we first establish an approximate correlation between *GOES* soft X-ray peak flux and flare energy. One measure of flare energy is the energy of non-thermal electrons, which may be inferred from hard X-ray observations (Lin and Hudson, 1971). We consider a sample from the literature of flare energies estimated from hard X-ray observations, restricting attention (for uniformity) to observations made by the *Reuven Ramaty High-Energy Solar Spectroscopic Imager* (*RHESSI*) (Lin *et al.*, 2002). These flare energies may be compared with the observed *GOES* peak flux of each event to establish an energy-peak flux scaling. Figure 2.15 shows the flare energy estimates made by Saint-Hilaire and Benz (2002), Saint-Hilaire and Benz (2005), Maltagliati, Falchi, and Teriaca (2006), Holman (2005) and Emslie *et al.* (2004) for 14 different *RHESSI* hard X-ray flares, plotted against the observed *GOES* soft X-ray peak flux of each flare. The plot shows that, to within an order of magnitude, a *GOES* B-class event has an energy of $10^{28}\,\mathrm{erg}$, a C-class event has energy an energy of $10^{29}\,\mathrm{erg}$, an M-class event has an energy of $10^{30}\,\mathrm{erg}$, and an X-class event has energy above $10^{31}\,\mathrm{erg}$. This provides a useful rule-of-thumb scaling law for flare energy estimates from *GOES* classification. These energy estimates only take into account the energy of non-thermal electrons producing hard X-rays in the flare. If an event is eruptive then a significant amount of energy can be carried off by the mass ejection (Gopalswamy *et al.*, 2009), and active region AR 11029 produced many small eruptions during its lifetime[7].

On 24 October AR 11029 produced four B class flares, the largest of which is a B4.9 class event with a peak soft X-ray flux of $4.9 \times 10^{-7}\,\mathrm{Wm}^{-2}$. The energy of each of these flares is estimated to be of the order $10^{28}\,\mathrm{erg}$, which is consistent with the upper bound of $4 \times 10^{29}\,\mathrm{erg}$ derived from the self-consistent force-free modelling and the upper bound of $3 \times 10^{30}\,\mathrm{erg}$ obtained from the initial P and N solutions (Tables 2.2 and 2.3).

[7]See the LASCO CME catalog http://cdaw.gsfc.nasa.gov/CME_list/

On 27 October AR 11029 produced 23 soft X-ray flares. The largest flare produced by AR 11029 was a *GOES* class C2.2 which occurred at $00\colon 24\,\mathrm{UT}$ on 28 October. The estimate from the modelling for the free energy is $\approx 7 \times 10^{31}\,\mathrm{erg}$ (Table 2.4), which is comparable to an X-class flare.

Our estimates of the free energy of active region AR 11029 indicate that the region had sufficient energy to produce an M-class or X-class flare on 27 October, but not on 24 October. It is interesting that the estimate for the energy on 27 October is substantially larger than that for 24 October. The photospheric extent of the region grew rapidly during the interval 24 October to 27 October as seen in Figure 2.1 and Wheatland (2010), and it appears that the coronal magnetic field increased in size and energy accordingly. The magnetic flux of the region increased significantly between 24 and 27 October. On 24 October the magnetic flux was $\approx 5 \times 10^{21}\,\mathrm{Mx}$ over the positive polarity and $\approx 4 \times 10^{21}\,\mathrm{Mx}$ over the negative polarity. On 27 October the flux is $\approx 30 \times 10^{21}\,\mathrm{Mx}$ over both polarities, an increase of a factor of 6-7.

2.6 Conclusion

Solar active region AR 11029 was a highly flare productive sunspot region which emerged on the Sun in late October 2009. The region produced 73 soft X-ray flares as recorded in the event list for the *Geostationary Operational Environmental Satellites* (*GOES*) over a period of about a week (24 October to 1 November). Statistical analysis of these flares showed evidence for departure from the standard power-law frequency-size distribution (Wheatland, 2010). Specifically, an absence of large events was indicated. This was conjectured to be due to the small active region having insufficient magnetic energy to power large flares (Wheatland, 2010). The aim of this chapter is to test this hypothesis by estimating the free energy (*i.e.* the energy available for flaring) using nonlinear force-free modelling of the coronal magnetic field of the active region from vector magnetogram data.

Estimates of the magnetic free energy of the coronal magnetic field of AR 11029 are presented using vector magnetogram data taken by the Vector-SpectroMagnetograph at the Solar Observatory's Synoptic Long term Investigations of the Sun facility (SOLIS/VSM), and the Solar Optical Telescope SpectroPolarimeter on the *Hinode* satellite (*Hinode*/SP). Our data set consists of a SOLIS/VSM magnetogram taken on 24 October 2009 and a *Hinode*/SP magnetogram taken on 27 October 2009. Force-free solutions are constructed from the data using the Grad-Rubin code due to Wheatland (2007) and the self-consistency procedure due to Wheatland and Régnier (2009). The procedure address the problem of the inconsistency between the force-free model and the photospheric data (Metcalf *et al.* 1995; De Rosa *et al.* 2009).

For the two vector magnetograms free energy estimates are obtained. For 24 October we estimate a free energy of $\approx\ 4 \times 10^{29}\,\mathrm{erg}$, which is roughly the size of a *GOES* C-class or small *GOES* M-class flare. For 27 October we estimate a free energy $\approx\ 7 \times 10^{31}\,\mathrm{erg}$, which is roughly the size of a *GOES* X-class flare. Although free-energy estimates made using non-linear force-free modelling are subject to significant uncertainty we believe that the order of magnitude of these estimates is correct.

The results in this chapter illustrate the difficulties with applying nonlinear force-free models to solar data. The uncertainty in the free energy estimates is large as a result of the non-convergence of the force-free model. Despite these difficulties, the results in this chapter do not support the hypothesis that there is an observable upper limit on the sizes of flares produced by small active regions due to insufficient free energy in the active region magnetic field. The modelling re-opens the interesting question of why this region did not produce any large flares given that it had sufficient energy to do so.

Chapter 3

A Magneto-Hydrostatic Grad-Rubin Code for Coronal Magnetic Field Extrapolations

Gilchrist, S.A., Wheatland, M.S.: 2013, *Solar Physics* **282**, 283.

Abstract

The coronal magnetic field cannot be directly observed, but in principle it can be reconstructed from the comparatively well observed photospheric magnetic field. A popular approach uses a nonlinear force-free model. Non-magnetic forces at the photosphere are significant meaning the photospheric data are inconsistent with the force-free model, and this causes problems with the modelling (De Rosa *et al.*, *Astrophys. J.* **696**, 1780, 2009). In this chapter we present a numerical implementation of the Grad-Rubin method for reconstructing the coronal magnetic field using a magneto-hydrostatic model. This model includes a pressure force and a non-zero magnetic Lorentz force. We demonstrate our implementation on a simple analytic test case and obtain the speed and numerical error scaling as a function of the grid size.

3.1 Introduction

Force-free extrapolations of the solar coronal magnetic field based on photospheric data contain a basic inconsistency: the magnetic field at the photosphere is not in a force-free state (Gary, 2001; Metcalf *et al.*, 1995). This inconsistency causes problems with the modelling (De Rosa *et al.*, 2009; Schrijver *et al.*, 2008).

The forced nature of the photospheric magnetic field can be demonstrated using photospheric vector magnetogram data. In the Cartesian half-space $z \geq 0$, the components of the net magnetic force in the volume above the $z = 0$ plane are determined by the magnetic field on the plane according to (Molodenskii, 1969)

$$F_x = \int B_x B_z dx dy, \tag{3.1}$$

$$F_y = \int B_y B_z dx dy, \tag{3.2}$$

$$F_z = \int (B_z^2 + B_x^2 - B_y^2) dx dy, \tag{3.3}$$

and

$$F_0 = \int (B_x^2 + B_y^2 + B_z^2) dx dy, \tag{3.4}$$

where B_x, B_y, and B_z are the Cartesian components of the magnetic field in the $z = 0$ plane. A set of necessary conditions for the magnetic field in the volume to be force-free are

$$\frac{F_x}{F_0} = 0, \tag{3.5}$$

$$\frac{F_y}{F_0} = 0, \tag{3.6}$$

and

$$\frac{F_z}{F_0} = 0. \tag{3.7}$$

In application to the Sun, the $z = 0$ plane is a local tangent plane which approximates a small patch of the photosphere, and the components of $\mathbf{B}$ are derived from spectro-polarimetric inversion. Metcalf *et al.* (1995) computed the ratios F_x/F_0, F_y/F_0, and F_z/F_0 based on spectro-polarimetric observations of the magnetic field at several heights in the photosphere/chromosphere above an active region. They found that, for the region studied, the magnetic field became force-free at a height of $\approx 400\mathrm{km}$ above the photosphere.

A low plasma beta is also indicative of a magnetic field in a force-free state. The plasma beta at the photosphere is estimated to be of order unity in active regions (Gary, 2001) implying pressure forces are comparable to magnetic forces at the photosphere.

The application of the nonlinear force-free model to magnetogram data has proved problematic. The numerical solution methods are generally iterative, and when applied to solar data the iterations may fail to converge (De Rosa *et al.*, 2009). The problem is particularly pronounced when large electric currents are present in the data. An example of the non-convergence of the Grad-Rubin method is demonstrated in Chapter 2. For the data for the 24th of October, the non-convergence appeared as an oscillation in the energy of the reconstructed field. The oscillations were small enough that the energy could be estimated with some ambiguity. However for the data for the 27th of October, the Grad-Rubin method did not converge, and no estimate of the magnetic field could be made based on a direct application of the force-free modelling.

Different solution methods are affected by the inconsistency in different ways. For methods using the well-posed formalism (see Section 1.4.3), the force-free parameter α is prescribed over a single polarity of the normal component of $\mathbf{B}$, which results in two possible solutions for each set of data. In practice, these two solutions are qualitatively and quantitatively different due to the forced nature of the boundary data. Figure 2.9 illustrates this problem. The two sets of field lines are the two solutions for the two different prescriptions of α on the boundary. There is significant difference between the two sets of field lines. For methods which over specify the problem the iterative methods can never converge to a force-free state if the boundary data are not consistent with the force-free model. In practice, this leads to numerical solutions with residual forces and nonzero divergence.

A proposed solution to this problem is "preprocessing" of the data (Wiegelmann, Inhester, and Sakurai, 2006; Fuhrmann, Seehafer, and Valori, 2007). With this technique the data are modified to be consistent with Equations (3.5)-(3.7) while maintaining minimal departure from the original data. However, Equations (3.5)-(3.7) are necessary conditions for forces to vanish in the volume, so even if they are satisfied, the data can still be inconsistent with the force-free model (De Rosa *et al.*, 2009) and mixed results have been obtained in the modelling: in some cases the problems were reduced (Schrijver *et al.*, 2008) and in other cases there was no significant improvement (De Rosa *et al.*, 2009).

Another approach is to develop static models of the coronal magnetic field which incorporate non-magnetic forces, *i.e.* magneto-hydrostatic models, which incorporate gravity and gas pressure forces. In this chapter we consider a model including only a pressure force. This model requires the prescription of pressure as a boundary condition. Presently, the photospheric pressure distribution is difficult to obtain observationally

compared to the magnetic field. This is a limitation of magneto-hydrostatic (and magneto-hydrodynamic) models in application to solar data.

A number of methods for solving the magneto-hydrostatic equations have been developed for modelling the coronal magnetic field. The optimisation procedure developed for the nonlinear force-free model has been extended to magneto-hydrostatic models in Cartesian geometry (Wiegelmann and Inhester, 2003; Wiegelmann and Neukirch, 2006), and spherical geometry (Wiegelmann *et al.*, 2007). Amari, Boulbe, and Boulmezaoud (2009) presented a finite element implementation of the Grad-Rubin method (Grad and Rubin, 1958). In addition semi-analytic approaches have been developed but these provide only restricted, and not general, solutions (*e.g.* Rudenko 2001).

In this chapter we present a numerical code to solve a general magneto-hydrostatic model of the coronal magnetic field of an active region. Our code is an implementation of the Grad-Rubin method (Grad and Rubin, 1958) to the magneto-hydrostatic equations in the half-space $z \geq 0$. The Grad-Rubin method has previously been used to solve the nonlinear force-free equations in the half-space for coronal reconstructions (*e.g.* Wheatland 2006; Amari, Boulmezaoud, and Mikic 1999), and to solve the magneto-hydrostatic equations in toroidal geometry (Reiman and Greenside, 1986) and in arbitrary geometry (Amari, Boulbe, and Boulmezaoud, 2009). The Grad-Rubin method has the advantage of, in principle, solving the magneto-hydrostatic equations to the limit imposed by numerical accuracy (*e.g.* truncation error due to the finite grid size), assuming the Grad-Rubin iteration procedure converges. We apply the code to a simple analytic test case as a demonstration, and to investigate the speed and numerical error scaling of the implementation. The resulting code and method does not yet provide a practical tool for coronal field modelling from solar data, because of the neglect of the gravity force, but it is a significant step in this direction.

This chapter is structured as follows. Section 3.2 presents the magneto-hydrostatic equations, and the boundary value problem to be solved. Section 3.3 is a brief summary of the Grad-Rubin method, and describes our specific implementation of the method in code. Section 3.4 presents the analytic test case used. Section 3.5 presents the results, and Section 3.6 contains discussion of the results and the conclusion.

3.2 Magneto-Hydrostatic Equations and Boundary Value Problem

3.2.1 The Model

The magneto-hydrostatic equations with the gravity force neglected are (Priest, 1984):

$$\nabla \times \mathbf{B} = \mu_0 \mathbf{J}, \tag{3.8}$$

$$\nabla \cdot \mathbf{B} = 0, \tag{3.9}$$

and

$$\mathbf{J} \times \mathbf{B} - \nabla p = 0. \tag{3.10}$$

Here p is the gas pressure, $\mathbf{J}$ is the electric current density, and $\mathbf{B}$ is the magnetic field vector.

3.2.2 The Boundary Value Problem

For a small active region the curvature of the photosphere is small, so we solve Equations (3.8)-(3.10) in the half-space $z \geq 0$, with the $z = 0$ plane representing the photosphere. The appropriate boundary conditions prescribed on the $z = 0$ plane are B_z, together with p and J_z prescribed over a single polarity of the magnetic field, *i.e.* p and J_z are prescribed only at points with $B_z > 0$ or at points where $B_z < 0$ (Grad and

Rubin, 1958). We denote the boundary values of the magnetic field, pressure and current density by $B_{\rm obs}$, $p_{\rm obs}$ and $J_{\rm obs}$ respectively. These boundary conditions are believed to be the correct physical boundary conditions for the magnetostatic model.

Equations (3.8)-(3.10) are solved numerically in the finite volume

$$\Omega_b = \{(x, y, z) | \, 0 \leq x \leq L_x, 0 \leq y \leq L_y, 0 \leq z \leq L_z\}. \tag{3.11}$$

In addition to the $z = 0$ plane, Ω_b has five additional plane boundaries on which boundary conditions are required. Magnetogram data only provide boundary conditions on the $z = 0$ plane and reasonable assumptions must be made for the remaining five. This problem is faced by all reconstruction codes regardless of the particular model or method used, and models including more physics typically require more boundary conditions at each boundary.

We choose boundary conditions on the magnetic field such that all field lines are connected to the lower boundary at two points (*i.e.* there are no open field lines). The need for this is discussed in Section 3.3.2. We achieve this in practice by imposing either (i) closed boundary conditions on the top and side boundaries

$$\mathbf{B} \cdot \hat{\mathbf{n}} = 0, \tag{3.12}$$

where $\hat{\mathbf{n}}$ denotes the unit normal vector to each boundary, or (ii) a closed top boundary condition

$$\mathbf{B} \cdot \hat{\mathbf{z}} = 0, \tag{3.13}$$

together with periodic boundary conditions on the side boundaries. For the periodic case any field line which leaves the computational volume by a side boundary re-enters on the opposite side, and therefore eventually connects to the lower boundary. These boundary conditions specify that magnetic flux only enters and leaves through the lower boundary, which requires that the lower boundary is flux balanced.

3.3 Numerical Implementation of the Grad-Rubin Method

In this section we outline our implementation of the Grad-Rubin method in code. The approach is similar to that for the force-free code described in Wheatland (2007).

3.3.1 The Grad-Rubin Method

The Grad-Rubin method (also called the current-field iteration method) is an iterative scheme for solving the magneto-hydrostatic equations (Grad and Rubin, 1958). In this method the nonlinear equations (Equations (3.8)-(3.10)) are replaced with a set of linear equations which are solved at each iteration. The method was originally formulated for solving the magneto-hydrostatic equations, but has been applied most often to the force-free equations.

Here we briefly outline a single Grad-Rubin iteration (a more detailed description is given by Grad and Rubin (1958)). We denote a quantity after k Grad-Rubin iterations using a superscript, so for example $\mathbf{B}^{[k]}$ denotes the magnetic field in our computational volume after k iterations starting from an initial magnetic field $\mathbf{B}^{[0]}$. In practice the iteration is initiated with a potential field in the volume calculated from $B_{\rm obs}$, which we denote as $\mathbf{B}^{[0]} = \mathbf{B}_0$. In the following we assume $\mathbf{B}^{[k]}$ is known from a previous iteration, or is the initial potential field. A single iteration consists of the following steps.

1. Calculate a new pressure $p^{[k+1]}$ in the volume by solving

$$\mathbf{B}^{[k]} \cdot \nabla p^{[k+1]} = 0, \tag{3.14}$$

with boundary conditions

$$p^{[k+1]}|_{z=0} = p_{\rm obs} \tag{3.15}$$

prescribed over one polarity of $B_{\rm obs}$.

2. Calculate the component of the current density perpendicular to the magnetic field in the volume using

$$\mathbf{J}_{\perp}^{[k+1]} = \nabla p^{[k+1]} \times \mathbf{B}^{[k]}/|\mathbf{B}^{[k]}|^2. \tag{3.16}$$

3. Calculate the component $\mathbf{J}_{\parallel}^{[k+1]}$ of the current density parallel to the magnetic field in the volume. The parallel component can be written as

$$\mathbf{J}_{\parallel}^{[k+1]} = \sigma^{[k+1]}\mathbf{B}^{[k]}/\mu_0, \tag{3.17}$$

where $\sigma^{[k+1]}$ is a scalar function of position. The parameter $\sigma^{[k+1]}$ is calculated in the volume by solving (Grad and Rubin, 1958)

$$\nabla\sigma^{[k+1]} \cdot \mathbf{B}^{[k]} = -\mu_0 \nabla \cdot \mathbf{J}_{\perp}^{[k+1]}, \tag{3.18}$$

with boundary conditions

$$\sigma|_{z=0} = \sigma_{\rm obs}^{[k+1]} \tag{3.19}$$

where

$$\sigma_{\rm obs}^{[k+1]} = \left.\frac{\mu_0(\mathbf{J}_{\perp}^{[k+1]} \cdot \hat{\mathbf{z}} - J_{\rm obs})}{B_{\rm obs}}\right|_{z=0}. \tag{3.20}$$

The boundary conditions $\sigma_{\rm obs}^{[k+1]}$ are prescribed over a single polarity of $B_{\rm obs}$ and are calculated using Equation (3.20) at each iteration. The form of Equation (3.20) is such that $\mathbf{J}^{[k+1]} \cdot \hat{\boldsymbol{z}} = J_{\rm obs}$ on the lower boundary (over the polarity of $B_{\rm obs}$ chosen for the boundary conditions).

Equations (3.16)-(3.17) define the total current density in the volume:

$$\mathbf{J}^{[k+1]} = \mathbf{J}_{\perp}^{[k+1]} + \sigma^{[k+1]}\mathbf{B}^{[k]}/\mu_0. \tag{3.21}$$

4. Calculate the new magnetic field in the volume by solving Ampere's law

$$\nabla \times \mathbf{B}^{[k+1]} = \mu_0 \mathbf{J}^{[k+1]}, \tag{3.22}$$

where the boundary conditions on $\mathbf{B}^{[k+1]}$ are those in Section 3.2.

3.3.2 Overview of the Code

The code solves the magneto-hydrostatic equations in the finite Cartesian domain $\Omega_{\rm b}$ using the Grad-Rubin method. The numerical grid is uniformly spaced with N grid points along each dimension, so there are N^3 grid points in total, and in the following we write $L = L_x = L_y = L_z$ for simplicity. The grid spacing is $L/(N-1)$, and the coordinates of the grid points are $(x_i, y_j, z_k) = (i, j, k)L/(N-1)$, where $0 \leq i, j, k \leq N-1$.

In the following we describe the implementation of the Grad-Rubin steps identified in Section 3.3.1 in detail, identifying some of the numerical methods used. The code is an implementation in FORTRAN90 using double precision floating point numbers (Press *et al.*, 2007). The code is parallelised for shared memory multiprocessors using OpenMP (Chandra *et al.*, 1990).

Step 1: Update of Pressure in the Volume

Equation (3.14) is solved by a field line tracing (or characteristic) method. The same method is used in some existing force-free Grad-Rubin method implementations for solving $\mathbf{B} \cdot \nabla\alpha = 0$ (*e.g.* Amari, Boulmezaoud, and Mikic 1999; Wheatland 2006, 2007). Equation (3.14) has also been solved using a finite element method (Amari, Boulmezaoud, and Aly, 2006). In the force-free case the tracing is used to update α in the volume, and here it is used to update the pressure.

The procedure is as follows. For each grid point (x_i, y_j, z_k) the field line threading (x_i, y_j, z_k) is traced to the point (x_0, y_0) where it crosses the lower boundary with the appropriate polarity for the boundary conditions. The pressure at the grid point is then assigned to be equal to the boundary value:

$$p(x_i, y_j, z_k) = p_{\rm obs}(x_0, y_0). \tag{3.23}$$

This procedure solves Equation (3.14) because the pressure is constant along a magnetic field line. The tracing is performed in either the forward or backward direction along the field line, with the direction chosen such that the point (x_0, y_0) has the appropriate polarity for $B_{\rm obs}$. Fourth order Runge-Kutta is used for the numerical tracing (Press *et al.*, 2007). Because the path of the field line is not confined to grid points, trilinear interpolation is used to estimate $\mathbf{B}$ between grid points (Press *et al.*, 2007). Similarly, bilinear interpolation is used to compute $p_{\rm obs}$ at the boundary point (x_0, y_0), which also may not coincide with a grid point.

Open field lines (see Section 3.2.2) would present a problem for this method. Since $p_{\rm obs}$ is only prescribed over a single polarity, it would be impossible to assign pressure to points threaded by field lines which connect to the lower boundary at only one polarity, opposite to that for which $p_{\rm obs}$ is prescribed. We avoid this problem by preventing open field lines through the choice of boundary conditions on $\mathbf{B}$ explained in Section 3.2.2. This eliminates the problem but introduces artificial boundary conditions on the top and side boundaries. However, the region of interest can be isolated from the effects of the boundaries by using a large domain.

Steps 2 and 3: Update of the Current Density in the Volume

Given the updated values $p^{[k+1]}$ for the pressure in the volume, Equation (3.16) may be directly evaluated at every gridpoint to give the perpendicular current $\mathbf{J}_\perp$ in the volume. The derivatives in the gradient on the right hand side are evaluated numerically using a centred difference approximation (Press *et al.*, 2007).

A particular problem is encountered with the evaluation of the perpendicular current $\mathbf{J}_\perp$ in the volume at each iteration (step 2 in the enumeration of the procedure in Section 3.3.1), for the test cases considered here. The perpendicular current is calculated using Equation (3.16):

$$\mathbf{J}_\perp^{[k+1]} = \nabla p^{[k+1]} \times \mathbf{B}^{[k]} / |\mathbf{B}^{[k]}|^2. \tag{3.24}$$

For the analytic solutions we use in Section 3.5 there are locations in the volume where $\mathbf{B} = 0$ and $\mathbf{J}_\perp$ is finite. The perpendicular current is not correctly evaluated numerically at these points. To prevent this we choose grid sizes for our problems such that the points with $\mathbf{B} = 0$ fall between grid points.

The value of $\sigma^{[k+1]}$ at each gridpoint is then obtained by solving Equation (3.18). This equation may be integrated along a field line to give the formal solution

$$\sigma^{[k+1]}(x_i, y_j, z_k) = \sigma_{\rm obs}(x_0, y_0) - \gamma \int_0^{s_0} \nabla \cdot \mathbf{J}_\perp^{[k+1]}(\mathbf{x}(s)) / |\mathbf{B}^{[k]}(\mathbf{x}(s))| ds, \tag{3.25}$$

where

$$\gamma = \begin{cases} +1 \text{ if } J_{\rm obs} \text{ is prescribed over } B_z > 0 \\ -1 \text{ if } J_{\rm obs} \text{ is prescribed over } B_z < 0, \end{cases} \tag{3.26}$$

where $\mathbf{x}(s)$ is the path of the field line (the parameter s is the arc length along the field line), and where $\mathbf{x}(s_0)$ is the point $(x_0, y_0, 0)$ at which the boundary conditions on $\sigma^{[k+1]}$ are imposed. Trilinear interpolation is

used to assign values in the argument of the integral along a field line, and the integral is evaluated using the trapezoidal rule (Press *et al.*, 2007).

The field line tracing needed for steps one and two (updating pressure and σ) is the computationally slow part of this implementation of the Grad-Rubin method. The number of operations for the field line tracing scales as N^4 for a grid with N^3 points (Wheatland, 2006). In the following we will write "$\sim N^4$" to denote such a scaling. The code parallelises the process using OpenMP, with the workload divided such that different code threads trace different field lines.

It is important to understand the accuracy of the numerical solutions for $p^{[k]}$ and $\sigma^{[k]}$. For the field line tracing solution we can infer an approximate scaling for the numerical error as follows. Trilinear interpolation has truncation error $\sim 1/N^2$ (Zikanov, 2010), and on average a field line requires $\sim N$ Runge-Kutta steps to reach the lower boundary. Therefore the total numerical error introduced by tracing a field line to the lower boundary has scaling $\sim N \times 1/N^2 = 1/N$). We expect this error to be the dominant error in the calculation, and so the error scaling for the whole computation is $\sim 1/N$. This error scaling has been confirmed for the force-free case (Wheatland, 2006).

Step 4: Update of the Magnetic Field in the Volume

The magnetic field may be expressed as $\mathbf{B}^{[k]} = \mathbf{B}_0 + \mathbf{B}_c^{[k]}$, where $\mathbf{B}_0$ is the potential field satisfying $\nabla \times \mathbf{B}_0 = 0$ together with the boundary condition

$$\mathbf{B}_0 \cdot \hat{\mathbf{z}}|_{z=0} = B_{\rm obs}, \tag{3.27}$$

and where $\mathbf{B}_c^{[k]}$ is a current carrying field satisfying $\nabla \times \mathbf{B}_c^{[k]} = \mu_0 \mathbf{J}^{[k]}$ together with the homogeneous boundary condition

$$\mathbf{B}_c^{[k]} \cdot \hat{\mathbf{z}}|_{z=0} = 0. \tag{3.28}$$

The fields $\mathbf{B}_c^{[k]}$ and $\mathbf{B}_0$ have the same boundary conditions on the top and side boundaries (either closed boundary conditions on all other boundaries, or closed top boundary conditions and periodic side boundary conditions, as discussed in Section 3.2.2).

The potential component has a well-known Fourier solutions in Cartesian geometry (Morse and Feshbach, 1953), and we use a two-dimensional Fourier series solution with the expansion performed in the x and y directions. For periodic boundary conditions the components of our potential field are[1]

$$B_{0x}(x,y,z) = \sum_{m=0}^{\infty}\sum_{n=0}^{\infty} c_{mn} i k_m \cosh(k[z-L]) \mathrm{e}^{i(xk_m + yk_n)}, \tag{3.29}$$

$$B_{0y}(x,y,z) = \sum_{m=0}^{\infty}\sum_{n=0}^{\infty} c_{mn} i k_n \cosh(k[z-L]) \mathrm{e}^{i(xk_m + yk_n)}, \tag{3.30}$$

and

$$B_{0z}(x,y,z) = \sum_{m=0}^{\infty}\sum_{n=0}^{\infty} c_{mn} k \sinh(k[z-L]) \mathrm{e}^{i(xk_m + yk_n)}. \tag{3.31}$$

where $k_m = 2\pi m/L$, $k_n = 2\pi n/L$ and $k^2 = k_m^2 + k_n^2$. The Fourier series coefficients are derived from the boundary conditions:

$$c_{mn} = -\frac{1}{L^2}\int_0^L \int_0^L dxdy B_{\rm obs}(x,y) \mathrm{e}^{-i(xk_m + yk_n)} / \sinh(kL). \tag{3.32}$$

[1] We note that this solution is a special case of the linear force-free solution due to Barbosa (1978), and is obtained by setting $\alpha = 0$ in that solution.

As explained in Section 3.2.2, we also use a solution with closed boundaries, and the expression for the components of this field are similar (see Appendix A). Equations (3.29)-(3.30) can be computed using Fast Fourier transforms, in which case $\sim N^3 \log(N)$ operations are required to evaluate the potential field for a grid of N^3 grid points (Press *et al.*, 2007). This makes step 4 relatively fast, computationally.

For the non-potential component $\mathbf{B}_c$ we use a three-dimensional Fourier series solution to the vector Poisson equation, working with a vector potential $\mathbf{A}_c$ such that $\mathbf{B}_c = \nabla \times \mathbf{A}_c$ (Morse and Feshbach, 1953). The components of the field are

$$B_{cx}(x,y,z) = \sum_{m=0}^{\infty}\sum_{n=0}^{\infty}\sum_{p=0}^{\infty}\left[k_n i a^{(3)}_{mnp} - k_p a^{(2)}_{mnp}\right]\cos(k_p z)\mathrm{e}^{i(k_m x + k_n y)}/k^2, \tag{3.33}$$

$$B_{cy}(x,y,z) = \sum_{m=0}^{\infty}\sum_{n=0}^{\infty}\sum_{p=0}^{\infty}\left[k_p a^{(1)}_{mnp} - k_m i a^{(3)}_{mnp}\right]\cos(k_p z)\mathrm{e}^{i(k_m x + k_n y)}/k^2, \tag{3.34}$$

$$\tag{3.35}$$

and

$$B_{cz}(x,y,z) = \sum_{m=0}^{\infty}\sum_{n=0}^{\infty}\sum_{p=0}^{\infty} i\left[k_m a^{(2)}_{mnp} - k_n a^{(1)}_{mnp}\right]\sin(k_p z)\mathrm{e}^{i(k_m x + k_n y)}/k^2. \tag{3.36}$$

Here $k_m = 2\pi m/L$, $k_n = 2\pi n/L$, and $k_p = \pi p/L$. The coefficients $a^{(i)}_{mnp}$, with $i = 1, 2, 3$ are given by:

$$a^{(1)}_{mnp} = \frac{2\mu_0}{L^3}\int_0^L\int_0^L\int_0^L J_x(x,y,z)\mathrm{e}^{-i(k_m x + k_n y)}\sin(k_p z)dxdydz, \tag{3.37}$$

$$a^{(2)}_{mnp} = \frac{2\mu_0}{L^3}\int_0^L\int_0^L\int_0^L J_y(x,y,z)\mathrm{e}^{-i(k_m x + k_n y)}\sin(k_p z)dxdydz, \tag{3.38}$$

and

$$a^{(3)}_{mnp} = \frac{2\mu_0}{L^3}\int_0^L\int_0^L\int_0^L J_z(x,y,z)\mathrm{e}^{-i(k_m x + k_n y)}\cos(k_p z)dxdydz. \tag{3.39}$$

The coefficients given by Equations (3.37)-(3.39), and the solution given by Equations (3.33)-(3.36), are computed in $\sim N^3 \log(N)$ operations using a combination of fast Fourier, fast sine, and fast cosine transforms (Poularikas, 1996; Press *et al.*, 2007). The corresponding solution for $\mathbf{B}_c$ with closed side boundaries is given in Appendix B, which also provides more detail on how these solutions are derived.

3.4 Analytic Test Case

To test the code we use a simple analytic solution to the magneto-hydrostatic equations (Wiegelmann, 1998; Wiegelmann and Inhester, 2003) which is a generalisation of a force-free field in Sturrock (1994), and which may be derived using the generating function method. The solution describes a sheared magnetic arcade with translational symmetry in the y direction and periodicity in the x direction.

For the problem at hand we modify the sheared arcade solution by imposing a closed top boundary condition (to match the boundary condition required by our Grad-Rubin method):

$$B_z(x,y,L) = 0. \tag{3.40}$$

The components of the resulting magnetostatic field are

$$B_x(x,z) = \psi_0 l \sin(kx)\cosh[l(L-z)], \tag{3.41}$$

$$B_y(x,z) = \psi_0 \lambda\sqrt{1-a_0}\sin(kx)\sinh[l(L-z)], \tag{3.42}$$

and

$$B_z(x,z) = \psi_0 k \cos(kx) \sinh[l(L-z)], \tag{3.43}$$

and the pressure is given by

$$p(x,z) = \psi_0^2 \left(\frac{a_0\lambda}{2\mu_0}\right) \sin^2(kx) \sinh^2[l(z-L)], \tag{3.44}$$

where k, λ, ψ_0 and a_0 are free parameters subject to $0 \leq a_0 \leq 1$ and $l = \sqrt{k^2 - \lambda^2}$.

The parameter λ determines the currents in the volume, with $\lambda = 0$ giving a potential field. The parameter a_0 sets the pressure in the volume, and the special case $a_0 = 0$ is a linear force-free field with force-free parameter $\alpha = \lambda$. The parameter a_0 may be used to enforce closed side boundary conditions in y with the choice $a_0 = 1$. The parameter k determines the period of the solution in the x direction, and the constant ψ_0, which determines the magnitude of the field, is chosen to be

$$\psi_0 = \frac{1}{\sinh(lL)k}, \tag{3.45}$$

to specify $\max(|B_{\rm obs}|) = 1$ on the lower boundary.

The boundary conditions in the $z = 0$ plane with the choice of ψ_0 given by Equation (3.45) are

$$B_{\rm obs} = \cos(kx), \tag{3.46}$$

$$p_{\rm obs} = \frac{a_0\lambda}{2\mu_0 k^2} \sin^2(kx), \tag{3.47}$$

and

$$J_{\rm obs} = \mu_0\lambda\sqrt{1-a_0}\cos(kx). \tag{3.48}$$

A schematic diagram of the field lines of the solution is shown in Figure 3.1, for the choices $k = 2\pi/L$, $a_0 = 0.5$, and $\lambda = \pi/(2L)$. The view in the left panel of the Figure is along the y axis. This perspective shows the arcade-like field line structure. The right panel of Figure 3.1 shows a top-down view of the particular field lines shown as dashed curves in the left panel. The top of these field lines is at $z = 3L/4$. This perspective shows that the arcade is sheared. For the given solution the shear angle is $\approx 10^\circ$ for the field lines with the height shown.

3.5 Results

In this section we apply the code to the test case in Section 3.4 for two different choices of parameters. The first choice is for a calculation with periodic side boundary conditions, and the second is for a calculation with closed side boundary conditions. For both cases the tests are performed several times on grids of varying size. The convergence of the Grad-Rubin iteration is demonstrated, and the speed of the code as a function of problem size (introduced in Section 3.3.2) is confirmed. We also examine the accuracy of the numerical solution by comparison with the analytic solution, and investigate the accuracy as a function of grid size, for comparison with the estimate of the scaling of the accuracy given in Section 3.3.2.

3.5.1 Test Case with Periodic Side Boundaries

For the first test we use the parameters $k = 2\pi(1 - 1/N)/L$, $\lambda = \pi/(2L)$ and $a_0 = 0.5$. The parameter k is chosen to vary with N so that the periodicity of the solution matches the periodicity of the discrete

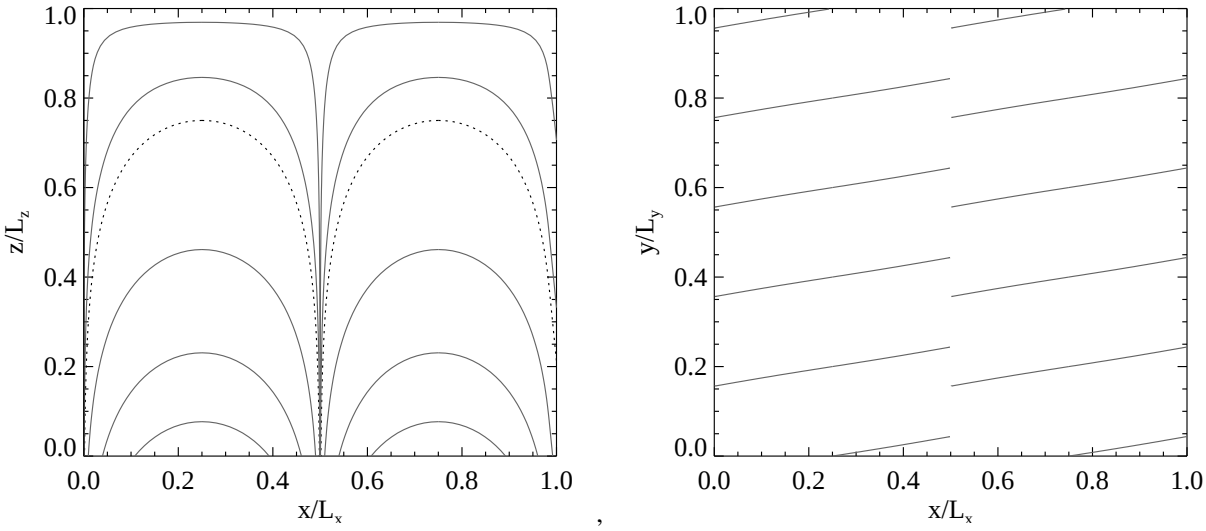

Figure 3.1: Field lines for the analytic magnetostatic field test case (see Section 3.4) with parameters $k = 2\pi/L$, $a_0 = 0.5$, and $\lambda = \pi/(2L)$. In the left panel the point of view is along the y axis. The right panel shows a top-down view of the field lines indicated by the dashed curves in the left panel. These field lines are sheared with respect to the x axis, at an angle of $\approx 10°$.

Fourier transform (Press *et al.*, 2007). A side effect of this is that the test case differs between grid sizes. In particular the boundary conditions, which depend on k through Equations (3.46)-(3.48), are different. However, for large N the difference is small. We apply the code to the test case with three different grid sizes ($N = 65, 101, 151$), and in each case we perform 30 Grad-Rubin iterations starting from a potential field.

The convergence of the Grad-Rubin iteration is measured by the absolute change in the field at each iteration, *i.e.*

$$\Delta B_{\text{avg}} = \langle |\mathbf{B}^{(k)} - \mathbf{B}^{(k-1)}| \rangle \tag{3.49}$$

where $\langle\rangle$ denotes the average over all points in the computational volume. The left panel of Figure 3.2 shows ΔB_{avg} over 30 Grad-Rubin iterations for the three different grid sizes. The squares show the case with $N = 65$, the diamonds show the case with $N = 101$, and the plus signs show the case with $N = 151$. In all three cases the Grad-Rubin iteration converges: ΔB_{avg} decreases exponentially for ≈ 15 iterations before becoming approximately constant. The rate of convergence does not appear to depend strongly on grid size.

The numerical solution after 30 iterations is compared to the analytic solution. This is done qualitatively by comparing the field lines of the analytic solution, the initial potential field, and the numerical solution. The left panel of Figure 3.3 shows the field lines of the analytic solution (light field lines), and the field lines of the potential field (dark field lines) viewed looking down on the computational domain. There is a significant difference between the two sets of field lines. The right panel of Figure 3.3 shows the field lines of the analytic solution (light field lines), and the field lines of the numerical solution after 30 Grad-Rubin iterations (dark field lines) from the same viewpoint. The two sets of field lines closely coincide, confirming that the Grad-Rubin iteration has converged to the analytic solution.

In addition to this qualitative comparison, we compare the analytic and numerical solutions quantitatively. Several metrics have been developed for this purpose in the context of nonlinear force-free modelling (Schrijver *et al.*, 2006). The various metrics show similar results, so for brevity we present only the mean vector error

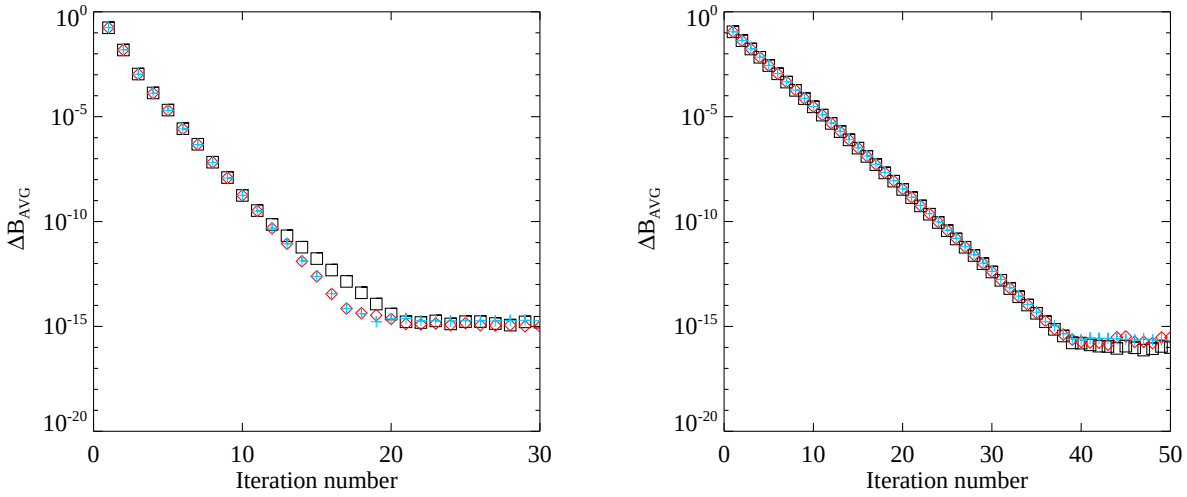

Figure 3.2: The mean absolute change in the field $\Delta B_{\rm avg}$ as a function of iteration number for the application of the Grad-Rubin method to the test cases. The left panel shows $\Delta B_{\rm avg}$ for the three tests with periodic side boundary conditions, and the right panel shows $\Delta B_{\rm avg}$ for the three tests with closed boundary conditions. The different symbols represent $\Delta B_{\rm avg}$ for different grid sizes N. In both panels the $N = 65$ case is shown with squares, the $N = 101$ case is shown with diamonds, and the $N = 151$ case is shown with plus signs, and the scale on the y axis is logarithmic.

$$E_{\rm m} = \left\langle \frac{|\mathbf{B} - \mathbf{b}|}{|\mathbf{B}|} \right\rangle, \tag{3.50}$$

and the metric

$$E_{\rm CS} = 1 - \left\langle \frac{\mathbf{B} \cdot \mathbf{b}}{|\mathbf{B}||\mathbf{b}|} \right\rangle, \tag{3.51}$$

which is based on the Cauchy-Schwartz inequality[2]. In both these definitions the analytic solution is $\mathbf{B}$, the numerical solution is $\mathbf{b}$, and the average is over all grid points in the domain. For two exactly matching fields $E_{\rm m} = 0$ and $E_{\rm CS} = 0$. The mean vector error is a measure of the difference between the magnitude and direction of $\mathbf{B}$ and $\mathbf{b}$ at each grid point, while $E_{\rm CS}$ is only sensitive to the differences in the direction of the fields.

We also compute

$$E_{\rm div} = \langle |\nabla \cdot \mathbf{b}| \rangle, \tag{3.52}$$

which is a measure of the divergence of the numerical solution $\mathbf{b}$. A second-order finite difference approximation is used to compute the divergence at each grid point (Press *et al.*, 2007). In principle $E_{\rm div}$ should be zero, but this is not achieved in practice due to the finite numerical accuracy of the solution, and the truncation error introduced by the numerical approximation to differentiation. The truncation error in the derivative has a scaling $\sim 1/N^2$ (Press *et al.*, 2007).

The left panel of Figure 3.4 shows $E_{\rm m}$ and $E_{\rm CS}$ for the initial potential field (plus signs and crosses), and for the numerical solution after 30 Grad-Rubin iterations (diamonds and squares), as functions of grid size N. The error associated with the potential field is independent of N. For the Grad-Rubin solution both $E_{\rm m}$ and $E_{\rm CS}$ decrease approximately as power laws, *i.e.* show scalings $\sim N^{\gamma}$, where we find (based on least squares fits) $\gamma = -1.3$ for $E_{\rm m}$ and $\gamma = -2.3$ for $E_{\rm CS}$. The power-law fits are shown in Figure 3.4 by the dashed lines. The scaling for $E_{\rm m}$ is close to the expected $\sim 1/N$ scaling discussed in Section 3.3.2, while the scaling for $E_{\rm CS}$ is closer to $\sim 1/N^2$.

The left panel of Figure 3.5 shows $E_{\rm div}$ as a function of N for the numerical solution after 30 Grad-Rubin iterations (diamonds) and the analytic solution (plus signs). The two data sets overlap indicating that

[2]These metrics are chosen because they show the largest discrepancy between the numerical and the analytic fields.

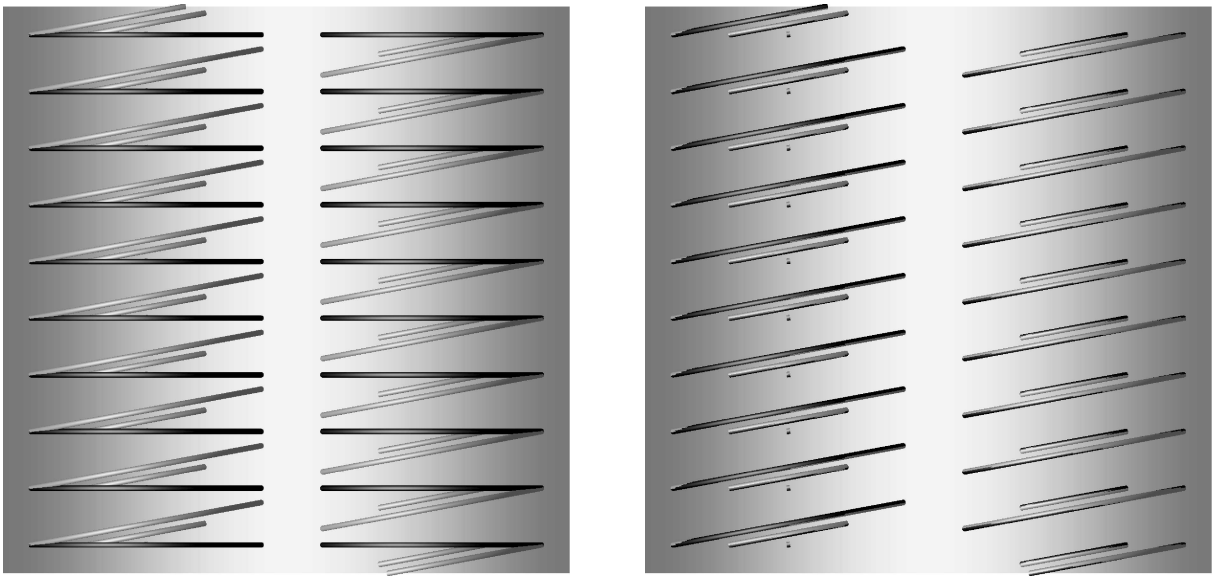

Figure 3.3: Comparisons between the field lines for the analytic solution, the Grad-Rubin solution and the initial potential field for the test case calculation in Section 3.5.1. The left panel shows the analytic solution (light field lines) and the potential field (dark field lines). The right panel shows the analytic solution (light field lines) and the numerical solution after 30 Grad-Rubin iterations (dark field lines). The solutions are viewed looking down from the top of the computational domain. The $z = 0$ plane is shaded to show $B_{\rm obs}$ (regions with $B_{\rm obs} > 0$ are dark and those with $B_{\rm obs} < 0$ are light). The solution after 30 Grad-Rubin iterations closely matches the analytic solution.

the divergence of the numerical solution is close to or smaller than the truncation error in the numerical derivative. In common with $E_{\rm m}$ and $E_{\rm CS}$, the metric $E_{\rm div}$ for the Grad-Rubin solution has power-law scaling $\sim N^{\gamma}$. We estimate $\gamma = -2.0$ based on a least squares fit to the data for the Grad-Rubin solution (the power-law fit is shown as a dashed line in the figure).

We also measure the run time of the code for different grid sizes using the CPU clock (the tests are performed on an eight core CPU). Figure 3.6 shows the execution time for 30 Grad-Rubin iterations as a function of N. The results appear to follow a power law $\sim N^{\gamma}$, and we estimate $\gamma = 3.8$ based on a least squares fit to the three data points (the fit is shown by the dashed line). This scaling is close to the $\sim N^4$ scaling expected for the field line tracing discussed in Section 3.3.2. This scaling implies that the field line tracing is the computationally slowest step in the calculation.

3.5.2 Test Case with Closed Side Boundaries

For the second test we use the parameters $k = \pi/L$, $\lambda = 0.9\pi/L$, and $a_0 = 1$. The grid sizes are the same as in Section 3.5.1, and we apply 50 Grad-Rubin iterations starting from a potential field.

The right panel of Figure 3.2 shows $\Delta B_{\rm avg}$ over 50 Grad-Rubin iterations for the three grid sizes used. For all three cases $\Delta B_{\rm avg}$ decreases exponentially for roughly 40 iterations before becoming approximately constant. The rate of convergence does not appear to depend strongly on the grid size.

Figure 3.7 shows the field lines of the analytic solution, the potential field, and the Grad-Rubin solution. The view in the two panels in the figure is along the y axis. The left panel shows the field lines of the initial potential field (dark field lines) and of the analytic solution (light field lines). The right panel shows the field lines of the Grad-Rubin solution after 50 Grad-Rubin iterations (dark field lines) and of the analytic solution (light field lines). The Grad-Rubin solution closely matches the analytic solution.

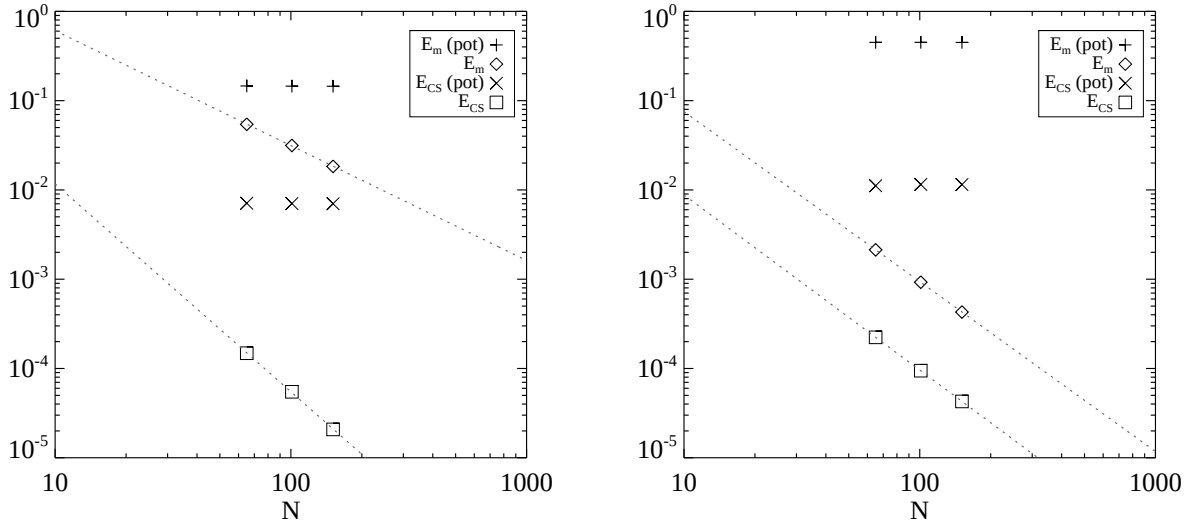

Figure 3.4: Error metrics $E_{\rm m}$ (see Equation (3.50)) and $E_{\rm CS}$ (see Equation (3.51)) as a function of grid size N for the initial potential field (plus signs and crosses), and for the numerical solution (diamonds and squares). The left panel shows the results for the test cases with periodic side boundary conditions after 30 Grad-Rubin iterations, and the right panel shows the results for the test cases with closed side boundary conditions after 50 Grad-Rubin iterations. The Grad-Rubin solutions show power-law scaling $E_{\rm m} \sim N^{\gamma}$ and $E_{\rm CS} \sim N^{\gamma}$, and the dashed lines show power-law fits to the data. The power-law indices γ for each fit are summarised in Table 3.1.

Table 3.1: Power law indices γ for the scaling of the error metrics $E_{\rm m}$, $E_{\rm CS}$, and $E_{\rm div}$ with grid size.

Test case	$E_{\rm m}$	$E_{\rm CS}$	$E_{\rm div}$
Periodic	-1.3	-2.3	-2.0
Closed	-1.9	-2.0	-1.4

The right panel of Figure 3.4 shows the error metrics $E_{\rm m}$ and $E_{\rm CS}$ for the initial potential field (plus signs and crosses), and for the numerical solution after 50 Grad-Rubin iterations (diamonds and squares). The error associated with the potential field is independent of N. For the Grad-Rubin solution both $E_{\rm m}$ and $E_{\rm CS}$ decrease as power-laws, with indices $\gamma = -1.9$ for $E_{\rm m}$ and $\gamma = -2.0$ for $E_{\rm CS}$ (based on least-squares fits, shown by the dashed lines). Both error metrics are found to scale approximately as $1/N^2$. The expected scaling, discussed in Section 3.3.2, is $\sim 1/N$. The improvement in the observed scaling may be due to the simplicity of the solution (for this solution $B_y = 0$) and is unlikely to occur more generally.

The right panel of Figure 3.5 shows the error metric $E_{\rm div}$ as a function of N for the numerical solution after 50 Grad-Rubin iterations (diamonds) and for the analytic solution (plus signs). In this case $E_{\rm div}$ for the Grad-Rubin solution has power-law with index $\gamma = -1.4$ (based on a least squares fit to the data, shown as a dashed line in the figure). The analytic solution has a power-law scaling in $E_{\rm div}$ with $\gamma = -2.0$ (the fit is not shown). There is a substantial difference between $E_{\rm div}$ for the analytic and numerical solution indicating that $E_{\rm div}$ is providing a measure of the residual divergence of the numerical solution and is not due to the truncation error incurred by the numerical approximation to differentiation.

3.6 Discussion and Conclusion

We present an implementation of the Grad-Rubin method for solving the magneto-hydrostatic equations in a finite domain. The code allows two possible choices of boundary conditions on the side boundaries of the domain: either $\mathbf{B}$ is periodic on the side boundaries, or the normal component of $\mathbf{B}$ is zero on the side

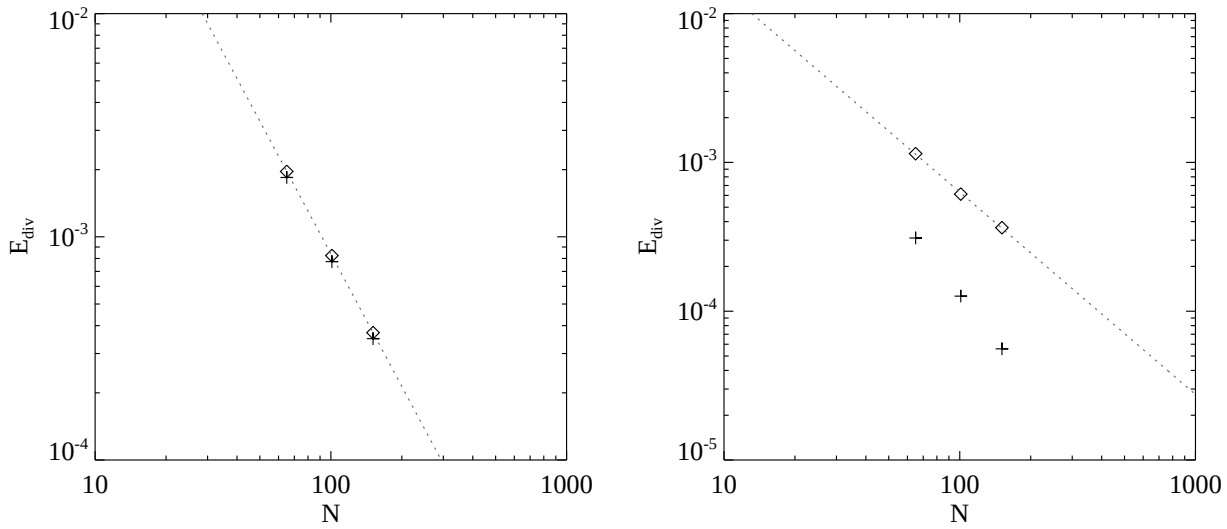

Figure 3.5: The absolute value of the divergence of the numerical solution and initial potential fields, averaged over the computational domain $E_{\rm div}$ (see Equation (3.52)) as a function of grid size N. The left panel shows $E_{\rm div}$ for the analytic solution (plus signs) and the numerical solution after 30 Grad-Rubin iterations for the test case with periodic boundary conditions. The right panel shows $E_{\rm div}$ for the analytic solution (plus signs) and the numerical solution after 50 Grad-Rubin iterations for the test case with closed boundary conditions. The dashed lines are power-law fits ($\sim N^{\gamma}$) to $E_{\rm div}$ for the numerical solutions. The power-law indices are $\gamma = -2.0$ for the data in the left panel, and $\gamma = -1.4$ for the data in the right panel. The power-law index for $E_{\rm div}$ for the analytic solutions in both panels is $\gamma = -2.0$. The fits are not shown.

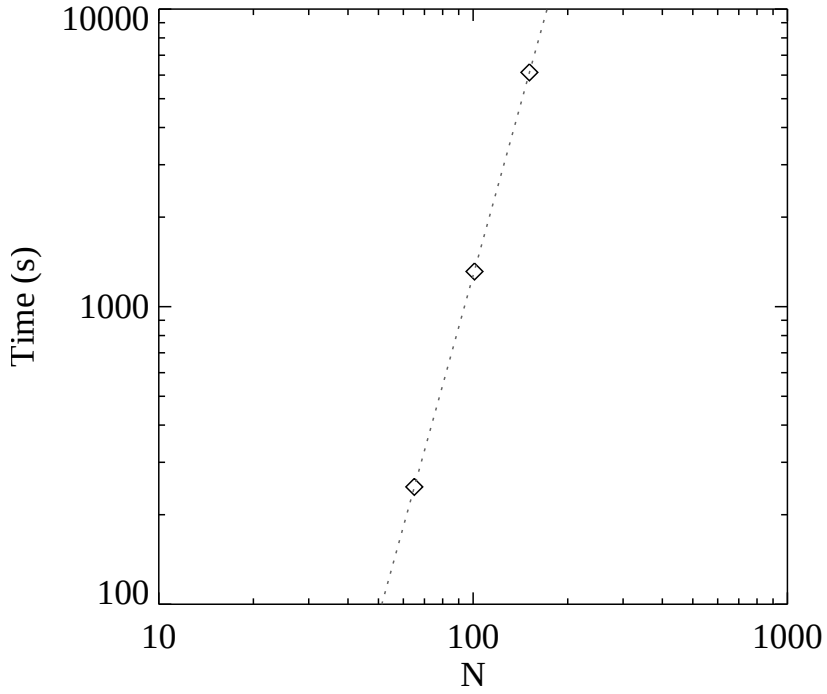

Figure 3.6: Execution time for 30 Grad-Rubin iterations as a function of grid size N for the first test case (Section 3.5.1). The execution time has power-law scaling with a power-law index $\gamma = 3.8$ based on a least-squares fit to the data (the dashed line).

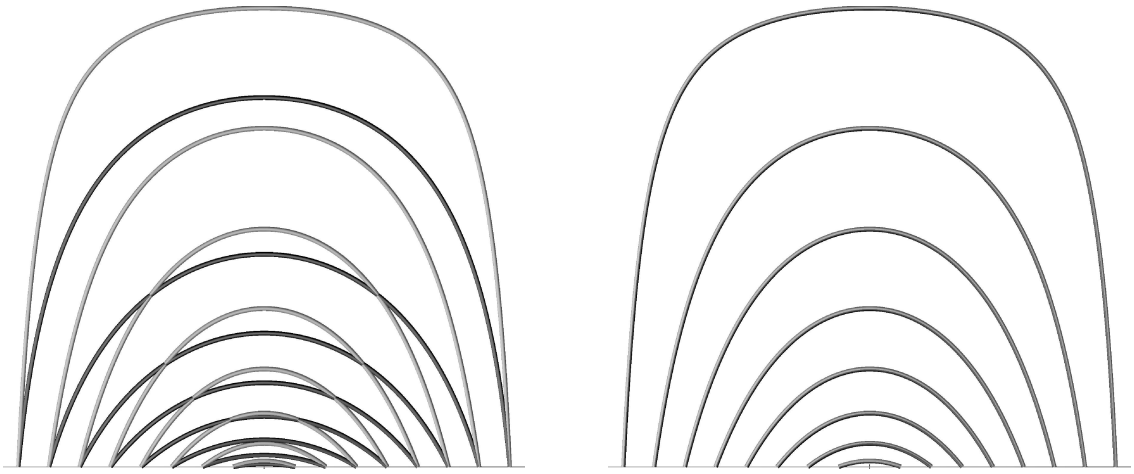

Figure 3.7: Comparison between the field lines for the analytic solution, the Grad-Rubin solution and the initial potential field for the test case in Section 3.5.2. The left panel shows the analytic solution (light field lines) and the potential field (dark field lines). The right panel shows the analytic solution (light field lines) and the numerical solution after 50 Grad-Rubin iterations (dark field lines). The view is along the y axis in both panels. The Grad-Rubin solution closely matches the analytic solution.

boundaries. We refer to these choices as periodic boundary conditions and closed boundary conditions. In both cases the normal component of $\mathbf{B}$ is zero on the top boundary of the domain.

The code is tested in application to a simple analytic solution, for two choices of parameters for the solution, which illustrate the periodic and closed boundary conditions respectively. In both cases the code accurately reconstructs the test solution. Several runs are performed for each test case with varying grid sizes, to demonstrate the scaling of the method with the size of the problem. The test case is highly idealised. The lower boundary conditions are exactly consistent with the magneto-hydrostatic model because they are derived from an exact solution, and the top and side boundary conditions exactly match the assumptions adopted for the numerical method. The idealisation allows a rigorous test of the correctness of the implementation.

For both test cases the Grad-Rubin method converges. The convergence is measured using the average absolute change ΔB_{avg} in the field (see Equation (3.49)). The test case with periodic boundary conditions converges faster than the test case with closed boundary conditions, measured in the number of iterations. This is likely due to the second test case being significantly more non-potential than the first, rather than being due to the different boundary conditions.

The code is found to accurately reproduce the analytic test cases. This is confirmed by a visual comparison of the field lines of the analytic solution and the reconstructed solution. For both choices of parameters/boundary conditions the numerical solution succeeds, based on this test. We also measure the success using the mean vector error E_{m} which is defined by Equation (3.50), and the Cauchy-Schwartz inequality based metric E_{CS}, which is defined by Equation (3.51). We also compute a measure of the residual divergence E_{div} which is defined by Equation (3.52). In the absence of numerical error we would expect $E_{\mathrm{m}} = E_{\mathrm{CS}} = E_{\mathrm{div}} = 0$. For both test cases E_{m}, E_{CS}, and E_{div} decrease as N increases, with a power-law scaling in N, and we estimate the power-law index in each case from a least-squares fit to the data. The power-law indices are summarised in Table 3.1. We obtain different scalings for the different metrics in each case. This may be attributed to the difference between the two test cases, and the different metrics. The slowest scaling achieved is $\sim 1/N$ in each case, which is consistent with other Grad-Rubin implementations (Wheatland, 2006), and with the estimate made in Section 3.3.2. The fastest scaling achieved is $\sim 1/N^2$, which may be attributed to the simple form of the analytic solutions and is unlikely to be achieved for more general solutions. In general we expect a scaling $\sim 1/N$.

The execution time of the code is found to scale as $\sim N^4$, which is comparable to the fastest force-free

Grad-Rubin methods (*e.g.* Wheatland 2006, 2007). However, the magneto-hydrostatic implementation is significantly slower in absolute terms than the force-free methods. The slowest step in both cases (force-free and magneto-hydrostatic) is the field line tracing used to update quantities in the volume at each iteration, and the magneto-hydrostatic case has two field line tracing steps (for $\sigma^{[k]}$ and $p^{[k]}$) compared to one (for $\alpha^{[k]}$) in the force-free case.

This chapter demonstrates the new method and code in application to a simple test case. This is a significant step in the development of magneto-hydrostatic extrapolations of the coronal magnetic field, but several obstacles still remain to be overcome before this can be achieved. One problem is observational: the photospheric pressure profile is not currently available for real solar cases. However, progress might be made by assuming a simple model for the pressure, *e.g.* a constant β model, with $p \propto |\mathbf{B}|^2$. Our model is also overly simplified in that we neglect gravity, and include only a pressure force. We are presently considering ways to include gravity also. Finally, it remains to be seen how well the techniques being developed cope with noisy data, and with data which are not strictly consistent with the magneto-hydrostatic model. Despite these qualifications, the method outlined here, and its successful application to analytic test cases, represents an important first step towards a Grad-Rubin method for magneto-hydrostatic reconstructions of the coronal magnetic field.

3.7 Appendix A

A potential field $\mathbf{B}_0$ satisfying

$$\nabla \times \mathbf{B}_0 = 0 \tag{3.53}$$

and the boundary conditions at $z = 0$

$$\mathbf{B}_0 \cdot \hat{\boldsymbol{z}} = B_{\rm obs} \tag{3.54}$$

is used to initiate the Grad-Rubin iteration. The appropriate field with periodic side boundary conditions is given in Equation (3.29)-(3.31) in the text. For the choice of closed side boundaries the appropriate choice is

$$B_{0x}(x,y,z) = \sum_{m=0}^{\infty}\sum_{n=0}^{\infty} c_{mn} k_m \cosh(k[z-L]) \sin(k_m x) \cos(k_n y), \tag{3.55}$$

$$B_{0y}(x,y,z) = \sum_{m=0}^{\infty}\sum_{n=0}^{\infty} c_{mn} k_n \cosh(k[z-L]) \cos(k_m x) \sin(k_n y), \tag{3.56}$$

and

$$B_{0z}(x,y,z) = -\sum_{m=0}^{\infty}\sum_{n=0}^{\infty} c_{mn} k \sinh(k[z-L]) \cos(k_m x) \cos(k_n y), \tag{3.57}$$

where $k_m = \pi m/L$, $k_n = \pi n/L$, $k^2 = k_m^2 + k_n^2$, and where the coefficients c_{mn} are given by

$$c_{mn} = \frac{4}{L^2} \int_0^L \int_0^L dx dy B_{\rm obs}(x,y) \cos(k_m x) \cos(k_n y) / \sinh(kL). \tag{3.58}$$

Equations (3.55)-(3.58) may be evaluated on a grid with N^3 points in $\sim N^3 \log(N)$ operations using fast sine and cosine transforms (Poularikas, 1996).

3.8 Appendix B

This appendix presents the solution for the current-carrying component of the test field, $\mathbf{B}_c$, with closed top and side boundary conditions. The magnetic field may be calculated from a vector potential $\mathbf{A}$ in the

Coulomb gauge ($\nabla \cdot \mathbf{A} = 0$) using $\nabla \times \mathbf{A} = \mathbf{B}_c$. The vector potential satisfies the vector Poisson equation (Jackson, 1998):

$$\nabla^2 \mathbf{A} = -\mu_0 \mathbf{J}. \tag{3.59}$$

The boundary conditions for $\mathbf{B}_c$ on the six plane boundaries are

$$\mathbf{B}_c \cdot \hat{\boldsymbol{n}} = 0, \tag{3.60}$$

where $\hat{\boldsymbol{n}}$ is the unit vector normal to the boundary. The corresponding boundary conditions for the vector potential in the Coulomb gauge are (Amari, Boulmezaoud, and Mikic, 1999):

$$\partial_n \mathbf{A} = 0, \tag{3.61}$$

and

$$\mathbf{A}_t = 0, \tag{3.62}$$

where $\mathbf{A}_t$ denotes the component of $\mathbf{A}$ transverse to the boundary, and $\partial_n \mathbf{A}$ denotes the normal derivative.

The vector potential $\mathbf{A}$ satisfying the boundary conditions Equations (3.61)-(3.62) can be written as a Fourier series:

$$A_x = \sum_{m=0}^{\infty}\sum_{n=0}^{\infty}\sum_{p=0}^{\infty} a^{(1)}_{mnp} \cos(k_m x)\sin(k_n y)\sin(k_p z), \tag{3.63}$$

$$A_y = \sum_{m=0}^{\infty}\sum_{n=0}^{\infty}\sum_{p=0}^{\infty} a^{(2)}_{mnp} \sin(k_m x)\cos(k_n y)\sin(k_p z), \tag{3.64}$$

and

$$A_z = \sum_{m=0}^{\infty}\sum_{n=0}^{\infty}\sum_{p=0}^{\infty} a^{(3)}_{mnp} \sin(k_m x)\sin(k_n y)\cos(k_p z), \tag{3.65}$$

where $k_m = \pi m/L$, $k_n = \pi n/L$, and $k_p = \pi m/L$. In the following we solve the Poisson equation to find an expression for a_{mnp}. The process is demonstrated for the A_x component, but the approach is similar for the other components.

Substituting Equation (3.63) into the Poisson equation (Equation (3.59)) gives

$$A_x = \sum_{m=0}^{\infty}\sum_{n=0}^{\infty}\sum_{p=0}^{\infty} a^{(1)}_{mnp} k^2 \cos(k_m x)\sin(k_n y)\sin(k_p z) = \mu_0 J_x(x,y,z), \tag{3.66}$$

where $k^2 = k_m^2 + k_n^2 + k_p^2$.

Applying the standard orthogonality relations (where δ_{mn} is the Kronecker delta):

$$\int_0^L \sin(\pi m s/L)\sin(\pi n s/L) ds = \frac{L}{2}\delta_{mn}, \tag{3.67}$$

$$\int_0^L \cos(\pi m s/L)\cos(\pi n s/L) ds = \frac{L}{2}\delta_{mn}, \tag{3.68}$$

and

$$\int_0^L \sin(\pi m s/L)\cos(\pi n s/L) ds = 0 \tag{3.69}$$

yields

$$a^{(1)}_{mnp} = \frac{8\mu_0}{L^3}\int_0^L\int_0^L\int_0^L J_x(x,y,z)\cos(k_m x)\sin(k_n y)\sin(k_p z) dx dy dz. \tag{3.70}$$

Similar expressions apply for the other two coefficients:

$$a^{(2)}_{mnp} = \frac{8\mu_0}{L^3}\int_0^L\int_0^L\int_0^L J_y(x,y,z)\sin(k_m x)\cos(k_n y)\sin(k_p z)dxdydz, \tag{3.71}$$

and

$$a^{(3)}_{mnp} = \frac{8\mu_0}{L^3}\int_0^L\int_0^L\int_0^L J_z(x,y,z)\sin(k_m x)\sin(k_n y)\cos(k_p z)dxdydz. \tag{3.72}$$

The magnetic field is obtained by evaluating $\mathbf{B}_c = \nabla \times \mathbf{A}$. The components of $\mathbf{B}_c$ are

$$B_{cx}(x,y,z) = \sum_{m=0}^{\infty}\sum_{n=0}^{\infty}\sum_{p=0}^{\infty}\left[k_n a^{(3)}_{mnp} - k_p a^{(2)}_{mnp}\right]\sin(k_m x)\cos(k_n y)\cos(k_p z)/k^2, \tag{3.73}$$

$$B_{cy}(x,y,z) = \sum_{m=0}^{\infty}\sum_{n=0}^{\infty}\sum_{p=0}^{\infty}\left[k_p a^{(1)}_{mnp} - k_m a^{(3)}_{mnp}\right]\cos(k_m x)\sin(k_n y)\cos(k_p z)/k^2, \tag{3.74}$$

$$\tag{3.75}$$

and

$$B_{cz}(x,y,z) = \sum_{m=0}^{\infty}\sum_{n=0}^{\infty}\sum_{p=0}^{\infty}\left[k_m a^{(2)}_{mnp} - k_n a^{(1)}_{mnp}\right]\cos(k_m x)\cos(k_n y)\sin(k_p z)/k^2. \tag{3.76}$$

The solution given by Equations (3.73)-(3.76) may be computed on a grid with N^3 points in $\sim N^3\log(N)$ operations using a combination of fast sine and cosine transforms.

Chapter 4

Nonlinear Force-Free Modelling of the Corona in Spherical Coordinates

Abstract

We present a code for solving the nonlinear force-free equations in spherical polar geometry, with the motivation of modelling the magnetic field in the corona. The code is an implementation of the Grad-Rubin method. Our method is applicable to a spherical domain of arbitrary angular size. The implementation is based on a global spectral representation for the magnetic field which makes no explicit assumptions about the form of the magnetic field at the transverse boundaries of the domain. We apply the code to a bipolar test case with analytic boundary conditions, and we demonstrate the convergence of the Grad-Rubin method, and the self-consistency of the resulting numerical solution.

4.1 Introduction

Basic properties of the solar coronal magnetic field such as its strength, direction, and three-dimensional structure, cannot be presently determined by observation, and this motivates modelling of the coronal magnetic field. In the corona above active regions the pressure and gravity forces are too small to balance the magnetic (Lorentz) force (Metcalf *et al.*, 1995; Gary, 2001) so it is common to model the coronal magnetic field as force-free, *i.e.* a magnetic field where the Lorentz force is identically zero, and electric currents flow along magnetic field lines (Sturrock, 1994). Force-free models of the corona were reviewed by Sakurai (1989), and Wiegelmann and Sakurai (2012).

Most of the force-free numerical methods in use solve the force-free equations in Cartesian geometry, with the corona corresponding to the half-space $z > 0$ and the photosphere represented by the $z = 0$ plane (Sakurai, 1981; Wu *et al.*, 1990; Wheatland, Sturrock, and Roumeliotis, 2000; Wiegelmann, 2004; Wheatland, 2007; Valori, Kliem and Keppens, 2005). This introduces two problems into the modelling. The first problem is that the Cartesian approximation, which assumes that the curvature of the Sun in negligible, becomes inaccurate when considering large regions on the Sun (Gary and Hagyard, 1990). Full-disk spectro-polarimetric observations of the photospheric magnetic field are now available from the *Helioseismic and Magnetic Imager* (HMI: Schou *et al.* 2012) aboard the *Solar Dynamics Observatory* (SDO: Pesnell, Thompson, and Chamberlin, 2012). Coronal field modelling based on these data must use spherical coordinates. The second problem concerns the assumption of boundary conditions on the transverse boundaries of the Cartesian domain. In practice the infinite half-space is replaced by a finite numerical domain, meaning boundary conditions are required on the top and side boundaries of the volume in addition to the $z = 0$

plane. In general, *ad hoc* boundary conditions are used, such as assuming periodicity, or assuming that no magnetic flux leaves the top or side boundaries. These boundary conditions are artificial and do not necessarily represent physical conditions in the corona. Spherical modelling avoids this problem, because a spherical domain can encompass the entire corona with no transverse boundaries, in which case *ad hoc* boundary conditions on the transverse boundaries are not required. Although spherical modelling removes the need to impose transverse boundaries conditions, it is still necessary to assume boundary conditions for the magnetic field and electric currents, either at infinity or on a spherical shell of finite radius. These boundary conditions are the spherical equivalent of the "top" boundary in a Cartesian domain.

Modelling the entire corona avoids the need for boundary conditions apart from those at the photosphere, but introduces other difficulties. The description of the polar field presents difficulties both observationally and numerically. The observational difficulties are two-fold. Firstly, due to the Sun's tilt, only one pole is observed from Earth at a time. Secondly, spectro-polarimetrically derived magnetic field values may be inaccurate near the poles where there may be significant unresolved mixed-polarity magnetic flux. This can lead to partial cancellation of the polarisation signal at each pixel. Quiet-Sun regions also contain mixed polarity flux, but the problem is likely to be worse close to the poles due to line-of-sight effects. For these reasons the polar field is usually interpolated from observations at lower latitudes (*e.g.* Sun *et al.* 2011). The co-ordinate singularities in the spherical polar system which occur at the poles also pose a problem for numerical methods. For finite difference methods the coordinate poles require special treatment, and with spectral methods specific grids are required to avoid problems (Boyd, 2001).

In this chapter we outline an implementation of the Grad-Rubin method for solving the nonlinear force-free model in spherical geometry. Our method is applicable both to the entire Sun and to regions with restricted angular extent. Other methods for solving the force-free model in spherical geometry have been developed. Wiegelmann (2007) presented a generalisation of the optimisation method, and Amari *et al.* (2013) presented a finite-difference implementation of the Grad-Rubin method. Our method differs from both of these and features a new spectral method for computing the magnetic field based on an expansion of the field in terms of global basis functions. This solution can be applied to a spherical region of the corona of arbitrary angular size, in which case explicit assumptions about the magnetic field on the transverse boundaries of the spherical region are not required, even for a spherical wedge with restricted extent. However, for the latter case we impose additional constraints on the boundary conditions at the photosphere. Specifically, we assume that the radial component of the field and the electric current density vanish at the photosphere outside the wedge. We present the application of our method to a simple test case with analytic boundary conditions to demonstrate the convergence of the method and the self-consistency of the solution.

This chapter is structured as follows. In Section 4.2 we outline the specific form of the force-free boundary value problem that we solve. In Section 4.3 we present the details of our implementation of the Grad-Rubin method, including the spectral solution for the magnetic field that is used. In Section 4.4 we describe the test case that we use and show the results of applying the code to the test case. Finally, in Section 4.5 we present a discussion of the results and a conclusion.

4.2 Theory

In this section we outline the two boundary value problems that we solve. We consider solutions of the nonlinear force-free equations in two domains. The first domain is the entire corona, and the second is a spherical wedge of limited angular extent.

4.2.1 Boundary Value Problems

We first consider the domain Ω_{global} which is defined as the set of points with spherical polar coordinates

$$\Omega_{\text{global}} = \{(r, \theta, \phi) \mid r \in [R_{\odot}, \infty), \theta \in (0, \pi), \phi \in [0, 2\pi)\}, \tag{4.1}$$

where θ is the polar angle, ϕ is the azimuthal angle, r is the radius, and $R_\odot$ is the radius of the Sun. We refer to this domain as global because it covers a complete 4π steradians, and its lower boundary is the entire photosphere.

It is necessary to specify boundary conditions on the force-free equations at the photosphere. Following the prescription of Grad and Rubin (1958), the appropriate boundary conditions are the radial component of $\mathbf{B}$,

$$\mathbf{B} \cdot \hat{\boldsymbol{r}}|_{r=R_\odot} = B_n(\theta, \phi), \tag{4.2}$$

and the force-free parameter

$$\alpha|_{r=R_\odot} = \alpha_0(\theta, \phi) \tag{4.3}$$

over one polarity of B_n, *i.e.* values of α_0 are specified either where $B_n < 0$ or where $B_n > 0$. It is also assumed that the magnetic field vanishes for large r, *i.e.*

$$\lim_{r\to\infty} \mathbf{B} = 0. \tag{4.4}$$

This asymptotic boundary condition matches that used by some Cartesian codes (Wheatland, 2007).

In some cases B_n and α_0 may only be non-zero over a small range of θ and ϕ. In this situation it is unnecessary to use a global domain. A more appropriate choice is

$$\Omega_{\text{wedge}} = \{(r, \theta, \phi) \mid r \in [R_\odot, \infty), \theta \in [\theta_{\min}, \theta_{\max}], \phi \in [\phi_{\min}, \phi_{\max}]\}, \tag{4.5}$$

i.e. a domain external to a sphere but restricted in angular extent. We refer to this as a spherical wedge. In principle, it is necessary to prescribe boundary conditions at the transverse boundaries of this domain, but in Section 4.3 we explain how to obtain solutions for which this is unnecessary. This approach assumes that B_n and α_0 are zero everywhere outside the domain Ω_{wedge}.

4.2.2 Grad-Rubin Iteration

The Grad-Rubin method is an iterative method for solving the nonlinear force-free equations (Grad and Rubin, 1958). The method has previously been implemented in Cartesian coordinates (Sakurai, 1981; Amari, Boulmezaoud, and Mikic, 1999; Wheatland, 2007) and in spherical coordinates (Amari *et al.*, 2013). The method replaces the nonlinear force-free equations with a set of linear equations which are solved repeatedly in a sequence of iterations. We denote a quantity after k Grad-Rubin iterations using a superscript in square brackets, *e.g.* $\mathbf{B}^{[k]}$. One Grad-Rubin iteration may be written

$$\nabla\alpha^{[k+1]} \cdot \mathbf{B}^{[k]} = 0, \tag{4.6}$$

and

$$\nabla \times \mathbf{B}^{[k+1]} = \alpha^{[k+1]}\mathbf{B}^{[k]}. \tag{4.7}$$

Equation (4.6) updates the force-free parameter α in the volume subject to boundary conditions on α. Equation (4.7) updates the magnetic field in the volume using the new α values together with the magnetic field from the previous iteration subject to the boundary conditions on the normal component of the field. Equations (4.6) and (4.7) are repeatedly solved until the magnetic field $\mathbf{B}^{[k]}$ and the force-free parameter $\alpha^{[k]}$ converge at all points in the volume. The iteration is initiated using a potential field $\mathbf{B}_0$ constructed from the boundary conditions on B_n. We present the details of our method for solving Equations (4.6) and (4.7) numerically in two spherical domains in Section 4.3.

4.3 Numerical Implementation

In this section we outline our implementation of the Grad-Rubin method in code. The Grad-Rubin method requires an initial potential field, a method for solving Equation (4.6) to update α, and a method for solving

Equation (4.7) to update the magnetic field.

The numerical grid used is a spherical polar grid with N_r points in the r direction, N_θ points in the θ direction, and N_ϕ points in the ϕ direction. The ϕ and r grids are uniformly spaced. The θ grid is either a Gauss-Legendre grid or is uniform (Press *et al.*, 2007). The Gauss-Legendre grid is required to accurately represent the solution near the poles and is only necessary for constructing solutions in the global domain. The grid is finite in the radial direction, and has a maximum r value which we call $R_{\max}$.

4.3.1 Spectral Solution for the Potential Field

An initial potential field is calculated as a starting point for the Grad-Rubin iteration. We use a spherical harmonic solution for the potential field. The spherical harmonics are global basis functions, meaning they are orthogonal over the domain Ω_{global}. It can be shown that, in terms of spherical harmonics $Y_{lm}(\theta, \phi)$, the components of the potential field satisfying the boundary condition Equation (4.4) at infinity are (Altschuler and Newkirk, 1969)

$$B_r = \sum_{l=0}^{\infty} \sum_{m=-l}^{l} a_{lm} \left(\frac{R_\odot}{r} \right)^{(l+2)} Y_{lm}(\theta, \phi), \tag{4.8}$$

$$B_\theta = \sum_{l=0}^{\infty} \sum_{m=-l}^{l} -\frac{a_{lm}}{l+1} \left(\frac{R_\odot}{r} \right)^{(l+2)} \frac{\partial Y_{lm}(\theta, \phi)}{\partial \theta} \tag{4.9}$$

and

$$B_\phi = \sum_{l=0}^{\infty} \sum_{m=-l}^{l} -\frac{ima_{lm}}{l+1} \left(\frac{R_\odot}{r} \right)^{(l+2)} \frac{Y_{lm}(\theta, \phi)}{\sin\theta}, \tag{4.10}$$

where the coefficients a_{lm} are given by

$$a_{lm} = \int_0^{2\pi} \int_0^{\pi} B_n(\theta, \phi) Y^*_{lm}(\theta, \phi) \sin\theta d\theta d\phi, \tag{4.11}$$

and where $i^2 = -1$. These equations are complex valued and the physical magnetic field is the real part. Equations (4.8)-(4.11) can be obtained from the well-known potential source-surface solution (Altschuler and Newkirk, 1969) by considering that solution in the limit where the source surface is located at infinity.

In practice the series must be truncated after a finite number of terms. We truncate the series at a finite l value which we call L, *i.e.* we perform the summation over all the spherical harmonics with $l \leq L$ and $|m| \leq l$. This approach results in a truncation error in $\mathbf{B}$ which is position independent (Boyd, 2001). The series is a Fourier series in ϕ, so it is natural to choose L to correspond to the Nyquist frequency (Boyd, 2001):

$$L = \frac{\pi}{\Delta\phi}, \tag{4.12}$$

where $\Delta\phi$ is the uniform spacing of points in ϕ. In practice the right hand side of Equation (4.12) is rounded to the nearest integer.

Equations (4.8)-(4.11) provide the magnetic field at all points in the global domain Ω_{global}. The solution in the restricted domain Ω_{wedge} can be found by evaluating the global solution only at points contained in Ω_{wedge}. This allows the solution in Ω_{wedge} to be found without assuming specific boundary conditions on the transverse boundaries of Ω_{wedge}. Since we assume that B_n is zero outside Ω_{wedge}, the integral in Equation (4.11) need only be computed over the restricted domain.

Tóth, van der Holst, and Huang (2011) report the non-convergence of the spectral series given by Equations (4.9)-(4.10). The non-convergence results in erroneous magnetic field values (particularly near the poles)

for large L. The problem occurs because the numerical grid used by Tóth, van der Holst, and Huang (2011) is not sufficiently dense near the poles to accurately represent the rapid variation of the spherical harmonics. For calculations in $\Omega_{\rm global}$ we use a Gauss-Legendre grid which accurately represents the spherical harmonics near the poles (Boyd, 2001). For calculations in $\Omega_{\rm wedge}$, we use uniform grid in θ, which is rotated such that the region of interest is isolated from the poles, and does not encounter this problem.

The Gibbs phenomenon (ringing produced in representing discontinuous changes) is a problem for all spectral methods (Boyd, 2001). The problem is significant when spectral potential field solutions are calculated from observational data (Tóth, van der Holst, and Huang, 2011). Including more terms in the series improves but does not eliminate the problem. It is important to note this particular caveat when applying and interpreting results produced by spectral methods. It should be noted that finite difference methods also become inaccurate at locations with large gradients in the field being represented.

A parallel code is used to sum the spectral series. The coefficients a_{lm} are calculated using Equation (4.11) and then Equations (4.8)-(4.10) are evaluated with the sums performed using partial sums, *i.e.* each series is broken into a number of sub-series, each of which is summed independently, and then the final result is obtained by adding the partial sums. The parallel implementation is written for a distributed memory multiprocessor. The method uses a combination of the Message Passing Interface (MPI) (Snir *et al.*, 1998) and OpenMP (Chandra *et al.*, 1990) and is described in the appendix.

4.3.2 Field Line Tracing Solution for the Current-Update Step

To solve Equation (4.6) we employ the field line tracing method which has been used in Grad-Rubin implementations in Cartesian coordinates (Amari, Boulmezaoud, and Mikic, 1999; Wheatland, 2007), and in spherical coordinates (Amari *et al.*, 2013). According to Equation (4.6), $\alpha^{[k+1]}$ is constant along magnetic field lines. The field line tracing method determines $\alpha^{[k+1]}$ in the volume by tracing the field line threading each grid point until it crosses the lower boundary, and the value of α_0 at the crossing point in the boundary is assigned to the grid point. The field line is traced in the forwards direction if boundary values for α_0 are chosen where $B_n < 0$, and is traced in the backwards direction if boundary values for α_0 are chosen where $B_n > 0$. Points in the volume connected to field lines which leave the domain through the outer boundary $r = R_{\rm max}$ are assigned $\alpha^{[k+1]} = 0$ at the point in the volume. In addition, points in the volume threaded by field lines which leave the transverse boundaries of $\Omega_{\rm wedge}$ are assigned $\alpha^{[k+1]} = 0$ at the point in the volume. The tracing is performed using fourth-order Runge-Kutta integration, and trilinear interpolation is used to determine $\mathbf{B}^{[k]}$ at points along the field line not coinciding with a grid point (Press *et al.*, 2007).

4.3.3 Spectral Solution to Ampere's Law for the Field-Update Step

To solve Equation (4.7) we use a spectral solution. The magnetic field is decomposed into the sum of a potential field and a non-potential field, *i.e.*

$$\mathbf{B}^{[n+1]} = \mathbf{B}_0 + \mathbf{B}_c^{[n+1]}, \tag{4.13}$$

where $\mathbf{B}_c^{[n+1]}$ satisfies

$$\nabla \times \mathbf{B}_c^{[k+1]} = \mathbf{J}^{[k+1]}, \tag{4.14}$$

with

$$\mathbf{J}^{[k+1]} = \alpha^{[k+1]}\mathbf{B}^{[k]}/\mu_0, \tag{4.15}$$

and where $\mathbf{B}_0$ is the potential field matching the boundary conditions on B_n calculated using the method of Section 4.3.1. It is only necessary to update $\mathbf{B}_c^{[k+1]}$ at each iteration as $\mathbf{B}_0$ does not change. Also, since $\mathbf{B}_0$ satisfies the boundary conditions on the normal component of the field at $r = R_\odot$ it follows that

$$\mathbf{B}_c^{[k+1]}|_{r=R_\odot} = 0, \tag{4.16}$$

and from Equation (4.4) we require

$$\lim_{r\to\infty} \mathbf{B}_c^{[k+1]} = 0. \tag{4.17}$$

Equations (4.16) and (4.17) define the boundary conditions on $\mathbf{B}_c^{[k+1]}$.

We use a spectral solution to Equation (4.14) which is analogous to the spherical harmonic solution for the potential field. We express $\mathbf{B}_c^{[k+1]}$ as a series using the vector spherical harmonics (Morse and Feshbach, 1953), *i.e.*

$$\mathbf{B}_c^{[k+1]} = \sum_{l=0}^{\infty}\sum_{m=-l}^{l} B_{lm}^{(1)}(r)\mathbf{Y}_{lm} + B_{lm}^{(2)}(r)\mathbf{\Psi}_{lm} + B_{lm}^{(3)}(r)\mathbf{\Phi}_{lm}, \tag{4.18}$$

where $\mathbf{Y}_{lm}$, $\mathbf{\Psi}_{lm}$, and $\mathbf{\Phi}_{lm}$ are the complete set of orthogonal vector basis functions defined by

$$\mathbf{Y}_{lm} = Y_{lm}\hat{\mathbf{r}}, \tag{4.19}$$

$$\mathbf{\Psi}_{lm} = \frac{r\nabla Y_{lm}}{\sqrt{l(l+1)}}, \tag{4.20}$$

and

$$\mathbf{\Phi}_{lm} = \frac{\mathbf{r}\times\nabla Y_{lm}}{\sqrt{l(l+1)}}. \tag{4.21}$$

These functions are mutually perpendicular, *i.e.*

$$\mathbf{Y}_{lm}\cdot\mathbf{\Psi}_{lm} = \mathbf{Y}_{lm}\cdot\mathbf{\Phi}_{lm} = \mathbf{\Psi}_{lm}\cdot\mathbf{\Phi}_{lm} = 0, \tag{4.22}$$

and orthonormal, *e.g.*

$$\int_0^{\pi}\int_0^{2\pi} \mathbf{Y}_{lm}(\theta,\phi)\cdot\mathbf{Y}^*_{l'm'}(\theta,\phi)d\theta d\phi = \delta_{ll'}\delta_{mm'}, \tag{4.23}$$

where δ_{lm} is the Kronecker delta[1]. The vector spherical harmonics have previously been applied to magnetostatic problems (*e.g.* Barrera, Estévez, and Giraldo, 1985; Dennis and Quartapelle 1985), but have not been used in this context.

The spectral coefficients $B_{lm}^{(i)}$ with $i = 1, 2, 3$ are determined by the distribution of currents in the volume and by the boundary conditions. We show in Chapter 5 that for the problem at hand the spectral coefficients for the magnetic field are

$$B_{lm}^{(1)} = \frac{\sqrt{l(l+1)}}{r}\left[-R_{\odot}^{l}\left(\frac{R_0}{r}\right)^{l+1} I_0 + I_2(r) + I_3(r)\right], \tag{4.24}$$

$$B_{lm}^{(2)} = \frac{1}{r}\left[R_{\odot}^{l}\left(\frac{R_{\odot}}{r}\right)^{l+1} I_0 - lI_1(r) + (l+1)I_2(r)\right], \tag{4.25}$$

and

$$B_{lm}^{(3)} = \frac{rJ_{lm}^{(1)}}{\sqrt{l(l+1)}}, \tag{4.26}$$

where

$$I_0 = \frac{\mu_0}{2l+1}\int_{R_{\odot}}^{\infty} s^{1-l}J_{lm}^{(3)}(s)ds, \tag{4.27}$$

$$I_1(r) = \frac{\mu_0}{2l+1}\int_{R_{\odot}}^{r} s\left(\frac{s}{r}\right)^{l+1} J_{lm}^{(3)}(s)ds, \tag{4.28}$$

and

$$I_2(r) = \frac{\mu_0}{2l+1}\int_{r}^{\infty} s\left(\frac{r}{s}\right)^{l} J_{lm}^{(3)}(s)ds. \tag{4.29}$$

[1] A similar integral relation applies for $\mathbf{\Psi}_{lm}$ and $\mathbf{\Phi}_{lm}$.

The coefficients $J_{lm}^{(i)}$ are the spectral coefficients of the current distribution defined by

$$J_{lm}^{(1)}(r) = \int \mathbf{J}^{[k+1]} \cdot \mathbf{Y}_{lm}^{*} d\Omega, \tag{4.30}$$

$$J_{lm}^{(2)}(r) = \int \mathbf{J}^{[k+1]} \cdot \mathbf{\Psi}_{lm}^{*} d\Omega, \tag{4.31}$$

and

$$J_{lm}^{(3)}(r) = \int \mathbf{J}^{[k+1]} \cdot \mathbf{\Phi}_{lm}^{*} d\Omega, \tag{4.32}$$

where $\mathbf{J}^{[k+1]}$ is the volume current density defined by Equation (4.15). The spectral solution is computed in three steps: i) $J_{lm}^{(i)}$ is computed from $\mathbf{J}^{[k+1]}$ using Equations (4.30)-(4.32); ii) spectral coefficients for the magnetic field are computed from Equations (5.77)-(5.80); iii) the spectral series is summed to a maximum order L. A parallel summation method is used, as described in the appendix (the method is described for the potential field calculation, but the same approach is also used for the non-potential component of the field).

The integrals I_0, I_1, and I_2 [Equations (4.27), (4.28), and (4.29)] are evaluated using the trapezoidal rule. The integrals are expressed in a such a way as to avoid numerical overflow for large values of l. Although the integrals in Equations (4.27) and (4.29) are written as extending to infinite radius, in the numerical solution the maximum radius is $R_{\max}$, and an error is introduced by this approximation if $\mathbf{J}^{[n+1]} \neq 0$ at $r = R_{\max}$. Therefore it is necessary to make $R_{\max}$ sufficiently large to encompass all the significant currents.

4.4 Application to Test Cases

In this section we apply our code to two test cases with analytic boundary conditions, to demonstrate the method. We establish the convergence of the method and quantify the self-consistency of the solution.

4.4.1 Two Bipolar Test Cases

The first test case is a simple model with analytic boundary conditions, representing the field due to a bipolar active region with Gaussian sunspots calculated in the global domain Ω_{global}. A small non-zero patch of α is included around one of the spots. The second test case has the same boundary conditions, on a smaller spatial scale, and the field is calculated in a restricted domain Ω_{wedge}. For each test case we demonstrate the convergence of the Grad-Rubin iteration, and we measure the self-consistency of the solution by verifying that the Lorentz force in the model corona is zero, *i.e.* that the electric current is parallel to the magnetic field.

For both test cases, the boundary conditions on the magnetic field are

$$B_n(\theta, \phi) = B_{\text{s}} \left(e^{-s_1^2/\sigma^2} - e^{-s_2^2/\sigma^2} \right), \tag{4.33}$$

where B_{s} is a scale constant, and σ is a parameter which determines the size of the spots. For the numerical calculation we normalise B_n such that $\max(|B_n|) = B_{\text{s}}$. The two functions s_1 and s_2 are distances to the centres of each spot as measured on the sphere, and may be written

$$s_i(\theta, \phi) = R_{\odot} \tan^{-1} \left[\frac{\sqrt{(\sin\theta \sin\Delta\lambda)^2 + (\sin\theta_i \cos\theta - \sin\theta \cos\theta_i \cos\Delta\lambda)^2}}{\cos\theta_i \cos\theta + \sin\theta \sin\theta_i \cos\Delta\lambda} \right], \tag{4.34}$$

where $\Delta\lambda = \phi_i - \phi$, and with (θ_1, ϕ_1) being the coordinates of the centre of the spot with positive polarity, and with (θ_2, ϕ_2) being the coordinates of the centre of the spot with negative polarity. For the boundary

conditions on α_0 we consider an isolated spot with a locally constant value of α around the centre of the positive spot, *i.e.*

$$\alpha_0 = \begin{cases} \Lambda & B_n \geq B_{\rm th} \\ 0 & 0 < B_n < B_{\rm th} \end{cases}, \tag{4.35}$$

where Λ is a constant, and $B_{\rm th}$ is a threshold value. Note that the boundary conditions on α_0 are only defined over one polarity of B_n (as per the Grad-Rubin formulation). We have chosen to define α_0 over the positive polarity of B_n, *i.e.* where $B_n > 0$.

It is known that force-free fields can be unstable when (Molodensky, 1974)

$$\alpha_{\rm s} L_{\rm s} > 1, \tag{4.36}$$

where $\alpha_{\rm s}$ is a characteristic value for α, and $L_{\rm s}$ is the characteristic scale length. For the bipolar test case we take the scale length to be the distance along the photosphere between the two spots, and we take $\alpha_{\rm s} = \Lambda$. For both test cases we choose these values such that

$$\alpha_{\rm s} L_{\rm s} \approx 1, \tag{4.37}$$

corresponding to a current close to the approximate maximum stable value.

4.4.2 Measures of Convergence

To measure the convergence of the iteration we employ two metrics. The first is the total magnetic energy at each iteration k:

$$E_k = \frac{1}{2\mu_0} \int \left| \mathbf{B}^{[k]} \right|^2 dV, \tag{4.38}$$

where the integral is over the entire computational volume. We expect the energy to converge to a fixed value with Grad-Rubin iteration. The second metric is the average absolute difference in the magnetic field at successive Grad-Rubin iterations:

$$A_{\rm mean} = \left\langle \left| \mathbf{B}^{[k]} - \mathbf{B}^{[k-1]} \right| \right\rangle, \tag{4.39}$$

where $\langle ... \rangle$ denotes the average over the computational volume. We expect $A_{\rm mean}$ to approach zero with repeated iteration.

To measure the self consistency of the solution, we consider the maximum angle between $\mathbf{J}$ and $\mathbf{B}$. The angle is defined by

$$\theta_{\rm max} = \max \left[\frac{\left| \mathbf{J}^{[k]} \times \mathbf{B}^{[k]} \right|}{\left| \mathbf{B}^{[k]} \right| \left| \mathbf{J}^{[k]} \right|} \right], \tag{4.40}$$

where the maximum is calculated over all grid points.

We also examine the self-consistency qualitatively by drawing the field lines of $\mathbf{B}^{[k]}$ and streamlines of the current density $\mathbf{J}^{[k]}$. For an exact force-free solution we expect that these two sets of field lines will coincide corresponding to $\theta_{\rm max} = 0$. This provides quite a stringent test, because the error in the paths of the field lines is the result of the local truncation error in the solution integrated along the paths, which is in general greater than the local error.

4.4.3 Results for Test Case One: the Bipole in the Global Domain

The first test case described in Section 4.4.1 considers a bipolar active region covering a significant fraction of the photosphere. This region provides a test for the method in the domain $\Omega_{\rm global}$. The parameters used for this test are shown in Table 4.1, and the dimensions of the grid are summarised in Table 4.2. We perform

Table 4.1: Parameters used for the bipolar test cases involving the domain Ω_{global} (Case 1), and the wedge-shaped region Ω_{wedge} (Case 2). Distances are quoted in units of a solar radius, angles are quoted in units of degrees, and the magnetic field strengths are relative to the scale constant B_{s}. Units are given in square brackets.

Case	σ $[R_\odot]$	L_{s} $[R_\odot]$	Λ $[R_\odot^{-1}]$	$\alpha_{\text{s}} L_{\text{s}}$	B_{th} $[B_s]$	(θ_1, ϕ_1) [degrees]	(θ_2, ϕ_2) [degrees]
1	0.1	0.35	3	1.05	0.75	$(0, 190)$	$(0, 170)$
2	0.02	0.035	30	1.05	0.75	$(0, 181)$	$(0, 179)$

Table 4.2: Size of the grids used for test cases. Both the physical sizes and the sizes of the numerical grids are shown.

Case	Domain	N_r	N_θ	N_ϕ	Lon [degrees]	Lat [degrees]	$R_{\max}$ $[R_\odot]$
1	Ω_{global}	128	64	128	360	180	6
2	Ω_{wedge}	64	64	64	20	20	1.2

40 Grad-Rubin iterations starting from a potential field. The computation takes approximately 15 minutes on a computer with an eight-core CPU.

The left panel of Figure 4.1 illustrates the energy (in units of the energy of the potential field E_0) as a function of iteration number. The energy converges to an approximately constant value after about six Grad-Rubin iterations. The left panel of Figure 4.2 shows the absolute average change in the field, A_{mean}, as a function of iteration number. The scale on the y axis is logarithmic. This figure shows that A_{mean} decreases exponentially to a value of the order 10^{-9}. The behaviour of the two metrics E/E_0 and A_{mean} establishes the convergence of the Grad-Rubin procedure for this case.

We also demonstrate the self-consistency of the numerical solution. Figure 4.3 shows the field lines of $\mathbf{B}$ (in blue) and the streamlines of $\mathbf{J}$ (in red). The left panel shows the results after one Grad-Rubin iteration. In this panel there is a significant discrepancy between the two sets of lines. The right panel shows the field lines after 40 Grad-Rubin iterations. In this case the two sets of lines almost coincide, indicating that the numerical solution is close to being force-free. Some discrepancy is observed for long field lines because of the need to interpolate values of $\mathbf{J}$ and $\mathbf{B}$ between grid points in order to draw field lines. At each grid point $\mathbf{J} \times \mathbf{B}$ is very small (as discussed below), but larger values are obtained between grid points when $\mathbf{J}$ and $\mathbf{B}$ are interpolated. The field lines which show the largest discrepancy occur close to the boundary separating zero and non-zero values of α_0, where the interpolation is least accurate.

The left panel of Figure 4.4 shows $\theta_{\max}$ as a function of iteration number. After the first iteration the maximum angle between $\mathbf{J}$ and $\mathbf{B}$ is approximately 20 degrees, and $\theta_{\max}$ decreases approximately exponentially over the 40 iterations to a final value of order 10^{-3} degrees. This confirms that a force-free solution is found.

4.4.4 Results for Test Case Two: the Bipole in the Restricted Domain

The second test case described in Section 4.4.1 considers the bipolar test case in the domain Ω_{wedge}. We choose a domain which spans 20° in latitude and 20° in longitude. The size and the dimensions of the numerical grid are summarised in Table 4.2. In this case, the separation between the spots is an order of magnitude smaller than for the first test case, so we increase α_{s} by an order of magnitude so that the product $L_{\text{s}}\alpha_{\text{s}}$ matches test case one. This provides a bipole with the same amount of twist. The parameters for this test case are summarised in Table 4.2. We again apply 40 Grad-Rubin iterations, which takes 1.6 hours to run on a computer with an eight-core CPU.

The right panel of Figure 4.1 shows the energy (in units of the energy of the potential field E_0) as a function of iteration number. The energy converges to a constant value after approximately four Grad-Rubin

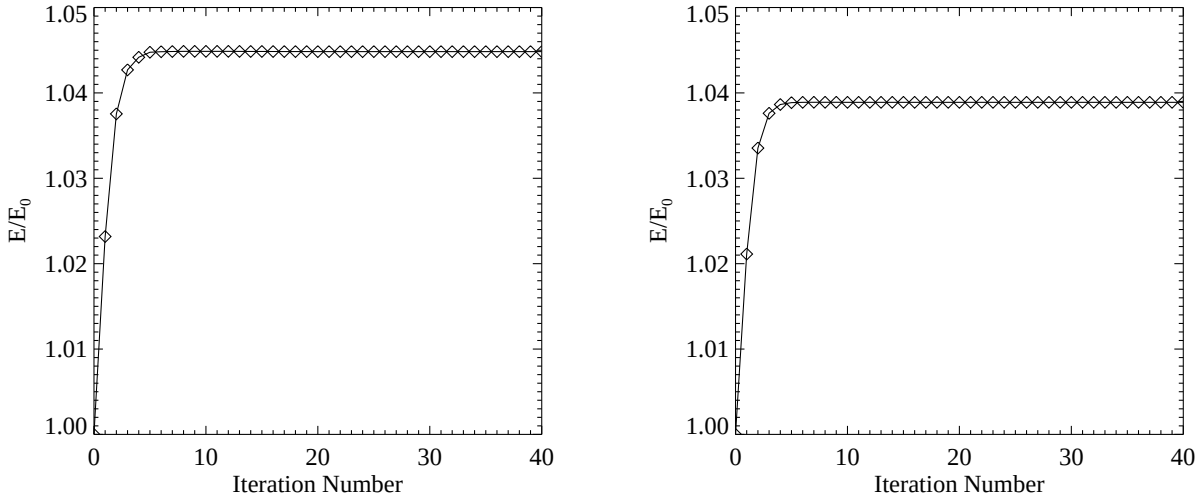

Figure 4.1: Energy (in units of the energy of the potential field E_0) as a function of iteration number. The left panel shows E/E_0 for the first test case in the global domain $\Omega_{\rm global}$, and the right panel shows the same for the second test case, involving a calculation in the domain $\Omega_{\rm wedge}$. In both cases the energy converges to an approximately constant value after about six iterations.

iterations. The right panel of Figure 4.2 shows $A_{\rm mean}$ as a function of iteration number. The scale on the y axis is logarithmic, and the figure shows that $A_{\rm mean}$ decreases approximately exponentially, to a final value the order of machine precision. The behaviour of E/E_0 and $A_{\rm mean}$ as a function of iteration confirm the convergence of the Grad-Rubin iteration procedure.

The left panel of Figure 4.5 shows the field lines of the magnetic field and the streamlines of the current density after the first iteration (left panel) and after the last iteration (right panel). The magnetic field is shown in blue and the current density in red. In the left panel there is a clear difference between the two sets of lines, and in the right panel the two sets of lines closely coincide, indicating that a force-free solution is found. Some disagreement is observed between the two sets of lines for longer field lines and is explained in Section 4.4.3.

The right panel of Figure 4.4 shows $\theta_{\rm max}$ as a function of iteration number. After the first iteration the maximum angle between $\mathbf{J}$ and $\mathbf{B}$ is approximately 20 degrees, and $\theta_{\rm max}$ decreases approximately exponentially with iteration, to a final value of order 10^{-9} degrees.

4.5 Discussion and Conclusion

We present an implementation of the Grad-Rubin method (Grad and Rubin, 1958) for solving the force-free boundary value problem in spherical polar geometry with the aim of modelling the solar coronal magnetic field. The method is applicable to either the entire corona or a wedge with restricted angular extent.

We apply our code to two test cases with analytic boundary conditions, representing a current-carrying bipole, to demonstrate the convergence of the Grad-Rubin iteration and the self-consistency of the final numerical solution. For the first case we compute a solution in a domain which encompasses the entire corona, and in the second we compute a solution in a spherical wedge. We find that in both cases the Grad-Rubin iteration converges, and the resulting solution is force free to a very good approximation, by which we mean that the angle between $\mathbf{J}$ and $\mathbf{B}$ is small.

The bipolar test case we consider is simple, but serves to illustrate the basic correctness of the method. We are unable to identify a suitable exact analytic equilibria with which to test the code. The Low and

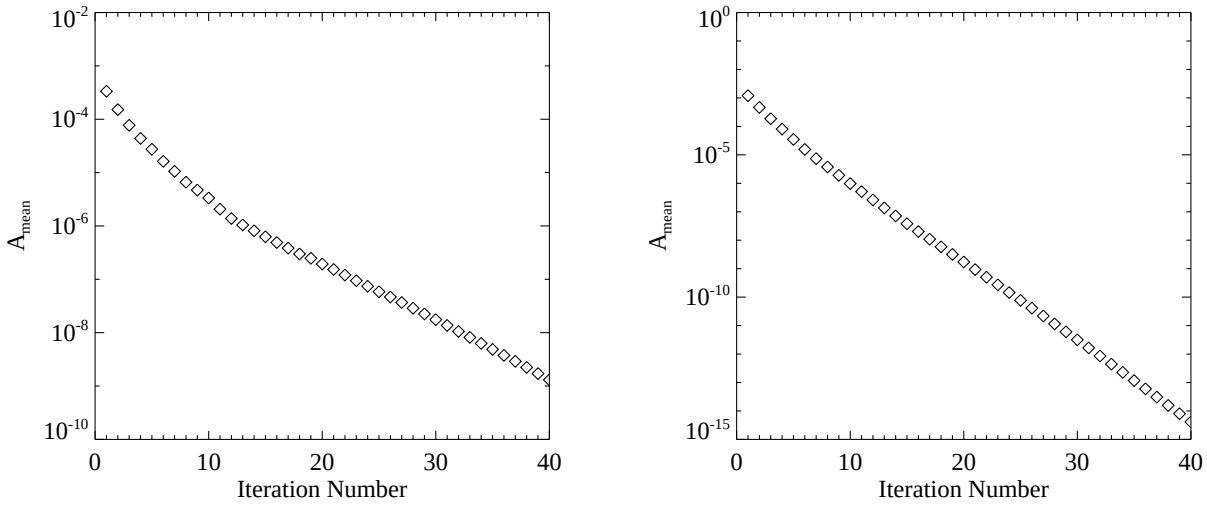

Figure 4.2: The average absolute change in the field, A_{mean}, as a function of iteration number for the first test case (left panel) and the second test case (right panel). The vertical scale is logarithmic.

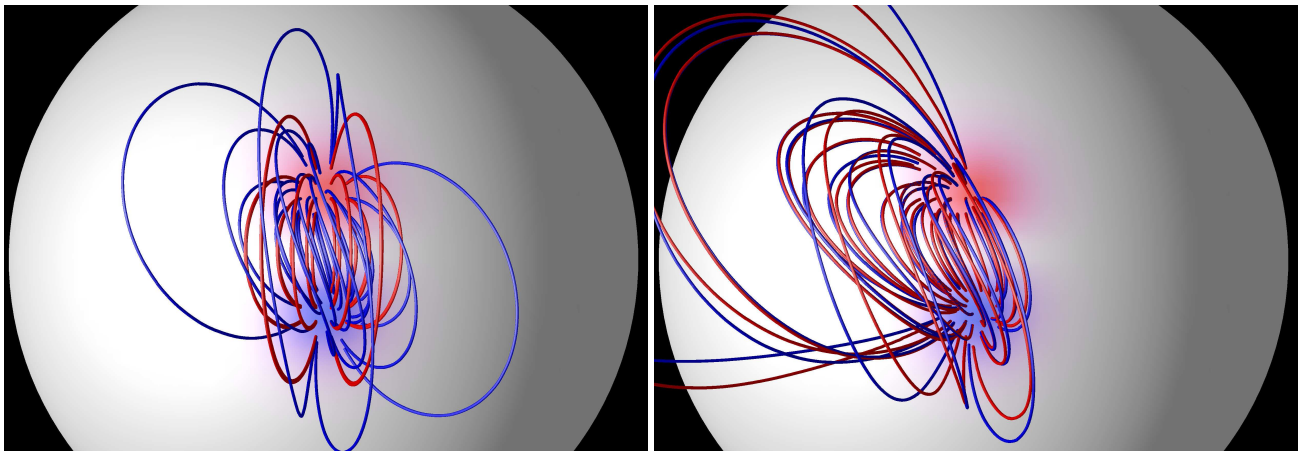

Figure 4.3: Field lines (blue) and streamlines of current density (red) for test case one. The left panel is after the first Grad-Rubin iteration. The right is after 40 Grad-Rubin iterations. In the left panel there is a clear difference between the two sets of lines, and in the right the two sets of lines coincide, indicating that a force-free solution has been found. The discrepancy between the two sets of lines is due to the interpolation of field values between grid points necessary to draw the lines (see the discussion in Section 4.4.3).

Lou (1990) field has often been used for testing force-free codes (Amari, Boulmezaoud, and Mikic, 1999; Wiegelmann, 2007), but it proves difficult to reproduce this solution without imposing analytic boundary conditions on an outer shell located at a finite radius from the photosphere. Using the asymptotic boundary condition defined by Equation (4.4), requires a very large domain to encompass all the significant currents for the Low and Lou (1990) problem. Hence it is difficult to calculate accurate solutions without resorting to the use of exact boundary conditions at a finite outer shell. The lack of an exact analytic test case means that we cannot determine how the numerical error scales as a function of grid resolution. We also note that our test case has smooth boundary conditions. In practice, we expect observational data to contain significant gradients, in particular due to noise which is present in the data. The effect of Gibbs phenomenon produced by the spectral method applied to these large gradients has not yet been investigated.

We note that the code takes 1.6 hours to run for the test case in the spherical wedge, for a grid with 64^3 points. By comparison the calculation in the global domain takes 15 minutes for a $128 \times 64 \times 128$ grid. The difference in speed occurs because the spherical harmonics must be summed to large orders when $\Delta\phi$

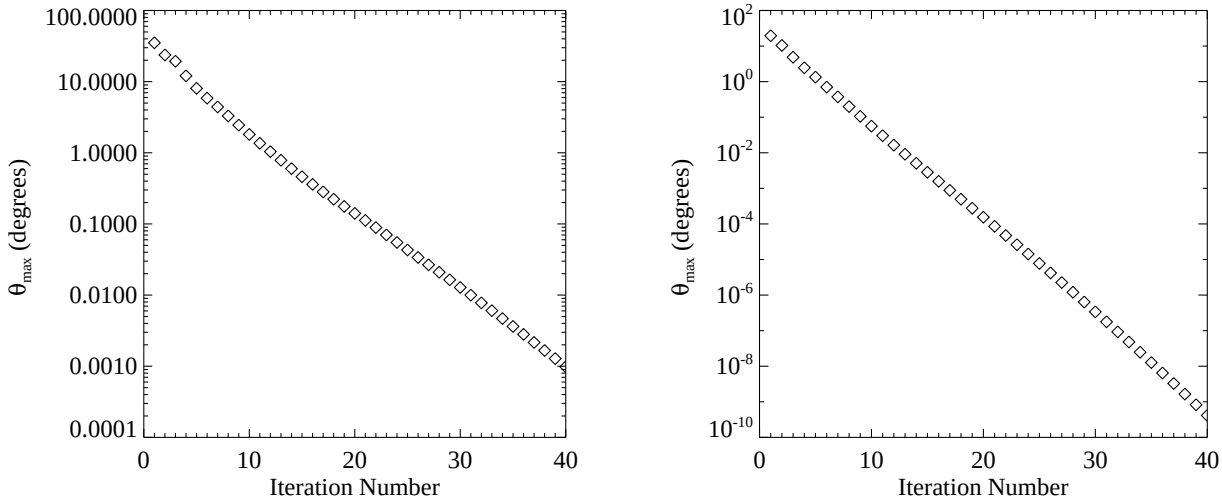

Figure 4.4: The maximum angle between $\mathbf{J}$ and $\mathbf{B}$ over the solution domain as a function of iteration number. The left panel shows $\theta_{\max}$ for the first test case in $\Omega_{\rm global}$, and the right panel shows $\theta_{\max}$ for the second test case in $\Omega_{\rm wedge}$. The vertical scale is logarithmic.

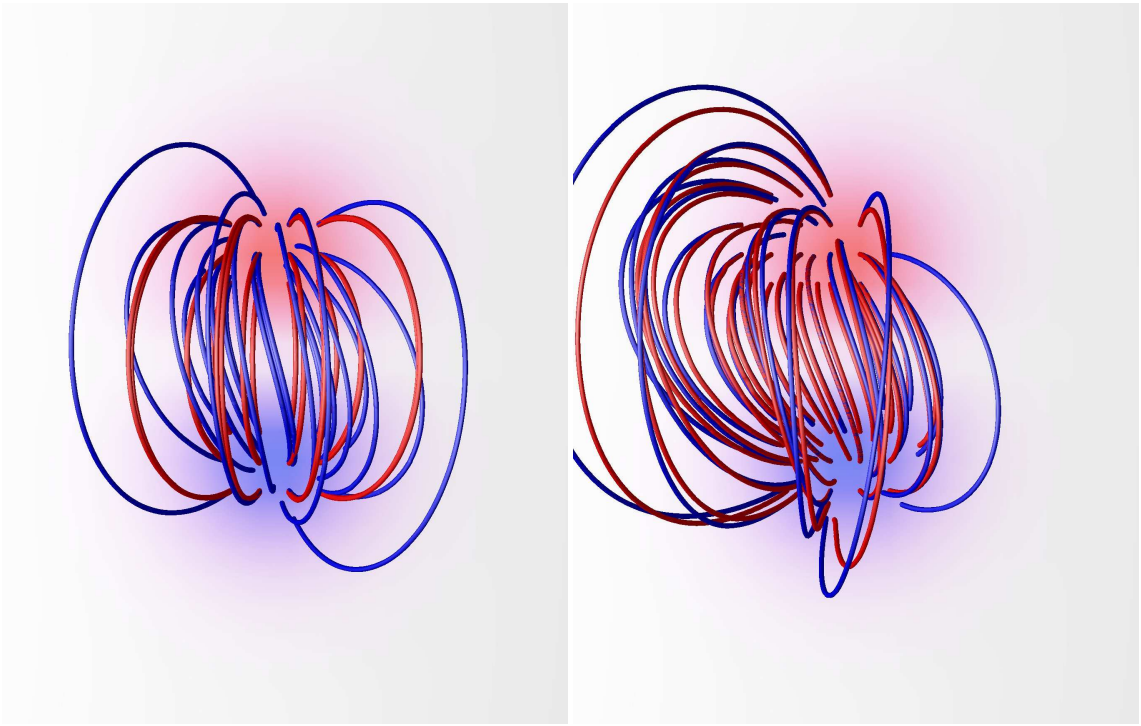

Figure 4.5: Field lines (blue) and streamlines of current density (red) for test case two. The left panel is after the first Grad-Rubin iteration. The right is after 40 Grad-Rubin iterations. In the left panel there is a clear difference between the two sets of lines, and in the right the two sets of lines coincide, indicating that a force-free solution has been found. The discrepancy between the two sets of lines is due to the interpolation of field values between grid points necessary to draw the lines (see the discussion in Section 4.4.3).

is small. In the first case $L = 64$ and in the second case $L = 567$. In practice it may not be necessary to use an L value of a given size for all values of r. We expect that as the field becomes smoother with increasing r higher order terms may be ignored and a reduction in L as a function of r may increase the speed of the code. Also, we expect that it may be possible to increase the speed of the code by improving details of the technique used for the calculation of the non-potential field. These improvements will be implemented in future work.

As mentioned in Section 4.3.1, Tóth, van der Holst, and Huang (2011) report the non-convergence of the spherical harmonics spectral series for large L, for the calculation of potential field models. The grid used by Tóth, van der Holst, and Huang (2011) is uniform in $\cos\theta$. However, near the poles, the associated Legendre polynomials are rapidly varying functions of $\cos\theta$, and the rapid variations are not accurately represented on the given grid. This results in the non-convergence of the series. For our calculations in $\Omega_{\rm wedge}$, we use a grid uniform in θ. Tóth, van der Holst, and Huang (2011) report that such a grid does not cause convergence problems. Furthermore, the region considered in Section 4.4.4 is sufficiently isolated from the poles that convergence problems are unlikely to occur regardless of the grid used. When considering larger regions which cannot be isolated from the poles, or for calculations in $\Omega_{\rm global}$ we use a Gauss-Legendre grid which is dense at the poles and accurately represents the rapid variations in the associated Legendre polynomials.

Other developments to the code are also planned. At present, the code uses a uniform grid in r, but this could be changed to a nonuniform grid. A nonuniform grid should be more efficient because the grid can be chosen to be dense close to the photosphere where the magnetic field is structured on small scales, and sparse far from the photosphere where the field is smooth. At present the method assumes the asymptotic boundary condition Equation (4.4) but this could be changed to accommodate boundary conditions at an outer "source surface" analogous to the potential source-surface model. Finally, the method presently only uses α_0 over a single polarity, which is likely to be problematic when using observational data because of the inconsistency of the data with the force-free model (Schrijver *et al.*, 2008). In future work we will modify our method to implement the self-consistency procedure of Wheatland and Régnier (2009).

The method and code outlined in this chapter are designed for application to solar data, but we have not yet attempted this. In future work we will test the code on vector magnetogram data derived from observations by the *Helioseismic and Magnetic Imager* aboard the *Solar Dynamics Observatory* (SDO/HMI). The SDO/HMI instrument provides data for the whole solar disk, which demands spherical modelling. We hope to be able to develop the code presented here into a practical tool for modelling of the coronal magnetic field from SDO/HMI data, and for application to other, future data sets.

4.6 Appendix

In this appendix we outline a parallel method for evaluating the sums in Equations (4.8)-(4.10). The method of summing the spectral series is important because it determines the speed of the computation. Also, a high resolution grid requires a large order L, in which case the memory required to compute the spectral solution becomes large (depending of the implementation). In the following we present a method for summing the series which is fast and which uses memory efficiently. The procedure is described for the B_r component of the potential field. A similar approach is used for the other components of the potential field, and for the non-potential field.

4.6.1 Parallel Summation of the Spectral Series

The following procedure for computing B_r follows a prescription in Press *et al.* (2007). Here we briefly outline the method and describe a parallel implementation.

The spectral series for B_r can be written as

$$B_r = \sum_{m=-L}^{L} g_m(r,\theta)e^{im\phi}, \tag{4.41}$$

where the auxiliary function $g_m(r,\theta)$ is defined as

$$g_m(r,\theta) = \sum_{l=|m|}^{L} a_{lm} \left(\frac{R_\odot}{r}\right)^{l+2} \tilde{P}_l^m(\cos\theta), \tag{4.42}$$

and where the spherical harmonics Y_{lm} are written as a product of a normalised-associated Legendre polynomial $\tilde{P}_l^m(x)$ and the complex exponential. In our method we first compute the auxiliary function using Equation (4.42), and then determine B_r using Equation (4.41).

This procedure can be implemented in parallel by partitioning the sum in Equation (4.41) into N partial sums which are computed independently. We define the partial sum

$$F_n = \sum_{m=m_n}^{m_{n+1}} g_m(r,\theta)e^{im\phi} + \sum_{m=-m_{n+1}}^{-m_n} g_m(r,\theta)e^{im\phi}, \tag{4.43}$$

where

$$m_n = nL/N. \tag{4.44}$$

The complete solution is then

$$B_r = \sum_{n=0}^{N-1} F_n. \tag{4.45}$$

For the special case $m = 0$ it is necessary to make the replacement $g_{\pm m}(\theta,\phi) \rightarrow g_{\pm m}(\theta,\phi)/2$ in Equation (4.43) to prevent over counting. Each F_n can be computed independently, allowing trivial parallelism. Most high performance computer clusters consist of a series of nodes, with each node containing several processors with shared a memory space. Our code distributes the computation of F_n among such nodes using the Message Passing Interface (MPI) (Snir *et al.*, 1998). The computation of F_n at each node is parallelized across the processors on the node using OpenMP (Chandra *et al.*, 1990).

4.6.2 Memory Requirements

It is important to consider the memory required to store $g_m(r,\theta)$ as an array. Since the integrand in Equation (4.11) is real, the coefficients with $m < 0$ contain the same information as those with $m > 0$ (Press *et al.*, 2007). Therefore, it is necessary only to store coefficients with $m \geq 0$, and there are $(L+1)L/2$ such coefficients. Therefore an array storing $g_m(r,\theta)$ has $L(L+1)N_rN_\theta/2$ elements for a grid of size $N_r \times N_\theta \times N_\phi$. The associated memory use may prove problematic for $L \sim 1000$. A grid of size $N_r = 128$, $N_\theta = 256$, and $N_\phi = 512$ requires $\approx 100\,\mathrm{Mb}$ to store B_r using double precision floating point numbers, and $\approx 1\,\mathrm{Gb}$ to store $g_m(r,\theta)$. The memory requirements for $g_m(r,\theta)$ can quickly become larger than a few gigabytes, a typical size for total memory on current desktop computer hardware.

The partial summation method reduces the memory requirements because the array g_m is split among the nodes. If the series is split into N partial sums, then the memory requirement for each node is $\sim 1/N$ of that needed to store the entire array. The partial summation method can also be used to conserve memory with only a single node. In this case each partial sum is computed sequentially. This way only part of the spectrum g_m is computed for each partial summation. Again, this method reduces the memory requirements by a factor $\sim 1/N$ compared with a single serial summation.

Chapter 5

Vector-Spherical Harmonic Solution to Ampere's Law around a Sphere

5.1 Introduction

In Chapter 4 we outline an implementation of the Grad-Rubin method in spherical polar coordinates. One of the steps in the Grad-Rubin methods requires the solution of Ampere's law, and in Section 4.3.3 we quoted (without a derivation) a solution to Ampere's law based on a vector-spherical harmonic expansion. In this chapter we derive the solution in 4.3.3.

This chapter is structured as follows. In Section 5.2 we formulate the boundary value problem. In Section 5.3 we present the solution of Laplace's equation for the potential component of the magnetic field. In section 5.4 we present the solution of Poisson's equation for the non-potential component of the magnetic field.

5.2 Formulation of Boundary Value Problems

A magnetostatic field is a static magnetic field produced by the steady flow of electric current. A magnetic field $\mathbf{B}$ is related to the electric current density $\mathbf{J}$ by Ampere's law

$$\nabla \times \mathbf{B} = \mu_0 \mathbf{J}, \tag{5.1}$$

and it also satisfies the divergence-free condition

$$\nabla \cdot \mathbf{B} = 0 \tag{5.2}$$

(Jackson, 1998). It is assumed that $\mathbf{J}$ represents a steady current, which implies

$$\nabla \cdot \mathbf{J} = 0. \tag{5.3}$$

In general solving Equations (5.1) and (5.2) takes the form of a boundary value problem. The formulation of the general magnetostatic boundary value problem is given by Jackson (1998).

When there are no boundaries present in the problem, the solution to Equations (5.1) and (5.2) is given by the Biot-Savart law (Jackson, 1998). However when boundaries are present the problem is more involved. One way to simplify the problem is to write $\mathbf{B}$ as the sum

$$\mathbf{B} = \mathbf{B}_0 + \mathbf{B}_c, \tag{5.4}$$

where $\mathbf{B}_0$ is a current-free (potential) magnetic field which satisfies the boundary conditions, and $\mathbf{B}_c$ is a non-potential magnetic field which satisfies homogeneous boundary conditions. The potential field can be expressed as

$$\mathbf{B}_0 = \nabla u, \tag{5.5}$$

where the scalar potential, u, is a solution of Laplace's equation

$$\nabla^2 u = 0. \tag{5.6}$$

Splitting the field into potential and non-potential components has two advantages. First, imposing more general boundary conditions on the scalar potential is easier than imposing boundary conditions on the magnetic field because of the reduced number of dependent variables (*i.e.* one scalar field u compared to three scalar fields for $\mathbf{B}$). Second, the comparatively more difficult problem of finding $\mathbf{B}_c$ is simplified because homogeneous boundary conditions are, in general, simpler to impose than non-homogeneous boundary conditions.

The non-potential component can be expressed as a vector potential $\mathbf{A}$, defined by

$$\mathbf{B}_c = \nabla \times \mathbf{A}. \tag{5.7}$$

In the Coulomb gauge,

$$\nabla \cdot \mathbf{A} = 0, \tag{5.8}$$

and the vector potential satisfies the vector Poisson equation *i.e.*

$$\nabla^2 \mathbf{A} = -\mu_0 \mathbf{J}. \tag{5.9}$$

The boundary conditions on $\mathbf{A}$ are determined by the requirement that $\mathbf{B}_c$ is homogeneous on the boundary, *i.e.*

$$\mathbf{B}_c \cdot \hat{\boldsymbol{r}}|_{r=R_\odot} = 0. \tag{5.10}$$

Boundary Value Problem

We consider the magnetic field in the region external to a sphere of radius $R_\odot$. This is the boundary value problem from Section 4.2.1, and we restate it here. The domain is

$$\Omega_{\text{global}} = \{(r, \theta, \phi) | r \in [R_\odot, \infty), \phi \in [0, 2\pi), \theta \in [0, \pi]\}. \tag{5.11}$$

The boundary conditions on the magnetic field are

$$\mathbf{B} \cdot \hat{\boldsymbol{r}}|_{r=R_\odot} = B_n(\theta, \phi), \tag{5.12}$$

and

$$\lim_{r \to \infty} \mathbf{B} = 0. \tag{5.13}$$

These boundary conditions can be used to derive boundary conditions for the scalar and vector potentials. The boundary conditions on u implied by Equations (5.12) and (5.13) are

$$\left.\frac{\partial u}{\partial r}\right|_{r=R_\odot} = B_n, \tag{5.14}$$

and

$$\lim_{r \to \infty} u = c, \tag{5.15}$$

where c is an arbitrary constant, which for convenience we set to zero. The non-potential field, $\mathbf{B}_c$, is required to satisfy the homogeneous boundary condition

$$\mathbf{B}_c \cdot \hat{\boldsymbol{r}}|_{r=R_\odot} = 0. \tag{5.16}$$

The boundary conditions on the vector potential which imply Equations (5.10) and (5.13) are

$$\mathbf{A} \times \hat{\mathbf{n}} = 0, \tag{5.17}$$

and

$$\lim_{r \to \infty} \mathbf{A} = 0. \tag{5.18}$$

5.3 Derivation of the Potential Component

In this section we determine the potential field component for the boundary value problem outlined in Section 5.2 using a spherical harmonic expansion. The solution to Laplace's equation in terms of spherical harmonics is well known (*e.g.* Morse and Feshbach 1953; Jackson 1998), but is included here for completeness.

5.3.1 General Solution to Laplace's Equation

Laplace's equation in spherical polar coordinates is

$$\frac{\partial^2 u}{\partial r^2} + \frac{2}{r}\frac{\partial u}{\partial r} + \frac{1}{r^2}\frac{\partial^2 u}{\partial \theta^2} + \frac{\cot\theta}{r^2}\frac{\partial u}{\partial \theta} + \frac{1}{r^2 \sin^2\theta}\frac{\partial^2 u}{\partial \phi^2} = 0. \tag{5.19}$$

The scalar potential can be expanded as series of the form

$$u(r,\theta,\phi) = \sum_{l=0}^{\infty}\sum_{m=-l}^{l} c_{lm}(r) Y_{lm}(\theta,\phi), \tag{5.20}$$

where Y_{lm} is the spherical harmonic of order l and degree m, and c_{lm} are spectral coefficients. An expression for the spectral coefficients can be derived by substituting Equation (5.20) into Laplace's equation. This gives

$$r^2 c''_{lm}(r) + 2r c'_{lm}(r) - l(l+1)c_{lm}(r) = 0, \tag{5.21}$$

where the prime denotes differentiation with respect to r. This equation can be solved by substitution of the ansatz

$$c_{lm}(r) = r^{\lambda}, \tag{5.22}$$

where λ is a parameter to be determined. This method gives the two linear independent solutions

$$c_{lm}(r) = r^{l} \tag{5.23}$$

and

$$c_{lm}(r) = r^{-(l+1)}. \tag{5.24}$$

The general solution to Laplace's equation is therefore

$$u(r,\theta,\phi) = \sum_{l=0}^{\infty}\sum_{m=-l}^{l} [C_{lm} r^{l} + D_{lm} r^{-(l+1)}] Y_{lm}(\theta,\phi), \tag{5.25}$$

where C_{lm} and D_{lm} are constants to be determined by the boundary conditions.

5.3.2 Solution to the Boundary Value Problem for the Potential Field

We begin with the general solution found in Section 5.3.1 and apply the specific boundary conditions to determine the coefficients C_{lm} and D_{lm}. The condition that u remains finite as $r \to \infty$ implies $C_{lm} = 0$. The coefficient D_{lm} is determined by the boundary condition at $r = R_{\odot}$. Applying this boundary condition gives

$$D_{lm} = -\frac{R_{\odot}^{l+2}}{l+1}\int_0^{2\pi}\int_0^{\pi} B_n(\theta,\phi) Y^*_{lm}(\theta,\phi)\sin\phi \, d\theta \, d\phi \tag{5.26}$$

for the second set of coefficients. Therefore the solution is

$$u(r,\theta,\phi) = -\sum_{l=0}^{\infty}\sum_{m=-l}^{l} \frac{a_{lm}}{l+1} r \left(\frac{R_{\odot}}{r}\right)^{l+2} Y_{lm}(\theta,\phi), \tag{5.27}$$

where

$$a_{lm} = \int_0^{2\pi} \int_0^{\pi} B_n(\theta, \phi) Y_{lm}^*(\theta, \phi) \sin\theta d\theta d\phi. \tag{5.28}$$

The limits of the integral cover the entire range of azimuthal and polar angles.

The gradient of the potential yields the magnetic field vector. The components of the magnetic field are

$$B_r = \sum_{l=0}^{\infty} \sum_{m=-l}^{l} a_{lm} \left(\frac{R_\odot}{r} \right)^{l+2} Y_{lm}(\theta, \phi), \tag{5.29}$$

$$B_\theta = -\sum_{l=0}^{\infty} \sum_{m=-l}^{l} \frac{a_{lm}}{l+1} \left(\frac{R_\odot}{r} \right)^{l+2} \frac{\partial Y_{lm}}{\partial \theta}, \tag{5.30}$$

and

$$B_\theta = -\sum_{l=0}^{\infty} \sum_{m=-l}^{l} \frac{a_{lm}}{l+1} \left(\frac{R_\odot}{r} \right)^{l+2} \frac{imY_{lm}}{\sin\theta}. \tag{5.31}$$

The expression for the θ derivative of a spherical harmonic is given in Appendix A.

5.4 Derivation of the Non-Potential Component

The vector potential is a solution of the vector Poisson equation:

$$\nabla^2 \mathbf{A} = -\mu_0 \mathbf{J}. \tag{5.32}$$

Equation (5.32) has an involved form in spherical polar coordinates, which is simplified by expanding $\mathbf{A}$ in terms of the eigenfunctions of the vector Laplace operator. This approach reduces the partial differential equations for $\mathbf{A}$ to a set of ordinary differential equations, which can be solved analytically.

The eigenfunctions of the vector Laplacian in spherical polar coordinates are vector valued functions called the vector-spherical harmonics (Morse and Feshbach, 1953; Dennis and Quartapelle, 1985). There are several ways to define the vector spherical harmonics, and here the convention of Morse and Feshbach (1953) and the notation of Dennis and Quartapelle (1985) is followed:

$$\mathbf{Y}_{lm}(\theta, \phi) = Y_{lm}(\theta, \phi)\hat{\boldsymbol{r}}, \tag{5.33}$$

$$\boldsymbol{\Psi}_{lm}(\theta, \phi) = \frac{r\nabla Y_{lm}(\theta, \phi)}{\sqrt{l(l+1)}}, \tag{5.34}$$

and

$$\boldsymbol{\Phi}(\theta, \phi) = \frac{\mathbf{r} \times \nabla Y_{lm}(\theta, \phi)}{\sqrt{l(l+1)}}. \tag{5.35}$$

Note that despite the presence of r in Equations (5.33)-(5.35), the vector spherical harmonics are independent of r since $\nabla Y_{lm}(\theta, \phi) \propto 1/r$.

Some basic properties of the vector spherical harmonics are summarised in Appendix B. These functions form a complete orthonormal basis, meaning any solution to Equation (5.32) can written as a series of the form

$$\mathbf{A}(r, \theta, \phi) = \sum_{l=0}^{\infty} \sum_{m=-l}^{l} A_{lm}^{(1)}(r)\mathbf{Y}_{lm} + A_{lm}^{(2)}(r)\boldsymbol{\Psi}_{lm} + A_{lm}^{(3)}(r)\boldsymbol{\Phi}_{lm}, \tag{5.36}$$

where $A_{lm}^{(1)}$, $A_{lm}^{(2)}$, and $A_{lm}^{(3)}$ are referred to as spectral coefficients. When expressed in this way the vector Poisson's equation is reduced to a set of coupled second-order equations for the spectral coefficients (Dennis and Quartapelle, 1985). The equations are

$$\frac{d^2A_{lm}^{(1)}}{dr^2} + \frac{2}{r}\frac{dA_{lm}^{(1)}}{dr} - \frac{l(l+1)+2}{r^2}A_{lm}^{(1)} + \frac{2\sqrt{l(l+1)}}{r^2}A_{lm}^{(2)} = -\mu_0 J_{lm}^{(1)}(r), \tag{5.37}$$

$$\frac{d^2A_{lm}^{(2)}}{dr^2} + \frac{2}{r}\frac{dA_{lm}^{(2)}}{dr} - \frac{l(l+1)+2}{r^2}A_{lm}^{(2)} + \frac{2\sqrt{l(l+1)}}{r^2}A_{lm}^{(1)} = -\mu_0 J_{lm}^{(2)}(r), \tag{5.38}$$

and

$$\frac{d^2A_{lm}^{(3)}}{dr^2} + \frac{2}{r}\frac{dA_{lm}^{(3)}}{dr} - \frac{l(l+1)}{r^2}A_{lm}^{(3)} = -\mu_0 J_{lm}^{(3)}(r), \tag{5.39}$$

where

$$J_{lm}^{(1)}(r) = \int \mathbf{J}\cdot\mathbf{Y}_{lm}^{*}d\Omega, \tag{5.40}$$

$$J_{lm}^{(2)}(r) = \int \mathbf{J}\cdot\mathbf{\Psi}_{lm}^{*}d\Omega, \tag{5.41}$$

and

$$J_{lm}^{(3)}(r) = \int \mathbf{J}\cdot\mathbf{\Phi}_{lm}^{*}d\Omega. \tag{5.42}$$

5.4.1 General Solution for $A_{lm}^{(3)}$

Equation (5.39) is independent of the other equations and may be solved for the $A_{lm}^{(3)}$ coefficients. The solution requires two steps: (i) finding the general solution to the homogeneous problem, and (ii) finding the particular solution to the inhomogeneous problem using the method of variation of parameters (Zwillinger, 1992).

The homogeneous equation can be solved using the ansatz

$$A_{lm}^{(3)}(r) = r^{\lambda}, \tag{5.43}$$

where λ is a parameter to be determined. The two linearly independent solutions are

$$A_{lm}^{(3)}(r) = r^{l} \tag{5.44}$$

and

$$A_{lm}^{(3)}(r) = r^{-l-1}. \tag{5.45}$$

The general solution $A_{lm}^{(3)}$ is therefore

$$A_{lm}^{(3)}(r) = C_{lm}r^{l} + D_{lm}r^{-l-1}, \tag{5.46}$$

where C_{lm} and D_{lm} are constants which are determined by the boundary conditions.

The particular solution to the inhomogeneous problem $A_{lm}^{(3)}$ can be computed from the general solution (and its derivatives) using the method of variation of parameters (Zwillinger, 1992). Using this method, the particular solution is

$$A_{lm}^{(3)}(r) = \frac{\mu_0 r^{-l-1}}{2l+1}\int_{R_\odot}^{r} s^{l+2}J_{lm}^{(3)}(s)ds - \frac{\mu_0 r^{l}}{2l+1}\int_{R_\odot}^{r} s^{1-l}J_{lm}^{(3)}(s)ds. \tag{5.47}$$

The complete solution is the sum of the general and particular solutions:

$$A_{lm}^{(3)}(r) = C_{lm}r^{l} + D_{lm}r^{-l-1} + \frac{\mu_0 r^{-l-1}}{2l+1}\int_{R_\odot}^{r} s^{l+2}J_{lm}^{(3)}(s)ds - \frac{\mu_0 r^{l}}{2l+1}\int_{R_\odot}^{r} s^{1-l}J_{lm}^{(3)}(s)ds. \tag{5.48}$$

5.4.2 General Solution for $A_{lm}^{(1)}$

The equations for $A_{lm}^{(1)}$ and $A_{lm}^{(2)}$ are coupled, but they can be uncoupled using the Coulomb gauge condition $\nabla \cdot \mathbf{A} = 0$. Applying the divergence formula for vector-spherical harmonics (see Appendix B), to the Coulomb gauge condition gives

$$\frac{dA_{lm}^{(1)}}{dr} + \frac{2}{r}A_{lm}^{(1)} - \frac{\sqrt{l(l+1)}}{r}A_{lm}^{(2)} = 0. \tag{5.49}$$

Equation (5.49) can be used to eliminate the $A_{lm}^{(2)}$ term in Equation (5.37) to give the uncoupled equation

$$\frac{d^2A_{lm}^{(1)}}{dr^2} + \frac{4}{r}\frac{dA_{lm}^{(1)}}{dr} + \frac{2 - l(l+1)}{r^2}A_{lm}^{(1)} = -J_{lm}^{(1)}(r). \tag{5.50}$$

Equation (5.50) can be solved in the same way as Equation (5.39). The solutions to the homogeneous equation are

$$A_{lm}^{(1)}(r) = r^{-1+l}, \tag{5.51}$$

and

$$A_{lm}^{(1)}(r) = r^{-2-l}. \tag{5.52}$$

The general solution to the homogeneous problem is therefore

$$A_{lm}^{(1)}(r) = C_{lm}r^{-1+l} + D_{lm}r^{-2-l}, \tag{5.53}$$

where C_{lm} and D_{lm} are constants determined by the choice of boundary conditions. The particular solution found by variation of parameters is

$$A_{lm}^{(1)}(r) = \frac{r^{-2-l}}{2l+1}\int_{R_\odot}^{r} s^{l+3}J_{lm}^{(1)}(s)ds - \frac{r^{-1+l}}{2l+1}\int_{R_\odot}^{r} s^{2-l}J_{lm}^{(1)}(s)ds. \tag{5.54}$$

5.5 Solution to the Boundary Value Problem for the Spectral Coefficients of the Non-Potential Field

5.5.1 Derivation of $A_{lm}^{(3)}$

The coefficients can be calculated from the boundary conditions given in Section 5.2, *i.e.*

$$\mathbf{A} \times \hat{\boldsymbol{r}}|_{r=R_\odot} = 0, \tag{5.55}$$

and

$$\lim_{r\to\infty} \mathbf{A} = 0. \tag{5.56}$$

Since $\hat{\boldsymbol{r}} \cdot \boldsymbol{\Phi}_{lm}(r) = 0$, Equation (5.55) implies

$$A_{lm}^{(3)} = 0\Big|_{r=R_\odot}, \tag{5.57}$$

and Equation (5.56) implies

$$\lim_{r\to\infty} A_{lm}^{(3)} = 0. \tag{5.58}$$

Imposing the first boundary condition (Equation (5.57)) on Equation (5.48) results in the relationship

$$D_{lm} = -C_{lm}R_\odot^{2l+1}, \tag{5.59}$$

and imposing the second boundary condition (Equation (5.58)) on Equation (5.48) gives

$$C_{lm} = \frac{\mu_0}{2l+1} \int_{R_\odot}^{\infty} s^{1-l} J_{lm}^{(3)}(s) ds. \tag{5.60}$$

For C_{lm} to be finite, $J_{lm}^{(3)}(r)$ must decrease with r at least as rapidly as $1/r^2$.

The complete solution is obtained by adding up the general and particular solutions:

$$A_{lm}^{(3)}(r) = -R_\odot^l \left(\frac{R_\odot}{r}\right)^{l+1} I_0 + I_1(r) + I_2(r), \tag{5.61}$$

where

$$I_0 = \frac{\mu_0}{2l+1} \int_{R_\odot}^{\infty} s^{1-l} J_{lm}^{(3)}(s) ds \tag{5.62}$$

$$I_1(r) = \frac{\mu_0}{2l+1} \int_{R_\odot}^{r} s \left(\frac{s}{r}\right)^{l+1} J_{lm}^{(3)}(s) ds, \tag{5.63}$$

and

$$I_2(r) = \frac{\mu_0}{2l+1} \int_{r}^{\infty} s \left(\frac{r}{s}\right)^{l} J_{lm}^{(3)}(s) ds. \tag{5.64}$$

The integrals I_1, I_2 and I_3 are written in such as way as to avoid overflow when implemented numerically. In each case the term raised to the power of l is less than one, so for large l numerical underflow may occur but numerical overflow will never occur.

5.5.2 Derivation of $A_{lm}^{(1)}$

The spectral coefficients for $A_{lm}^{(1)}$ can be computed from the general solution by imposing the boundary conditions given in Section 5.2, *i.e.*

$$\mathbf{A} \times \hat{\boldsymbol{r}}|_{r=R_\odot} = 0, \tag{5.65}$$

and

$$\lim_{r\to\infty} \mathbf{A} = 0. \tag{5.66}$$

The second of these conditions implies the boundary condition

$$\lim_{r\to\infty} A_{lm}^{(1)} = 0. \tag{5.67}$$

However, the boundary condition given by Equation (5.65) does not constrain $A_{lm}^{(1)}$ since $\mathbf{Y}_{lm}(r) \times \hat{\boldsymbol{r}} = 0$ identically. Instead, a second boundary condition must be derived from the Coulomb gauge condition and the boundary conditions on $A_{lm}^{(2)}$. The gauge condition implies the relationship

$$\frac{dA_{lm}^{(1)}}{dr} + \frac{2}{r} A_{lm}^{(1)} - \frac{\sqrt{l(l+1)}}{r} A_{lm}^{(2)} = 0, \tag{5.68}$$

and we can use this and the boundary conditions on $A_{lm}^{(2)}$ implied by Equation (5.65) to derive boundary condition on $A_{lm}^{(1)}$. Since $\boldsymbol{\Psi}_{lm}(r) \times \hat{\boldsymbol{r}} \neq 0$, we require $A_{lm}^{(2)} = 0$ on the the surface $r = R_\odot$ in order to satisfy Equation (5.65), hence Equation (5.68) implies that the second boundary condition on $A_{lm}^{(1)}$ is

$$\left.\frac{dA_{lm}^{(1)}}{dr} + \frac{2}{r} A_{lm}^{(1)}\right|_{r=R_\odot} = 0. \tag{5.69}$$

Applying the boundary conditions given by Equations (5.67) and (5.69) to the general solution found in Section 5.4.2 gives

$$C_{lm} = \frac{1}{2l+1} \int_{R_\odot}^{\infty} s^{2-l} J_{lm}^{(1)}(s) ds, \tag{5.70}$$

and

$$D_{lm} = \frac{l+1}{l(2l+1)} R_{\odot}^{2l+1} \int_{R_{\odot}}^{\infty} s^{2-l} J_{lm}^{(1)}(s) ds. \tag{5.71}$$

The complete solution for the $A_{lm}^{(1)}$ component is

$$A_{lm}^{(1)} = \frac{R_{\odot}^{2l+1}(l+1) I_3}{l r^{2+l}} + I_4(r) + I_5(r) \tag{5.72}$$

where

$$I_3 = \frac{1}{2l+1} \int_{R_{\odot}}^{\infty} s^{2-l} J_{lm}^{(1)}(s) ds, \tag{5.73}$$

$$I_4(r) = \frac{1}{2l+1} \int_{R_{\odot}}^{r} s \left(\frac{s}{r}\right)^{l+2} J_{lm}^{(1)}(s) ds, \tag{5.74}$$

and

$$I_5(r) = \frac{1}{2l+1} \int_{r}^{\infty} s \left(\frac{r}{s}\right)^{l-1} J_{lm}^{(1)}(s) ds. \tag{5.75}$$

5.5.3 Derivation of $A_{lm}^{(2)}$

The coefficients $A_{lm}^{(2)}$ can be computed from the coefficients $A_{lm}^{(1)}$ using Equation (5.49). Therefore it is not necessary to solve Equation (5.38) directly. The coefficients are

$$A_{lm}^{(2)} = \frac{(l+1) R_{\odot}^{2l+1}}{\sqrt{l(l+1)}} \frac{I_3}{r^{2+l}} + \frac{l}{\sqrt{l(l+1)}} I_4(r) - \frac{1+l}{\sqrt{l(l+1)}} I_5(r), \tag{5.76}$$

where I_3, $I_4(r)$ and $I_5(r)$ are the same as in Section 5.4.2.

5.5.4 Spectral Coefficients for the Magnetic Field

The spectral coefficients for the magnetic field $\mathbf{B}_{lm}$ can be computed from $\mathbf{A}_{lm}$ using the definition of the vector potential $\nabla \times \mathbf{A} = \mathbf{B}$. Using the vector spherical harmonic relations for the curl given in Appendix B it is straightforward to show that

$$B_{lm}^{(1)} = \sqrt{l(l+1)} A_{lm}^{(3)} / r, \tag{5.77}$$

and

$$B_{lm}^{(2)} = \frac{dA_{lm}^{(3)}}{dr} + \frac{A_{lm}^{(3)}}{r}. \tag{5.78}$$

The expression for $B_{lm}^{(3)}$ found from $\nabla \times \mathbf{A} = \mathbf{B}$ is

$$B_{lm}^{(3)} = \sqrt{l(l+1)} A_{lm}^{(1)} - \frac{dA_{lm}^{(2)}}{dr} + \frac{A_{lm}^{(2)}}{r}. \tag{5.79}$$

This can be simplified using the equations $\nabla \cdot \mathbf{A} = 0$, and $\nabla^2 \mathbf{A} = -\mu_0 \mathbf{J}$. The simplified expression is

$$B_{lm}^{(3)} = \frac{r J_{lm}^{(1)}}{\sqrt{l(l+1)}}. \tag{5.80}$$

Equation (5.80) can also be obtained by applying the vector-spherical harmonic curl formula directly to Ampere's law ($\nabla \times \mathbf{B} = \mu_0 \mathbf{J}$).

The explicit form for the spectral coefficients of the magnetic field are

$$B_{lm}^{(1)} = \frac{\sqrt{l(l+1)}}{r}\left[-R_\odot\left(\frac{R_\odot}{r}\right)^{l+1} I_0 + I_2(r) + I_3(r),\right] \tag{5.81}$$

and

$$B_{lm}^{(2)} = \frac{1}{r}\left[R_\odot^l\left(\frac{R_\odot}{r}\right)^{l+1} I_0 - lI_1(r) + (l+1)I_2(r)\right]. \tag{5.82}$$

These are equations for the magnetic field presented in Chapter 4.

5.6 Conclusion

In this Chapter we derive a solution to Ampere's law in the domain external to a sphere using a vector-spherical harmonic expansion.

5.7 Appendix A

This appendix contains the definition and basic properties of spherical harmonics.

5.7.1 Spherical Harmonics: Definition

The spherical harmonics $Y_{lm}(\theta,\phi)$ are the eigenfunctions of the angular part of the Laplacian operator in spherical polar coordinates. The standard definition is

$$Y_{lm}(\theta,\phi) = \sqrt{\frac{2l+1}{4\pi}\frac{(l-m)!}{(l+m)!}}P_l^m(\cos\theta)e^{im\phi}, \tag{5.83}$$

where l is a positive integer called the order, and m is an integer called the degree. The function P_l^m is an associated Legendre polynomial which is defined by the equation

$$P_l^m(x) = (-1)^m(1-x^2)^{m/2}\frac{d^m}{dx^m}P_l(x), \tag{5.84}$$

where $P_l(x)$ is a Legendre polynomial.

The magnitude of the associated Legendre polynomials grows rapidly as the order is increased. In practice, calculating $P_l^m(x)$ for $l > 100$ results in numerical overflow. To avoid this problem it is common to define the spherical harmonics in terms of renormalised associated Legendre polynomials $\tilde{P}_l^m(x)$, defined by

$$\tilde{P}_l^m(x) = \sqrt{\frac{2l+1}{4\pi}\frac{(l-m)!}{(l+m)!}}P_l^m(x). \tag{5.85}$$

A stable recursion for $\tilde{P}_l^m(x)$ is given by (Press *et al.*, 2007). In terms of the renormalised associated Legendre polynomials, the spherical harmonics are

$$Y_{lm}(\theta,\phi) = \tilde{P}_l^m(\cos\theta)e^{im\phi}. \tag{5.86}$$

5.7.2 Spherical Harmonics: Basic Properties

The spherical harmonics are orthonormal i.e.

$$\int_0^{2\pi}\int_0^{\pi} Y^*_{l'm'}(\theta,\phi)Y_{lm}(\theta,\phi)\sin\theta d\theta d\phi = \delta_{l'l}\delta_{m'm} \tag{5.87}$$

where $*$ denotes the complex conjugate and δ is the Kronecker delta. The complex conjugate Y^*_{lm} is related to Y_{lm} by the relation

$$Y_{l-m}(\theta,\phi) = (-1)^m Y^*_{lm}(\theta,\phi). \tag{5.88}$$

A function $f(x)$ is said to have even parity with respect to the point a if $f(x-a)$ is an even function. Similarly if $f(x-a)$ is odd then $f(x)$ is said to have odd parity with respect to a. The spherical harmonics inherit the parity of the renormalised associated Legendre polynomials. Specifically,

$$\tilde{P}^m_l[\cos(\pi-\theta)] = (-1)^{l+m}\tilde{P}^m_l(\cos\theta), \tag{5.89}$$

meaning Y_{lm} has either odd or even parity with respect to the equator (i.e. where $\theta = \pi/2$).

5.7.3 Spherical Harmonics: Derivatives

The derivative of Y_{lm} with respect to ϕ has the simple form

$$\frac{\partial Y_{lm}}{\partial\phi} = imY_{lm}. \tag{5.90}$$

The derivative of Y_{lm} with respect to θ is

$$\frac{\partial Y_{lm}}{\partial\theta} = -\sin\theta\frac{d\tilde{P}^m_l}{dx}e^{im\phi}. \tag{5.91}$$

The derivative of $\tilde{P}^m_l$ can be found by differentiating Equation (5.85) and using any of the standard recursion formula for the derivative of P^m_l. Several recursion formula exist, here we consider

$$\frac{d}{dx}P^m_l(x) = \frac{lxP^m_l(x) - (l+m)P^m_{l-1}(x)}{x^2-1} \tag{5.92}$$

(Gradshteyn and Ryzhik, 1980). Using Equations (5.92) and (5.85) it can be shown that

$$\frac{d}{dx}\tilde{P}^m_l(x) = \frac{lx\tilde{P}^m_l(x) - \gamma_{lm}(l+m)\tilde{P}^m_{l-1}(x)}{x^2-1}, \tag{5.93}$$

where

$$\gamma_{lm} = \sqrt{\frac{(2l+1)}{(2l-1)}\frac{(l-m)}{(l+m)}}. \tag{5.94}$$

Therefore

$$\frac{\partial Y_{lm}}{\partial\theta} = \left[\frac{-\gamma_{lm}(l+m)\tilde{P}^m_{l-1}(\cos\theta) + l\cos\theta\tilde{P}^m_l(\cos\theta)}{\sin\theta}\right]e^{im\phi}. \tag{5.95}$$

This can also be written in the form

$$\frac{\partial Y_{lm}}{\partial\theta} = \frac{-\gamma_{lm}(l+m)Y_{l-1m} + l\cos\theta Y_{lm}}{\sin\theta}. \tag{5.96}$$

Equation (5.90) inherits the parity of Y_{lm}. However, determining the parity of Equation (5.96) is more complicated due to its recursive form. By applying the parity rule [i.e. Equation (5.89)] separately to each term in the recursion it can be shown that

$$\frac{\partial}{\partial\theta}Y_{lm}(\pi-\theta,\phi) = (-1)^{l+m+1}\frac{\partial}{\partial\theta}Y_{lm}(\theta,\phi). \tag{5.97}$$

5.8 Appendix B

This appendix contains the definition and basic properties of the vector-spherical harmonics.

5.8.1 Vector-Spherical Harmonics: Definition

There are several different definitions of the vector spherical harmonics (see Morse and Feshbach 1953; Dennis and Quartapelle 1985). Here we follow the conventions of Morse and Feshbach (1953) *i.e.*

$$\mathbf{Y}_{lm}(\theta,\phi) = Y_{lm}(\theta,\phi)\hat{\boldsymbol{r}}, \tag{5.98}$$

$$\boldsymbol{\Psi}_{lm}(\theta,\phi) = \frac{r\nabla Y_{lm}(\theta,\phi)}{\sqrt{l(l+1)}}, \tag{5.99}$$

and

$$\boldsymbol{\Phi}(\theta,\phi) = \frac{\mathbf{r}\times\nabla Y_{lm}(\theta,\phi)}{\sqrt{l(l+1)}}. \tag{5.100}$$

5.8.2 Vector-Spherical Harmonics: Basic Properties

The three vector spherical harmonics are perpendicular to each other i.e.

$$\mathbf{Y}_{lm}\cdot\boldsymbol{\Psi}_{lm} = 0, \tag{5.101}$$

$$\mathbf{Y}_{lm}\cdot\boldsymbol{\Phi}_{lm} = 0, \tag{5.102}$$

and

$$\boldsymbol{\Psi}_{lm}\cdot\boldsymbol{\Phi}_{lm} = 0. \tag{5.103}$$

They also satisfy the orthonormality conditions

$$\int \mathbf{Y}_{lm}(\theta,\phi)\cdot\mathbf{Y}^*_{l'm'}(\theta,\phi)d\Omega = \delta_{lm}\delta_{l'm'}, \tag{5.104}$$

$$\int \boldsymbol{\Psi}_{lm}(\theta,\phi)\cdot\boldsymbol{\Psi}^*_{l'm'}(\theta,\phi)d\Omega = \delta_{lm}\delta_{l'm'}, \tag{5.105}$$

and

$$\int \boldsymbol{\Phi}_{lm}(\theta,\phi)\cdot\boldsymbol{\Phi}^*_{l'm'}(\theta,\phi)d\Omega = \delta_{lm}\delta_{l'm'}, \tag{5.106}$$

where δ_{lm} is the Kronecker delta.

For a function $f(r)$, the divergence of the vector spherical harmonics satisfy the relations

$$\nabla\cdot[f(r)\mathbf{Y}_{lm}] = \left(\frac{d}{dr}+\frac{2}{r}\right)f(r)Y_{lm}, \tag{5.107}$$

$$\nabla\cdot[f(r)\boldsymbol{\Psi}_{lm}] = -\sqrt{l(l+1)}\frac{f(r)}{r}Y_{lm}, \tag{5.108}$$

and

$$\nabla\cdot[f(r)\boldsymbol{\Phi}_{lm}] = 0. \tag{5.109}$$

Furthermore, if a vector field $\mathbf{V}$ is described by a vector-spherical harmonics series

$$\mathbf{V} = \sum_{l=0}^{\infty}\sum_{m=-l}^{l} V^{(1)}_{lm}\mathbf{Y}_{lm} + V^{(2)}_{lm}\boldsymbol{\Psi}_{lm} + V^{(3)}_{lm}\boldsymbol{\Phi}_{lm}, \tag{5.110}$$

then $\nabla \cdot \mathbf{V}$ is

$$\nabla \cdot \mathbf{V} = \frac{dV_{lm}^{(1)}}{dr} + \frac{2V_{lm}^{(1)}}{r} - \sqrt{l(l+1)}\frac{V_{lm}^{(2)}}{r}. \tag{5.111}$$

For a function $f(r)$, the curl of the vector spherical harmonics satisfy the relations

$$\nabla \times [f(r)\mathbf{Y}_{lm}] = \sqrt{l(l+1)}\frac{f(r)}{r}\mathbf{\Phi}_{lm}, \tag{5.112}$$

$$\nabla \times [f(r)\mathbf{\Psi}_{lm}] = -\left(\frac{d}{dr} + \frac{1}{r}\right) f(r)\mathbf{\Phi}_{lm}, \tag{5.113}$$

and

$$\nabla \times [f(r)\mathbf{\Phi}_{lm}] = \sqrt{l(l+1)}\frac{f(r)}{r}\mathbf{Y}_{lm} + \left(\frac{d}{dr} + \frac{1}{r}\right) f(r)\mathbf{\Psi}_{lm}. \tag{5.114}$$

For the vector field $\mathbf{V}_{lm}$ described by Equation (5.110) it follows that

$$\nabla \times \mathbf{V} = \sqrt{l(l+1)}\frac{V_{lm}^{(3)}}{r}\mathbf{Y}_{lm} + \left(\frac{d}{dr} + \frac{1}{r}\right) V_{lm}^{(3)}\mathbf{\Psi}_{lm} \tag{5.115}$$

$$+ \sqrt{l(l+1)}\frac{V_{lm}^{(1)}}{r}\mathbf{\Phi}_{lm} - \left(\frac{d}{dr} + \frac{1}{r}\right) V_{lm}^{(2)}\mathbf{\Phi}_{lm}. \tag{5.116}$$

5.8.3 Vector-Spherical Harmonics: Component Form

The components of the vector spherical harmonics in spherical polar coordinates are:

$$\mathbf{Y}_{lm}(\theta,\phi) = Y_{lm}\hat{\boldsymbol{r}} \tag{5.117}$$

$$\mathbf{\Psi}_{lm}(\theta,\phi) = [l(l+1)]^{-1/2}\left[\frac{\partial Y_{lm}}{\partial\theta}\hat{\boldsymbol{\theta}} + \frac{im}{\sin\theta}Y_{lm}\hat{\boldsymbol{\phi}}\right], \tag{5.118}$$

and

$$\mathbf{\Phi}_{lm}(\theta,\phi) = [l(l+1)]^{-1/2}\left[-\frac{\partial Y_{lm}}{\partial\theta}\hat{\boldsymbol{\phi}} + \frac{im}{\sin\theta}Y_{lm}\hat{\boldsymbol{\theta}}\right]. \tag{5.119}$$

5.8.4 Vector-Spherical Harmonics: Table

This section contains a table of the first few vector spherical harmonics.

$$\mathbf{Y}_{10}(\theta,\phi) = \sqrt{\frac{3}{4\pi}}\cos\theta\hat{\boldsymbol{r}} \tag{5.120}$$

$$\mathbf{\Psi}_{10}(\theta,\phi) = -\sqrt{\frac{3}{8\pi}}\sin\theta\hat{\boldsymbol{\theta}} \tag{5.121}$$

$$\mathbf{\Phi}_{10}(\theta,\phi) = \sqrt{\frac{3}{8\pi}}\sin\theta\hat{\boldsymbol{\phi}} \tag{5.122}$$

$$\mathbf{Y}_{11}(\theta,\phi) = -\sqrt{\frac{3}{8\pi}}\sin\theta\hat{\boldsymbol{r}} \tag{5.123}$$

$$\mathbf{\Psi}_{11}(\theta,\phi) = -\sqrt{\frac{3}{16\pi}}\left[\cos\theta\,\hat{\boldsymbol{\theta}} + i\hat{\boldsymbol{\phi}}\right]e^{i\phi} \tag{5.124}$$

$$\mathbf{\Phi}_{11}(\theta,\phi) = \sqrt{\frac{3}{16\pi}}\left[\cos\theta\hat{\boldsymbol{\phi}} - i\hat{\boldsymbol{\theta}}\right]e^{i\phi} \tag{5.125}$$

Chapter 6

Conclusion and Scope for Future Work

The goal of coronal magnetic field extrapolations is to reliably determine the coronal magnetic field in the corona from observations of the magnetic field at the photosphere. The work in this thesis is a step towards this goal. Present methods based on a nonlinear force-free model of the coronal magnetic field have numerous shortcomings. These are outlined in Chapter 1 and demonstrated in Chapter 2. In this thesis we present two numerical codes which, in principle, address two of the problems with the present modelling.

In Chapter 3 we present an implementation of the Grad-Rubin method (Grad and Rubin, 1958) for solving a magneto-hydrostatic model of the coronal magnetic field. The magneto-hydrostatic model addresses the inconsistency that exists between the force-free model and the forced spectro-polarimetric boundary data. The code was applied to an analytic test case to demonstrate the accuracy and speed of the code. We did not apply the code to spectro-polarimetric data and this is a possibility for future work. The work in Chapter 3 considers only pressure forces. Additional forces such as gravity could be included in future work.

In Chapter 4 we present a code for solving the nonlinear force-free equations in spherical polar geometry. The motivation for this work is to model regions of the corona which are too large to be modelled reliably with existing methods based on Cartesian geometry. We demonstrate the correctness of the code by application to a test case. The code is an implementation of the Grad-Rubin method, and is based on a global spectral representation of the magnetic field in terms of vector-spherical harmonic functions. In Chapter 5 we derive the spectral solutions presented in Chapter 4.

There are a number of ways the work in Chapter 4 could be extended. Firstly, the existing code has not been completely optimised. There are improvements that can be made in terms of memory management and parallelisation. Secondly, the model can be extended to include the effect of the solar wind by implementing source-surface boundary conditions. Finally, the code can be applied to spectro-polarimetric data. A comparison between spherical modelling and Cartesian modelling would help quantify the improvement of the spherical modelling over the Cartesian modelling.

In this thesis we have emphasised the application of the codes to spectro-polarimetric data. However, the codes can also be used with analytic boundary conditions to address theoretical questions, such as the uniqueness and existence of solutions, and the Aly-Sturrock conjecture (Aly, 1991; Sturrock, 1991). These questions are difficult to address analytically due to the nonlinear character of the force-free and magneto-hydrostatic equations, but in principle can be addressed numerically using the methods developed in this thesis.

The correctness of the theory and numerical codes presented in this thesis has been demonstrated using simple test cases. The work in this thesis addresses problems with the existing model and lays the foundations for the next generation of extrapolation models for the coronal magnetic field.

Bibliography

Akabane, K.: 1956, *Publ. Astron. Soc. Japan* **8**, 173.

Alissandrakis, C.E.: 1981, *Astron. Astrophys.* **100**, 197.

Altschuler, M.D., Newkirk, G.: 1969, *Solar Phys.* **9**, 131.

Aly, J.J.: 1991, *Astrophys. J. Lett.* **375**, L61.

Amari, T., Aly, J.J., Canou, A., Mikic, Z.: 2013, *Astron. Astrophys.* **553**, A43.

Amari, T., Boulbe, C., Boulmezaoud, T.Z.: 2009, *SIAM J. Sci. Comput.* **31**, 3217.

Amari, T., Boulmezaoud, T.Z., Aly, J.J.: 2006, *Astron. Astrophys.* **446**, 691.

Amari, T., Boulmezaoud, T.Z., Mikic, Z.: 1999, *Astron. Astrophys.* **350**, 1051.

Aschwanden, M.J.: 2004, *Physics of the Solar Corona*, Springer, Berlin, 196.

Aschwanden, M.J., Schrijver, C.J.: 2011, *Astrophys. J.* **736**, 102.

Auer, L.H., House, L.L., Heasley, J.N.: 1977, *Solar Phys.* **55**, 47.

Babcock, H.W.: 1953, *Astrophys. J.* **118**, 387.

Barbosa, D.D.: 1978, *Solar Phys.* **56**, 55.

Barrera, R.G., Estévez, G.A., Giraldo, J.: 1985, *Eur. J. Phys.* **6**, 287.

Beckers, J.M.: 1968, *Solar Phys.* **5**, 15.

Bineau, M.: 1972, *Commun. Pure Appl. Math.* **25**, 77.

Bisnovatyi-Kogan, G.S., Blinnikov, S.I.: 1976, *Soviet Astronomy Letters* **2**, 191.

Boulmezaoud, T.Z., Amari, T.: 2000, *Z. Angew. Math. Phys.* **51**, 942.

Boyd, J.P.: 2001, *Chebyshev and Fourier Spectral Methods*, 2nd edn. Dover Publications Inc, New York, 380.

Chandra, R., Menon, R., Dagum, L., Kohr, D., Maydan, D., McDonald, J.: 2001, *Parallel Programming in OpenMP*, Morgan Kaufmann Publishers, San Francisco, 1.

Chiu, Y.T., Hilton, H.H.: 1977, *Astrophys. J.* **212**, 873.

Chodura, R., Schlueter, A.: 1981, *Journal of Computational Physics* **41**, 68.

Cuperman, S., Ofman, L., Semel, M.: 1990, *Astron. Astrophys.* **227**, 583.

De Rosa, M.L., Schrijver, C.J., Barnes, G., Leka, K.D., Lites, B.W., *et al.*: 2009, *Astrophys. J.* **696**, 1780.

Demoulin, P., Cuperman, S., Semel, M.: 1992, *Astron. Astrophys.* **263**, 351.

Dennis, S.R., Quartapelle, L.: 1985, *J. Comp. Phys.* **61**, 218.

Dulk, G.A., McLean, D. J.: 1978, *Solar Phys.* **57**, 279.

Emslie, A.G., Kucharek, H., Dennis, B.R., Gopalswamy, N., Holman, G.D., *et al.*: 2004, *J. Geophys. Res.* **109**, 10104.

Fuhrmann, M., Seehafer, N., Valori, G.: 2007, *Astron. Astrophys.* **476**, 349.

Gary, G.A.: 2001, *Solar Phys.* **203**, 71.

Gary, G.A., Hagyard, M.J.: 1990, *Solar Phys.* **126**, 21.

Gary, D.E., Fleishman, G.D., Nita, G.M.: 2013, *Solar Phys.* **288**, 549.

Gelfreikh, G.B.: 1994, In: Vojtech Rusin, Petr Heinzel, Jean-Claude Vial (eds.) *Solar Coronal Structures. Proceedings of the 144th IAU Colloquium*, 21.

Georgoulis, M.K.: 2005, *Astrophys. J. Lett.* **629**, L69.

Gilchrist, S.A., Wheatland, M.S.: 2014, *Solar Phys.* **289**, 1153.

Gopalswamy, N., Yashiro, S., Michalek, G., Stenborg, G., Vourlidas, A., *et al.*: 2009, *Earth, Moon, Planets* **104**, 295.

Grad, H., Rubin, H.: 1958, *Proc. 2nd Int. Conf. Peaceful Uses of Atomic Energy* **31**, 190.

Gradshteyn, I.S., Ryzhik, I.M.: 1980, *Table of integrals, series and products*, 5th edn. Academic Press, New York, 1005.

Hale, G.E.: 1908, *Astrophys. J.* **28**, 315.

Harvey, J., Livingston, W., Slaughter, C.: 1972, *Line Formation in the Presence of Magnetic Fields*, 227.

Henney, C.J., Keller, C.U., Harvey, J.W.: 2006, In: Casini, R., Lites, B.W. (eds.) *Solar Polarization 4, ASP Conf. Ser.* **358**, 92.

Holman, G.D.: 2005, *Adv. Space Res.* **35**, 1669.

Hudson, H.S.: 1991, *Solar Phys.* **133**, 357.

Hudson, H.S.: 2007, *Astrophys. J. Lett.* **663**, L45.

Jackson, J.D.: 1998, *Classical Electrodynamics,* 3rd edn. Wiley, New York, 180.

Jaynes, E.T., Bretthorst, G.L.: 2003, *Probability Theory*, Cambridge University Press, Cambridge, 86.

Jefferies, J., Lites, B.W., Skumanich, A.: 1989, *Astrophys. J.* **343**, 920.

Jefferies, J.T., Mickey, D.L.: 1991, *Astrophys. J.* **372**, 694.

Judge, P.G.: 1998, *Astrophys. J.* **500**, 1009.

Judge, P.G., Habbal, S., Landi, E.: 2013, *Solar Phys.* **288**, 467.

Kaiser, R., Neudert, M., von Wahl, W.: 2000, *Commun. Math. Phys.* **211**, 111.

Kiepenheuer, K.O.: 1953, *Astrophys. J.* **117**, 447.

Kosugi, T., Matsuzaki, K., Sakao, T., Shimizu, T., Sone, Y., *et al.*: 2007, *Solar Phys.* **243**, 3.

Landi Degl'Innocenti, E.: 1979, *Solar Phys.* **63**, 237.

Landi Degl'Innocenti, E., Landolfi, M.: 2004, *Polarization in Spectral Lines*, Kluwer Academic Publishers, Dordrecht, 625.

Leka, K.D., Barnes, G., Crouch, A.: 2009, In: Lites, B., Cheung, M., Magara, T., Mariska, J., Reeves, K. (eds.), *The Second Hinode Science Meeting: Beyond Discovery – Toward Understanding, ASP Conf. Ser.* **415**, 365.

Leka, K.D., Barnes, G., Crouch, A.D., Metcalf, T.R., Gary, G.A. *et al.*: 2009, *Solar Phys.* **260**, 83.

Leighton, R.B.: 1959, *Astrophys. J.* **130**, 366.

Leroy, J.L.: 1977, *Astron. Astrophys.* **60**, 79.

Lin, R.P., Dennis, B.R., Hurford, G.J., Smith, D.M., Zehnder, A., *et al.*: 2002, *Solar Phys.* **210**, 3.

Lin, R.P., Hudson, H.S.: 1971, *Solar Phys.* **17**, 412.

Lin, H., Kuhn, J.R., Coulter, R.: 2004, *Astrophys. J. Lett.* **613**, L177.

Lin, H., Penn, M.J., Tomczyk, S.: 2000, *Astrophys. J. Lett.* **541**, L83.

Lites, B.W., Elmore, D.F., Seagraves, P., Skumanich, A.P.: 1993, *Astrophys. J.* **418**, 928.

Lites, B.W., Skumanich, A.: 1990, *Astrophys. J.* **348**, 747.

Livingston, W., Penn, M.: 2009, *EOS Trans.* **90**, 257.

Low, B.C., Lou, Y.Q.: 1990, *Astrophys. J.* **352**, 343.

Maltagliati, L., Falchi, A., Teriaca, L.: 2006, *Solar Phys.* **235**, 125.

Melrose, D.B., McPhedran, R.C.: 1991, *Electromagnetic Processes in Dispersive Media*, Cambridge University Press, Cambridge, 319.

Metcalf, T.R.: 1994, *Solar Phys.* **155**, 235.

Metcalf, T.R., Jiao, L., McClymont, A.N., Canfield, R.C., Uitenbroek, H.: 1995, *Astrophys. J.* **439**, 474.

Metcalf, T.R., Leka, K.D., Barnes, G., Lites, B.W., Georgoulis, M.K., *et al.*: 2006, *Solar Phys.* **237**, 267.

Mikić, Z., Linker, J.A., Schnack, D.D., Lionello, R., Tarditi, A.: 1999, *Physics of Plasmas* **6**, 2217.

Molodenskii, M.M.: 1969, *Soviet Astronomy* **12**, 585.

Molodensky, M.M.: 1974, *Solar Phys.* **39**, 393.

Morse, P.M., Feshbach, H.: 1953, *Methods of Theoretical Physics, part two*, McGraw-Hill, New York, 1252.

Nagai, F.: 1980, *Solar Phys.* **68**, 351.

Nakagawa, Y., Raadu, M. A.: 1972, *Solar Phys.* **25**, 127.

Pesnell, W.D., Thompson, B.J., Chamberlin, P.C.: 2012, *Solar Phys.* **275**, 3.

Pevtsov, A.A., Canfield, R.C., Metcalf, T.R.: 1994, *Astrophys. J. Lett.* **425**, L117.

Poularikas, A.D.: 1996, *The Transform and Applications Handbook*, CRC Press, Florida, 227.

Press, W.H., Teukolsky, S.A., Vetterling, W.T., Flannery, B.P.: 2007, *Numerical Recipes. The Art of Scientific Computing*, 3rd edn. Cambridge University Press, Cambridge, 292.

Priest, E.R.: 1984, *Solar Magnetohydrodynamics*, D.Reidel Publishing Company, Dordrecht, 117.

Priest, E.R., Forbes, T.G.: 2002, *Astron. Astrophys. Rev.* **10**, 313.

Rachkovsky, D.N.: 1962, *Izv. Krymsk. Astrofiz. Observ.* **28**, 259.

Régnier, S.: 2013, *Solar Phys.* **288**, 481

Régnier, S., Priest, E.R.: 2007, *Astrophys. J. Lett.* **669**, L53.

Reiman, A., Greenside, H.: 1986, *Comp. Phys. Com.* **43**, 157.

Rudenko, G.V.: 2001, *Solar Phys.* **198**, 279.

Rust, D.M.: 1967, *Astrophys. J.* **150**, 313.

Sakurai, T.: 1981, *Solar Phys.* **69**, 343.

Sakurai, T.: 1982, *Solar Phys.* **76**, 301.

Sakurai, T.: 1989, *Space Sci. Rev.* **51**, 11.

Saint-Hilaire, P., Benz, A.O.: 2002, *Solar Phys.* **210**, 287.

Saint-Hilaire, P., Benz, A.O.: 2005, *Astron. Astrophys.* **435**, 743.

Schatten, K.H., Wilcox, J.M., Ness, N.F.: 1969, *Solar Phys.* **6**, 442.

Scherrer, P.H., Bogart, R.S., Bush, R.I., Hoeksema, J.T., Kosovichev, A.G., *et al.*: 1995, *Solar Phys.* **162**, 129.

Schmidt, H.U.: 1964, *NASA Special Publication* **50**, 107.

Schou, J., Scherrer, P.H., Bush, R.I., Wachter, R., Couvidat, S., *et al.*: 2012, *Solar Phys.* **275**, 229.

Schrijver, C.J., De Rosa, M.L., Metcalf, T.R., Barnes, G., Lites, B., *et al.*: 2008, *Astrophys. J.* **675**, 1637.

Schrijver, C.J., De Rosa, M.L., Metcalf, T.R., Liu, Y., McTiernan, J., *et al.*: 2006, *Solar Phys.* **235**, 161.

Schrijver, C.J., De Rosa, M.L., Title, A.M., Metcalf, T.R.: 2005, *Astrophys. J.* **628**, 501.

Semel, M.: 1988, *Astron. Astrophys.* **198**, 293.

Skumanich, A., Lites, B.W.: 1987, *Astrophys. J.* **322**, 473.

Snir, M., Otto, S., Huss-Lederman, S., Walker, D., Dongarra., J: 1998, *MPI–the complete reference*, 2nd edn. MIT Press, Massachusetts, 1.

Stepanov, V.E., Severny, A.B.: 1962, *Izv. Krymsk. Astrofiz. Observ.* **28**, 166.

Stenflo, J.O.: 1978, *Reports on Progress in Physics* **41**, 865.

Stenflo, J.O.: 1994, *Solar Magnetic Fields, Polarization Radiation Diagnostics*, Kluwer Academic Publishers, Dordrecht, 1.

Stenflo, J.O.: 2013, *Astron. Astrophys. Rev.* **21**, 66.

Sturrock, P.A.: 1991, *Astrophys. J.* **380**, 655.

Sturrock, P.A.: 1994, *Plasma Physics, An Introduction to the Theory of Astrophysical, Geophysical and Laboratory Plasmas*, Cambridge University Press, Cambridge, 201.

Sun, X., Liu, Y., Hoeksema, J.T., Hayashi, K., Zhao, X.: 2011, *Solar Phys.* **270**, 9.

Thalmann, J.K., Wiegelmann, T., Raouafi, N.E.: 2008, *Astron. Astrophys.* **488**, L71.

Tóth, G., van der Holst, B., Huang, Z.: 2011, *Astrophys. J.* **732**, 102.

Tsuneta, S., Ichimoto, K., Katsukawa, Y., Nagata, S., Otsubo, M., *et al.*: 2008, *Solar Phys.* **249**, 167.

Tun, S.D., Gary, D.E., Georgoulis, M.K.: 2011, *Astrophys. J.* **728**, 1.

Unno, W.: 1956, *Publ. Astron. Soc. Japan* **8**, 108.

Usmanov, A.V.: 1996, *AIP Conf. Proc.* **382**, 141.

Valori, G., Kliem, B., Keppens, R.: 2005, *Astron. Astrophys.* **433**, 335.

Venkatakrishnan, P., Hagyard, M.J., Hathaway, D.H.: 1988, *Solar Phys.* **115**, 125.

Wang, Y.M., Sheeley, N.R.: 1992, *Astrophys. J.* **392**, 310.

Wheatland, M.S.: 1999, *Astrophys. J.* **518**, 948.

Wheatland, M.S.: 2000, *Astrophys. J.* **532**, 1209.

Wheatland, M.S.: 2006, *Solar Phys.* **238**, 29.

Wheatland, M.S.: 2007, *Solar Phys.* **245**, 251.

Wheatland, M.S.: 2010, *Astrophys. J.* **710**, 1324.

Wheatland, M.S., Leka, K.D.: 2011, *Astrophys. J.* **728**, 112.

Wheatland, M.S., Régnier, S.: 2009, *Astrophys. J. Lett.* **700**, L88.

Wheatland, M.S., Sturrock, P.A., Roumeliotis, G.: 2000, *Astrophys. J.* **540**, 1150.

White, S.M., Kundu, M.R.: 1997, *Solar Phys.* **174**, 31.

Wiegelmann, T.: 1998, *Physica Scripta Volume T* **74**, 77.

Wiegelmann, T.: 2004, *Solar Phys.* **219**, 87.

Wiegelmann, T.: 2007, *Solar Phys.* **240**, 227.

Wiegelmann, T.: 2008, *J. Geophys. Res.* **113**, 3.

Wiegelmann, T., Inhester, B.: 2003, *Solar Phys.* **214**, 287.

Wiegelmann, T., Inhester, B.: 2010, *Astron. Astrophys.* **516**, A107.

Wiegelmann, T., Inhester, B., Sakurai, T.: 2006, *Solar Phys.* **233**, 215.

Wiegelmann, T., Lagg, A., Solanki, S.K., Inhester, B., Woch, J.: 2005, *Astron. Astrophys.* **433**, 701.

Wiegelmann, T., Neukirch, T.: 2006, *Astron. Astrophys.* **457**, 1053.

Wiegelmann, T., Neukirch, T., Ruan, P., Inhester, B.: 2007, *Astron. Astrophys.* **475**, 701.

Wiegelmann, T., Sakurai, T.: 2012, *Living Rev. Solar Phys.* **9**, 5. http://www.livingreviews.org/lrsp-2012-5

Wu, S.T., Sun, M.T., Chang, H.M., Hagyard, M.J., Gary, G.A.: 1990, *Astrophys. J.* **362**, 698.

Yan, Y., Sakurai, T.: 2000, *Solar Phys.* **195**, 89.

Yang, W.H., Sturrock, P.A., Antiochos, S.K.: 1986, *Astrophys. J.* **309**, 383.

Zikanov, O.: 2010, *Essential Computational Fluid Dynamics*, Wiley, New Jersey, 66.

Zwillinger, D.: 1989, *Handbook of Differential Equations*, 2nd edn. Academic Press, San Diego, 356.